SEASAT Report

MITRE

SEASAT Report

K. Case
R. Dashen
W. Munk
J. Vesecky
K. Watson
F. Zachariasen

January 1985

JSR-83-203

JASON
The MITRE Corporation
1820 Dolley Madison Boulevard
McLean, Virginia 22102

Unclassified

SECURITY CLASSIFICATION OF THIS PAGE (When Data Entered)

REPORT DOCUMENTATION PAGE

READ INSTRUCTIONS BEFORE COMPLETING FORM

1. REPORT NUMBER: JSR-83-203

2. GOVT ACCESSION NO.

3. RECIPIENT'S CATALOG NUMBER

4. TITLE (and Subtitle): Seasat Report

5. TYPE OF REPORT & PERIOD COVERED

6. PERFORMING ORG. REPORT NUMBER

7. AUTHOR(s): K. Case, R. Dashen, W. Munk, J. Vesecky, K. Watson, F. Zachariasen

8. CONTRACT OR GRANT NUMBER(s): F19628-84-C-0001

9. PERFORMING ORGANIZATION NAME AND ADDRESS:
The MITRE Corporation
1820 Dolley Madison Boulevard
McLean, Virginia 22102

10. PROGRAM ELEMENT, PROJECT, TASK AREA & WORK UNIT NUMBERS

11. CONTROLLING OFFICE NAME AND ADDRESS

12. REPORT DATE: March 1984

13. NO. OF PAGES: 211

14. MONITORING AGENCY NAME & ADDRESS (if diff. from Controlling Office)

15. SECURITY CLASS. (of this report): Unclassified

15a. DECLASSIFICATION/DOWNGRADING SCHEDULE

16. DISTRIBUTION STATEMENT (of this report)

17. DISTRIBUTION STATEMENT (of the abstract entered in Block 20, if different from report)

18. SUPPLEMENTARY NOTES

19. KEY WORDS (Continue on reverse side if necessary and identify by block number)

P 1-1

20. ABSTRACT (Continue on reverse side if necessary and identify by block number)

A brief overview of SEASAT and ship wake characteristics is given. The authors do not believe that the V-shaped wakes seen by the SEASAT satellite are external waves because ship wakes are three to four orders of magnitude too weak to explain the observed radar returns.

If the V-shaped wakes are not produced by internal waves, then by default they must be manifestations of the Kelvin wake. Present understanding of rear axis

(Continued)

DD FORM 1 JAN 73 1473

EDITION OF 1 NOV 65 IS OBSOLETE

Unclassified

SECURITY CLASSIFICATION OF THIS PAGE (When Data Entered)

19 KEY WORDS (Continued)

20 ABSTRACT (Continued)

generation of Kelvin wakes ("thin ship theory") does not adequately explain the effects seen by SEASAT. Non-linear effects probably need to be included. Also ship's propellor-generated Kelvin wakes do not appear to be strong enough to create the wakes seen.

Consequently, we are left with a somewhat unsatisfying situation. We believe that narrow wakes cannot be produced by ship generated internal waves, (except under extreme conditions) because these are too weak by three or four orders of magnitude. Therefore, they must be due to the Kelvin wake. But we have not yet been able to analyze the Kelvin wake sufficiently well theoretically to identify just which feature of the Kelvin wake SEASAT is seeing.

ACKNOWLEDGEMENTS

Professor G. L. Tyler of Stanford Univeristy is gratefully acknowledged for his help in investigating radar scattering effects associated with wakes.

TABLE OF CONTENTS

TABLE OF CONTENTS
(CONT'D)

TABLE OF CONTENTS
(CONT'D)

LIST OF ILLUSTRATIONS

LIST OF ILLUSTRATIONS
(CONT'D.)

LIST OF TABLES

1.0 INTRODUCTION AND SUMMARY

This report is concerned with the narrow V-shaped wakes seen behind surface ships by the SEASAT synthetic aperture radar. An example is shown in Figure 1-1.

The following characteristics appear to be typical. The wake (full) angles vary greatly, ranging from as little as 3° to (rarely) the full 39° of the Kelvin wake caustics. There seems to be a correlation between wake angle and ship size or speed: smaller (slower?) ships have larger wake angles than larger (faster?) ships. The overall wake lengths can be large, up to 10 or 15 km in some cases. There is apparently no correlation between the wake angle and the aspect angle of the ship's track--that is, the angle between the ship's track and the satellite track. The complete wake consists of an outer V which appears white, reflecting an increased radar cross section, together with an axial dark strip, reflecting a decrease in radar cross section. Often, however, only part of this structure is visible; one may see only one side of the white V, together with or without the dark centerline, or sometimes just the dark centerline itself. No statistics seem to exist on how often no wake at all is visible. No correlation has been made between specific SEASAT images and specific ships, so the size and speed of

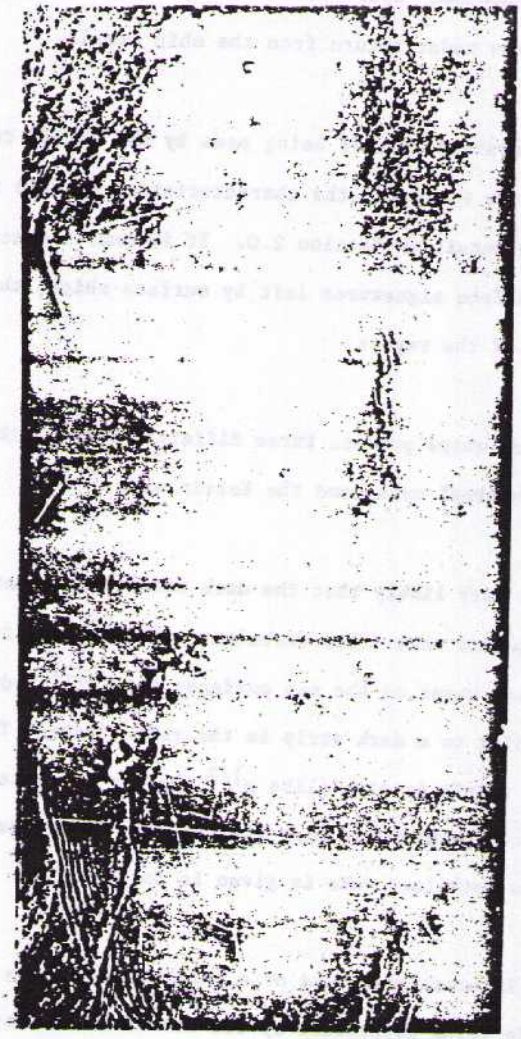

Figure 1-1. Narrow V-shaped wakes seen behind surface ships by the SEASAT synthetic aperture radar.

the ships is unknown--apart from the qualitative implications of the strength of the radar return from the ship itself.

To understand what is being seen by the SEASAT radar, it is first necessary to recall the characteristics of this radar. These are given in detail in Section 2.0. It is next necessary to understand the surface signatures left by surface ships; this occupies the balance of the report.

Surface ships produce three different wakes: the turbulent wake, the internal wake, and the Kelvin wake.

It is very likely that the dark centerline observed by SEASAT is the turbulent wake. The turbulent wake is known to smooth out small ambient waves on the sea surface; this will reduce the radar return leading to a dark strip in the radar image. The turbulent wake grows slowly in size (like $x^{1/2}$ where x is distance behind the ship) and can persist for many kilometers. A more detailed discussion of the turbulent wake is given in Section 5.0.

The internal wave wake of a ship should form a narrow V, the outer angle being determined by the relative velocity of the ship and the fastest internal wave, the speed of which is determined by

the local thermocline. For typical parameters one would expect a full wake angle of a few degrees. Qualitatively, slower ships should have larger wake angles. In principle, there should be several successive crests. More details appear in Section 3.1.

Natural internal waves can be easily seen on SEASAT images. Nevertheless, we do not believe the V-shaped ship wakes can be internal waves, because ship generated internal waves are too weak by approximately three or four orders of magnitude to explain the observed radar returns. The mechanism by which internal waves generate a radar signal is as follows. Internal waves produce a horizontal current on the ocean surface; they do not displace the surface vertically (except by an exceedingly small amount). The surface current strains the ambient surface waves and changes their mean slope; this changes the radar cross section. If there are no ambient waves, there is no radar return and no way to see an internal wave. Thus the change in radar cross section produced by an internal wave is proportional to the ambient cross section already present: $\Delta\sigma = \epsilon\sigma$. The proportionality constant ϵ is (essentially) the surface strain.

The ambient cross section is largely Bragg scattering from a rough surface at, for SEASAT, a Bragg wavelength of 30 cm. Since

the surface is rough, the phase change between scatterers is large. The variance in the cross section is therefore equal to the mean: $\langle(\sigma - \langle\sigma\rangle)^2\rangle = \langle\sigma\rangle^2$. Hence to extract a change in cross section of $\varepsilon\sigma$ from background noise requires $1/\varepsilon^2$ independent samples, for a signal-to noise of one.

For SEASAT, the number of independent samples is the number of pixels in the wake, not more than 10^4. The values of ε can be .1 to .3 for natural internal waves, but only 10^{-4} or so (depending on ship size and speed and on the local thermocline) for a ship. Hence, the natural internal waves can be seen, but not ship generated ones, except in conditions of exceptionally strong thermoclines with correspondingly large values of ε . Such situations do occasionally arise. We have seen one SEASAT image taken in the Strait of Georgia showing a ship wake with several parallel crests; this is likely to be an internal wave wake. However, the Strait of Georgia is well known as a region of huge thermoclines; internal wave wakes can even be seen visually there.

The argument briefly summarized here is given in detail in Section 3.2.

If the V-shaped wakes are not produced by internal waves, then by default they must be manifestations of the Kelvin wake.

The kinematics of the Kelvin wake are well known (and described in detail in Section 4.1); the dominant features are two sets of waves, divergent and transverse, meeting at a caustic at a (full) wake angle of 39° independent of ship speed or size. Obviously, however, this caustic is <u>not</u> what is (generally) seen by SEASAT.

The Kelvin wake, of course, changes the ocean surface vertically, so the radar is responding to a quite different effect than it is for internal waves. When the slope of the ocean surface is changed by the Kelvin wake, the Bragg waves that are responsible for the major part of the radar cross section are tilted; this produces a shift in the apparent aspect angle of the radar and therefore changes the effective Bragg wavelength. Because of the k^{-4} spectrum of ambient surface waves, the tilting therefore changes the radar cross section. Evidently, then, the most important part of the Kelvin wake to the radar is the region of maximum slope. We begin our Kelvin wake discussion with a more detailed description of this effect (Section 4.2).

The dynamics of the Kelvin wake are not well known, and in particular, it is difficult to calculate quantitatively the amplitudes and slopes of waves in the wake as a function of ship characteristics; this is especially true in the near axis region of the wake in which, it turns out, is what we are most interested.

The standard treatment is known as "thin ship theory;" this is described in Section 4.1 as a baseline calculation. "Thin ship theory" is only an approximation to the full linearized surface wave problem, which seems to be known in the trade as the "Kelvin-Neumann problem." This is addressed in Section 4.3. Our conclusions, however, are that this treatment is probably also not adequate to describe the near axis wake. At small wake angles, it is quite likely that non-linear effects will be important. One of these which may be particularly significant is the convection by the potential flow around the hull of short surface waves produced near the bow.

Other sources of Kelvin wakes besides the hull itself may also be important. In Section 4.5 we discuss the Kelvin wake produced by the ship's propeller. It turns out that, kinematically, the caustics in propeller wake are at quite small angles, a few degrees instead of the 39° of the conventional Kelvin wake. Also, there is

a strong speed dependence of the caustic angle--slower ships have bigger angles. However, it seems unlikely that the propeller source strength is adequate to explain the SEASAT images.

In conclusion, we are left with a somewhat unsatisfying situation. We believe that narrow wakes cannot be produced by ship generated internal waves, (except under extreme conditions) because these are too weak by three or four orders of magnitude. Therefore, they must be due to the Kelvin wake. But we have not yet been able to analyze the Kelvin wake sufficiently well theoretically to identify just which feature of the Kelvin wake SEASAT is seeing.

It may well be, then, that the situation will only be cleared up by an experiment. Some thoughts as to what this should include appear in Section 6.0.

2.0 RADAR ASPECTS

2.1 Radar Aspects of SEASAT-SAR Wake Images

2.1.1 Introduction

The SEASAT satellite shown in Figure 2-1 operated from July 4 to October 10, 1978, gathering (along with other data) synthetic aperture radar (SAR) images equivalent to about 20% of the Earth's surface, i.e., an area of some 10^8 km^2. The image resolution varied from about 6 m to 40 m, depending upon direction and processing as discussed below. Since such a radar can operate night and day and through clouds, it is clearly a formidable tool for surveillance and remote sensing of environmental conditions over the ocean. Table 2-1 summarizes some basic characteristics of the SEASAT SAR system. These parameters are to some extent optimized to observe ocean surface phenomena. In Figure 2-2 we illustrate the SEASAT SAR observational geometry.

As with many remote sensing techniques, SEASAT SAR images enable large scale features to be observed. Ship wakes are salient features in SEASAT SAR images in part because they are often observed to have lengths of over 10 to 20 km. Further, the

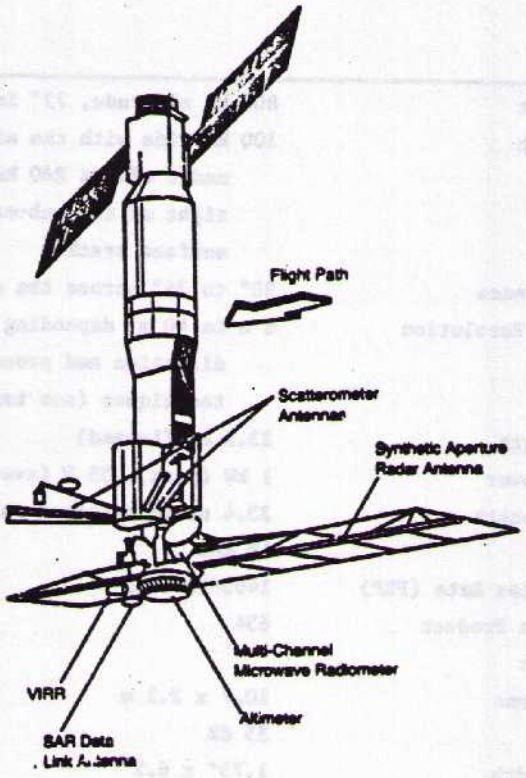

Figure 2-1. The SEASAT satellite showing the 2.2 x 10.7 m synthetic aperture radar antenna. The long axis of the satellite points toward the satellite's nadir and the SAR antenna observes downward and to the right of the satellite velocity vector.

TABLE 2-1

CHARACTERISTICS OF THE SEASAT SAR SYSTEM

Satellite Orbit	800 km altitude, 72° inclination
SAR Image Swath	100 km wide with the side nearest nadir offset 240 km to the right of the sub-satellite surface track
Angle of Incidence	20° to 26° across the swath
Typical Image Resolution	6 m to 40 m, depending on direction and processing techniques (see text)
Radar Wavelength	23.5 cm (L-band)
Transmitter Power	1 kW (peak), 55 W (average)
Chirp Pulse Length	33.4 μs (compressed pulse ~ 65ns)
RF Bandwidth	19 MHz
Pulse Repetition Rate (PRF)	1463-1640 Hz
Time-Bandwidth Product	634
Radar Antenna:	
Dimensions	10.7 x 2.2 m
Gain	35 dB
Beam Width	1.73° x 6.2°
Polarization	99% horizontal (perpendicular to plane of incidence)
Ground-Based Data Recorder Rate	110 M bits/second (5 bits/word)

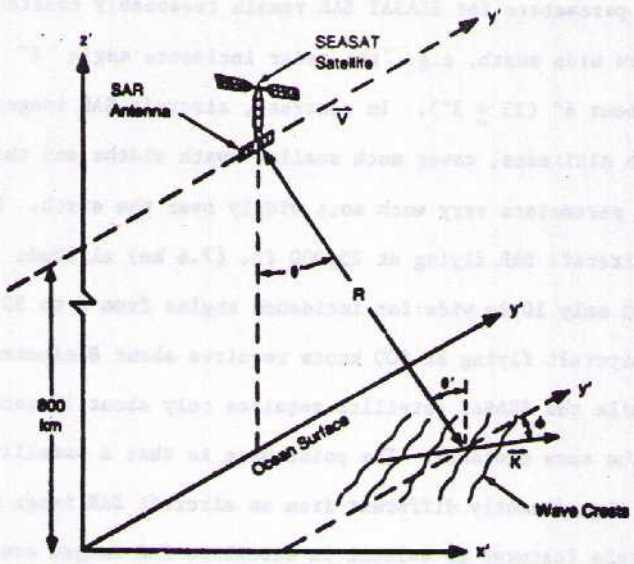

Figure 2-2. Observational geometry for SEASAT SAR. The mean ocean surface is the (x ',y ') plane. Wave phenomena are illustrated with the wave travelling along $\vec{K}$ at an angle ϕ to the y ' direction. In SAR parlance the x '-direction is referred to as the range or cross-track direction, while the y '-direction is referred to as the azimuth or along-track direction.

observational parameters for SEASAT SAR remain reasonably constant over the 100 km wide swath, e.g., the radar incidence angle θ' varies only about 6° ($23 \pm 3°$). In contrast, aircraft SAR images, even from high altitudes, cover much smaller swath widths and the observational parameters vary much more widely over the swath. For example, an aircraft SAR flying at 25,000 ft. (7.6 km) altitude covers a swath only 10 km wide for incidence angles from 0 to 55°. Further, an aircraft flying at 400 knots requires about 8 minutes to fly 100 km while the SEASAT satellite requires only about 15 seconds to traverse the same distance. The point here is that a satellite SAR image is significantly different from an aircraft SAR image and thus large scale features so evident in satellite SAR images are not necessarily so obvious in aircraft SAR images of the same area.

Here in Section 2 we focus on radar aspects of ship wake features in SEASAT SAR images. Review papers and reports by Beal et al. (1981), Fu and Holt (1982) and Vesecky and Stewart (1982) give more comprehensive and detailed information on SEASAT SAR images of the ocean.

2.2 Formation of SAR Images From Raw Radar Echo Data And Display Of SAR Images

2.2.1 Optical and Digital Imaging of SAR Scenes

The radar echo signal received by a synthetic aperture radar requires extensive manipulation before an image emerges. We shall refer to this image formation process as "imaging" and to manipulation of an SAR image after formation as image "processing." Both imaging and image processing may be done optically, (i.e., by an optical train, which is an analog system) or digitally (i.e., by digital computer manipulation of digital data). Optical imaging and processing of SAR data is relatively less expensive and faster, but also less accurate and less flexible. Digital imaging and processing of SAR data is relatively expensive and slower, but can produce the highest quality images with sophisticated corrections and accurate geographical registration. In general, for a 40 x 40 km SEASAT SAR scene optical imaging would cost tens to hundreds of dollars in a bulk run and take seconds of processor time. A comparable, digitally imaged scene would cost a few thousand dollars and take hours of processor time on a medium-sized computer, e.g., a Prime 750 with array processor. Digitally imaged scenes are generally required for detailed analysis of features such as ship wakes. Wake

features clearly evident in digital SAR images are often completely invisible in optical SAR images of the same ship wake. The key point here is that images of varying quality result from the same SEASAT SAR raw data depending on how the imaging process was done.

2.2.2 SEASAT SAR Images - Standard Data Products Optically Imaged at Jet Propulsion Laboratory

The standard data product image for SEASAT SAR was necessarily optically imaged because of the large throughput rate required to produce images for all the SEASAT SAR data collected, some 10^8 km^2. These images were delivered to NOAA for public distribution through the Environmental Data Information Service. The resolution in these images runs from 25 to 40 m. Portions of the SEASAT SAR data have been optically imaged elsewhere. For example, European SEASAT SAR passes were optically imaged at the Environmental Research Institute of Michigan (ERIM). These small special imaging runs done at ERIM, JPL, or elsewhere are usually superior in quality to the standard data product which was done first and under pressure to get a quick look at the data.

2.2.3 Digitally Imaged SEASAT SAR Data

Digitally imaged SAR scenes from SEASAT were first produced by Bennett and Cumming (1979) at McDonald Dettweiler and Associates in Vancouver, B.C. This company can provide high quality, digitally imaged SEASAT SAR scenes. Their computer algorithm, referred to as the "MDA" algorithm, has been installed on other computers, e.g. at DFVLR, Oberpfaffenhofen, W. Germany. Other digital imaging algorithms exist or are under development at the Royal Aircraft Establishment (RAE), Farnborough, England; The Norwegian Defense Research Establishment, Kjeller, Norway; Jet Propulsion Laboratory; Mitsubishi Electric, Japan; Johns Hopkins Applied Physics Laboratory, and the Naval Research Laboratory. These various digital imaging algorithms produce high quality images, but a particular algorithm may be tuned to emphasize speed at some sacrifice in quality. The RAE algorithm puts emphasis on quality and many of the images used as illustrations in this report were produced at RAE.

2.2.4 Properties of Digitally Imaged SAR Scenes

In SAR image formation there are many engineering trade-offs which improve image quality in some respect while increasing computation time and/or sacrificing quality elsewhere. For example,

the SEASAT SAR system gathered data such that images could be produced with a best practical resolution of about 25 m along the range direction and 6 m along the azimuth direction. Generally 4 of the 6 m resolution cells along the azimuth direction were incoherently averaged to produce a square resolution cell of 25 x 25 m resolution. Such an averaging process is referred to as '4 look' imaging along the azimuth direction. Some ship wake features may be entranced by using the 6 m resolution (see Fig. 2-4) or other imaging options available with a given digital processing algorithm.

Many subtleties of SAR image formation are discussed in a review by Tomiyasu (1978). An example of these subtleties which is important for satellite SAR images of ship wakes concerns "range cell migration." This term refers to the fact that for SEASAT SAR images Earth surface curvature and other effects cause a point target at given surface range (x'- coordinate in Figure 2) to migrate in echo time delay over the SAR's integration period (~ 2.3s for SEASAT). In order to calculate the doppler spectrum for a given range cell, the echo signal in <u>different</u> time delay cells must be used. Use of a crude single-step algorithm generates 'ghost' features in the SAR image as shown in Figure 2-3a. These ghosts can be removed by a more sophisticated algorithm to handle range cell

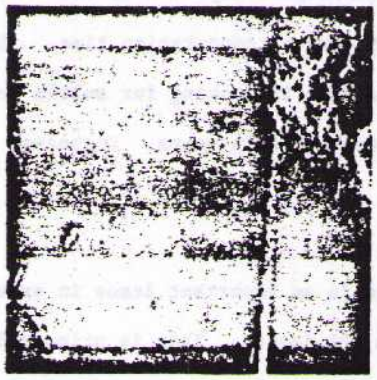

Note: (a) Shows a 4 x 4 km area near Goldstone, CA, where an array of nine corner reflectors were deployed in flat dry lake beds. The stronger echos from the two reflectors at the ends of the array show the side lobes in both the along track (↕) and cross track directions. For the digital imaging algorithm used by RAE to produce these images the first side lobe is 13.3 dB down. However, the photographic brightness in this figure is proportional to echo amplitude and thus in the figure the first sidelobe is only a factor 4.6 less bright than the peak. Note that for the two end reflectors there are two sets of sidelobes one of which is an artifact or ghost. The wide, nearly vertical stripe near the right side of 2-3(a) is the enormous sidelobe pattern created by the enormous echo from NASA's 210'Goldstone tracking antenna, located nearby.

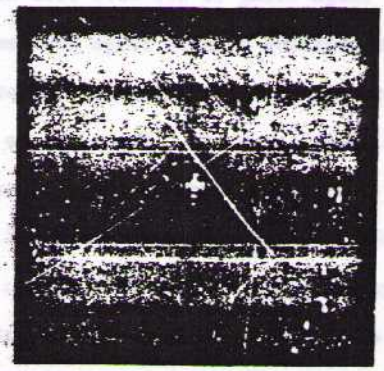

Note: (b) We see the SAR image of the lower left, corner reflector processed using a more sophisticated algorithm which suppressed the ghost sidelobe pattern. Use of the superior algorithm is said to "deghost" the image. RAE images used in this report (aside from 2-3(a)) are deghosted. Images kindly provided by Brian Barber at the Remote Sensing Centre, Space Department, RAE Farnborough.

Figure 2-3. SEASAT SAR images of corner reflectors near Goldstone, CA. In both images the SAR velocity vector runs parallel to the ordinate (i.e. y-axis of Figure 2-3 is vertical).

migration. Image quality is improved as shown in Figure 2-3b, but at the expense of increased computation time. 'Deghosted' images are clearly advantageous in looking for subtle features in the ocean surface phenomena such as ship wakes. Deghosted images are used in this report.

Dynamic range is an important issue in examining the physics behind features in SAR images. This is principally because photographic displays of SAR images can be misleading in terms of the relative radar backscatter cross section (σ^{o}) implied by dark and light portions of a photograph. For the SEASAT SAR the dynamic range of the receiver front end amplifier was about 60 dB (factor of 10^{6}). A digitized image using 16 bit word size has a dynamic range of about 45 dB. To overcome dynamic range problems some images are printed photographically with photographic tone proportional to the square root of SAR image intensity. These images are called amplitude images. Most of the images used here are amplitude images. Photographic film has a dynamic range of at best about 30 dB and a photographic print probably less than 20 dB. Hence, when one looks at a photographic print only a portion of the total dynamic range of the system can be displayed. It is usually a mystery just what the relative radar echo intensity is between the blackest black and the whitest white in a photographic print.

This brings up one of our principal recommendations, namely that examination of SAR data regarding ship wakes should be done using digitally imaged data in a digital format. By viewing such an image from a digital format via CRT display, an image can be manipulated in a known manner and the relative intensities of image features can be accurately known. Similarly photographic images generated from a digital format image using an appropriate algorithm can also be useful. By magnifying small areas of a digital format image, a photographic (or CRT) image can be generated which shows image pixels explicitly and their relative intensities clearly. The images presented in this report are photographs generated from digital format images of digitally imaged data. However, these images were printed as described below and are not necessarily optimized to show important wake features.

2.2.5 Contrast Stretched Images

In order to fit the larger dynamic range of a SAR image into the smaller dynamic range of a photograph, a data compression process called linear contrast stretching is often used. Depending on the particular image the stretching may be an expansion or a compression. The process described here is that used at RAE and corresponds to some of the figures used in this report. First, a

statistical distribution of pixel brightness is calculated. Here we use brightness B(x,y) to refer to the brightness of the photograph which may correspond to SAR image intensity I(x,y), i.e. to radar echo power, or to $\sqrt{I}$, i.e. to radar echo amplitude. Knowing the histogram or probability density function for B(x,y) over a 16 bit (0-65,535) count range consider a range from 0 to some percentile, e.g. 0-98.5% which contains 98.5% of the image pixels. This 0-98.5% range, which usually has a probability density peak at about 1000 to 2000 counts, is divided into 256 bins spaced linearly and these bins constitute the 24 dB dynamic range of the photograph. The lowest photo brightness bin incorporates the lowest intensity SAR image pixels as a black tone. However, the highest intensity SAR image pixels are excluded from the photograph. Many of the images displayed in this report use the 0-98.5% linear contrast stretch discussed here. Most other images use a linear contrast stretch, but the parameters and specifications vary.

Although a specific case is discussed here, it is clear that the photographic display of a SAR image can <u>compress</u> or <u>expand</u> the dynamic range of the pixels in the original image. Thus, until one has complete specifications of just how the contrast compression or expansion was done for a particular image, it is not possible to deduce the relative radar cross section variations displayed in a

photographic print of a SAR image. Why such specifications are not printed as part of the caption on all SAR image photographs is hard to understand. In any case, such information is readily accessible when a digitized image is read from magnetic tape and displayed on an image analysis system such as manufactured by Comptal or Sun.

2.2.6 Importance of Examining Digital SAR Image Data

Having discussed the risks of trying to draw conclusions from photographic prints of SAR images alone, we make the point again very explicitly that these pitfalls can be avoided by using the full dynamic range output of a digital SAR imaging system. This full dynamic range can be faithfully recorded on digital media, such as magnetic tape or disc, and subsequently displayed on a video display terminal. We emphatically recommend that such a system be used in further investigation of SAR images of ship wakes.

2.3 Features of SEASAT Ship Wake Images

While an exhaustive study of ship wakes in SEASAT SAR images was not within the scope of this study, we have examined some ten's of ship wake images from various sources. Below we describe features of these ship wake images which we believe are important in

discovering the physical mechanisms which produce the wake images. For the most part, these wake features are illustrated using images generated digitally at RAE. These images are of exceptionally high quality.

2.3.1 Classic Kelvin Wakes

The image of Figure 2-4, illustrating the classic Kelvin wake, was obtained on SEASAT orbit 834 in the English Channel southwest of the Isle of Wight. The dark linear feature parallel to the long axis of the ship is thought to be associated with the 'turbulent wake' of the ship. This makes sense since a linear stripe of relatively smooth water is often seen behind ships and such relatively smooth water would appear dark in a SAR image since it backscatters radar waves less well (at oblique incidence) than the rougher surrounding water. The ship (white oblong shape at right center) is displaced from its expected position at the head of the wake. This is a well known phenomena in SAR images since the ship is moving relative to the mean ocean surface. Taking the dark turbulent wake feature as the ship's track, we can calculate the ship's velocity from the relation

$$d = v_x x'/V \qquad (2\text{-}1)$$

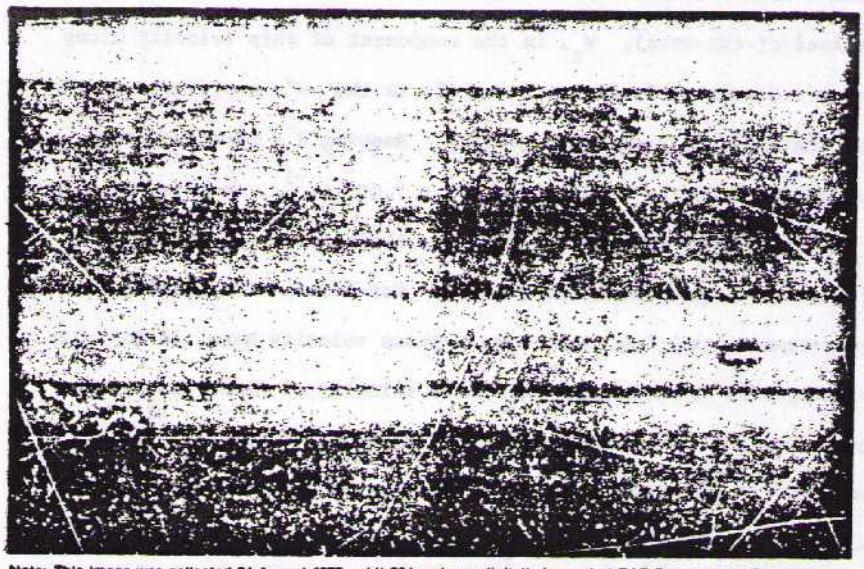

Note: This image was collected 24 August 1978, orbit 834 and was digitally imaged at RAE Farnborough. The SAR platform is moving from bottom toward the top at an angle 12.8° counterclockwise with respect to the ordinate of the figure and views the scene from left of the figure. The approximate processing resolution is $\Delta y \sim 6$m in azimuth and $\Delta x \sim 17$m in range. The image measures 8.1 km along the abscissa and 4 km along the ordinate. This image was kindly provided by Brian Barber of the Space Department, RAE Farnborough, U.K.

Figure 2-4. SEASAT SAR image of a large ship and a classical Kelvin wake in the English Channel off the Isle of Wight.

where d is the displacement of the ship from its true position (at the head of the wake), $v_{x'}$ is the component of ship velocity along the x'- direction in Figure 2-1, x' is the x'- coordinate of the ship and V is the satellite velocity. Knowing d = 564m (scaling from Figure 2-4), x' = 353,000m & V = 7,000 ms^{-1} , we have $v_{x'}$ = 11.2 ms^{-1}. Correcting for wake trajectory relative to $\vec{V}$, $v_{x'}$ = 11.5 ms^{-1} (or about 23 kts). For Kelvin wakes, the waves transverse to the ship track have a phase velocity equal to the ship velocity. We can calculate the phase velocity of these transverse waves from their observed wavelength (scaled from Figure 2-4), namely λ_t = 93m . From the deep water gravity wave dispersion relation the phase velocity $c_p = (g\lambda / 2\pi)^{1/2} = 12\ ms^{-1}$. So observationally the ship displacement and transverse wake wavelength are consistent to within about 5%.

Several other features of this Kelvin wake are of interest. First, the wake is a weak feature barely visible above the speckle noise of the image. Second, the line connecting the cusps of the wake (see Section 2.5 and Figure 2-12 for a wake description) in the upper half of the picture is dark relative to the background, while in the lower half, this line along the wave cusps is light on the outside and dark on the inside, i.e., this signature rises above, then falls below the background. The angles of both cusp lines are

(within the errors of measurement) at the classical angle of near 20°. The transverse waves of the wake are more evident in the upper than the lower half of the wake. Finally, (from Figure 2-4 and other images) the signature of the turbulent wake directly behind the ship becomes wider and more pronounced as one observes further astern of the ship, finally fading away some 7.5 km astern of the ship. Nothing definite about the ship aside from its observed speed, heading and length of some 260 m is known to the authors of this report.

2.3.2 Dark Turbulent Wakes

Perhaps the most common feature in SEASAT SAR images of ship wakes is the dark linear feature directly astern of the ship. As discussed in 2.3.1 above, it is reasonable to associate this image feature with the relatively smooth water of a ship's turbulent wake. As one can observe from the images shown here, it is evidently the most stable feature of ship wakes in SAR images. However, the turbulent wake signature is not always present, e.g., see Figure 2-5.

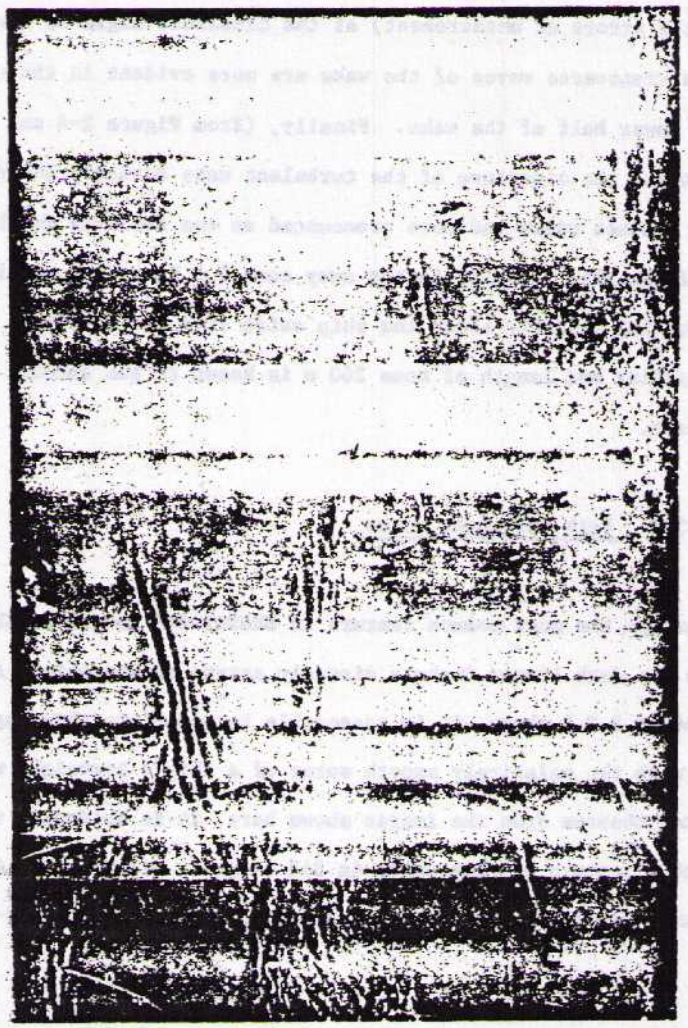

Note: This image was collected 25 July 1978 orbit 407 and was digitally processed at Jet Propulsion Lab. The SAR platform is moving from right to left parallel to the abscissa of the figure and views the scene from below the figure. The approximate processing resolution is $\Delta y' \sim 25$m in azimuth and $\Delta x' \sim 25$m in range. The image was kindly provided by Brian Barber at the Space Department, RAE Farnborough, U.K.

Figure 2-5. SEASAT SAR image of several large ships and very narrow wakes 40 km off the Florida coast near Cape Canaveral.

2.3.3 Wakes With Very Narrow Opening Angles

A very curious feature shown occassionally in SEASAT SAR images is illustrated in Figure 2-5. Here two bright lines form an opening angle of only some 6° and no turbulent wake is evident. Further there is structure in the upper arm of the wake showing several, roughly parallel, linear features. Perhaps most remarkable is the length of 20 to 25 km. From the size of the ship, it is likely to be a bulk cargo carrier. Based on a rather small number of observed cases, it seems that narrow angle wakes occur when the velocity vector of the ship is fairly near the direction of the SAR platform movement (y'- direction in Figure 2-1). To the author's knowledge no narrow angle wakes have been observed for ships travelling nearly perpendicular to the SAR platform movement (x'- direction in Figure 2-1).

There has been some confusion regarding the water depth below the ship in this figure. Estimates range from 20 to 100 or 200 fathoms. Using nautical charts and the full JPL digital image (≈ 100 x 100 km) we estimate the depth at 20 to 25 fathoms consistent with the estimate of McCandless (1984). There is some uncertainty in the estimate because only a small portion of the coast line appears in the image. A more sophisticated estimate of

ship position using spacecraft orbit and altitude data, etc. was made at RAE Farnborough and confirms the 20-25 fathom estimate.

2.3.4 Wakes With Intermediate Opening Angles

In addition to the very narrow wakes of Figure 2-5, and the classical Kelvin wake of Figure 2-4, there are wake images from SEASAT SAR with intermediate opening angles. Figure 2-6 illustrates these sorts of wakes with total opening angles of about 22 to 25°. It is interesting that this fleet of small fishing boats produces very similar wake images in each case. The dark turbulent wake features are absent. In this image, the SAR platform moves vertically from bottom to top and looks from the left of the image. Since the boats are moving nearly along the direction of the SAR platform (presumably at ~ 10 kts.), we observe little of the displacement of the ship from the wake which is so pronounced in Figure 2-4. We would expect maximum displacement of boat from wake for the boat at lower left and indeed it appears that the strong boat echo is displaced vertically upward nearly along the left arm of the wake. Compare the lower left boat and wake with the boat and wake at upper right when the strong boat echo (including sidelobe structure as in Figure 2-2) clearly stands near the vertex of the

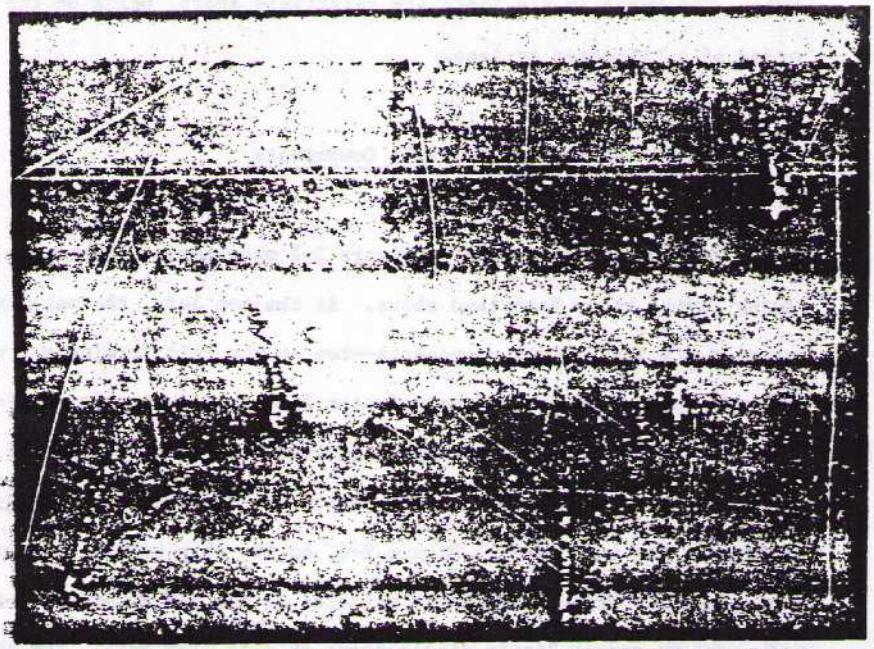

Note: This image was collected on 10 August 1978, orbit 633 and digitally imaged at RAE Farnborough. The SAR platform is moving from bottom to top, parallel to the vertical axis of the figure, and views the scene from left to the image. The approximate processing resolution is $\Delta y' \sim 6$m in azimuth and $\Delta x' \sim 18$m in range. The image measures 3.1 km along the abscissa and 2.3 km along the ordinate. The image was kindly provided by Brian Barber at the Space Department, RAE Farnborough, U.K.

Figure 2-6. SEASAT SAR image of fishing fleet in the Irish Sea off Ballyquintin Pt., east coast of Northern Ireland.

wake. The wakes in the image are relatively short, being on the order of a kilometer or less.

2.3.5 Wakes With Multiple Components

Two wake images shown in Figure 2-7 show curious features going beyond those described above. At the top left, the wake image shows 3 distinct bright components—two on the left forming a V with a $\sim 5^0$ opening angle and one brighter line running nearly vertically in the figure. This bright line forms an opening angle of $\sim 20^0$ with the nearer arm of the narrow V. The viewing geometry is virtually the same as with Figure 2-6, so the ship making this wake is apparently travelling nearly parallel to the SAR velocity vector $\hat{V}$, and we expect little displacement of ship from wake. The ship image itself appears aligned with the isolated and very bright arm of the wake. No dark turbulent wake is visible. Note that the background against which this wake is viewed is very dark indicating a very calm sea surface, i.e., low wind speed.

At bottom left of Figure 2-7, we find a ship moving almost directly away from the radar. As in Section 2.3.1 above, we calculate the ship's speed from the displacement between the ship and the turbulent wake. The displacement $d \approx 250m$; hence $V \approx 6m/s$

41

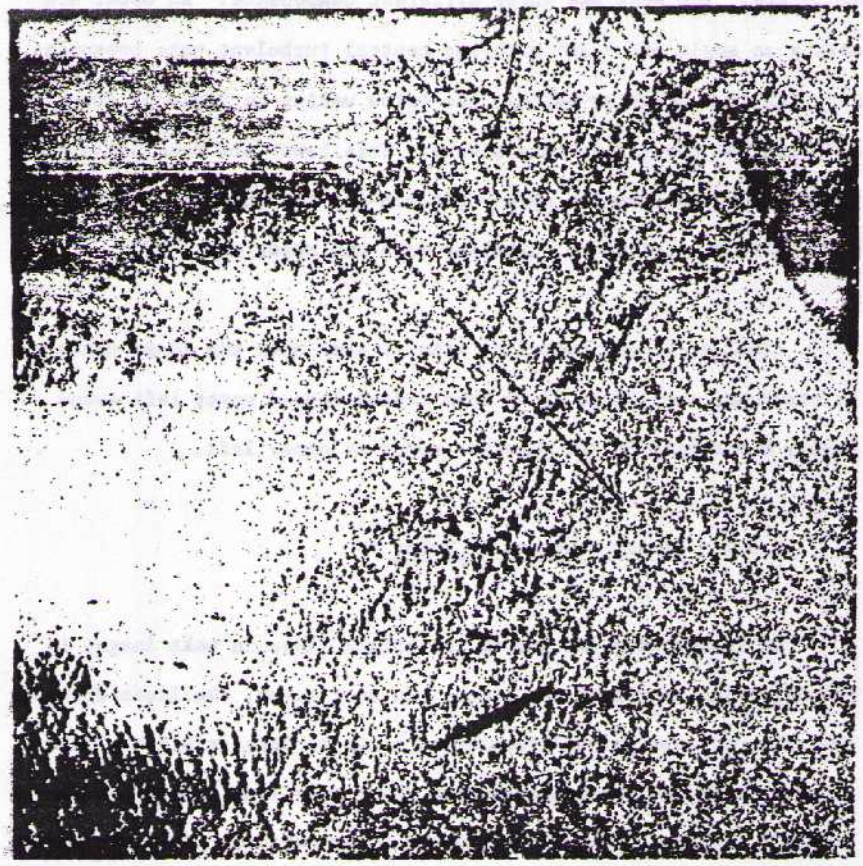

Note: This image was collected on orbit 782, 19 August 1978 and digitally imaged at RAE Farnborough. The SAR platform is moving from bottom to top, parallel to the vertical axis of the figure, and views the scene from left of the image. The approximate processing resolution in $\Delta y' \sim 25$m in the azimuth direction and $\Delta x' \sim 23$m in the range direction. The image measures 31.25 km along both the abscissa and the ordinate. The image was kindly provided by Brian Barber at the Space Department, RAE Farnborough, U.K.

Figure 2-7. SEASAT SAR image showing wakes with multiple components in the Mediterranean Sea south of Monaco.

or 12 kts. The wake has three different components: an upper arm making an angle of ~ 20^0 with the central turbulent wake component, and finally a brighter patchy line below making an angle of about 17° with the central turbulent wake. This lower arm does not appear to be displaced from the ship--this arm and the ship both appear to be displaced relative to turbulent wake and upper arm.

Finally, a long turbulent wake is seen near the image center. It stretches some 20 to 25 km from center toward upper left eventually dispersing in the smoother water at upper left.

2.3.6 Linear Features in Wakes

An interesting feature of the bright lines in wake images is the very fine nature of the lines. In most cases, the lines forming the wake are some several resolution cells or less in width. This suggests that the phenomena causing these very fine lines is very narrowly confined spatially along the water surface. This suggests a sharply "resonant" phenomena. Hence one's attention is directed toward items in wake hydrodynamics, radar wave scattering from the sea surface and SAR system response which show a strong functional dependence on some relevant parameter. One example is the dependence of radar backscatter from a rough surface on angle of

incidence (θ'). At angles of incidence near the mean value for SEASAT $\theta' \sim 23^{\circ}$, many experiments (see Valenzuela, 1978) show that a change in θ' of $\sim 3^{0}$ can cause a change in backscattered power of a factor of 2.

2.4 Radar Backscatter From The Ocean

2.4.1 Scattering Mechanisms

Scattering of electromagnetic waves from a rough surface is a difficult problem and is amenable to analytic treatment only over a limited range of conditions. Thus, even if one could specify the ocean surface exactly, calculating the radar echo from this surface analytically could still be difficult. We point this out because some 'simulated SAR images' have simply been plots of some ocean surface property and did not include the radar wave scattering part of the problem. These comments notwithstanding, analytical models are clearly very helpful and are reasonably accurate over a wide range of conditions. Below we briefly discuss some analytical models for electromagnetic wave scattering from the ocean surface and comment on their relevance to the imaging of ship wakes. An excellent review of these mechanisms is given by Hasselmann et al. (1984).

2.4.1.1 Bragg Resonance Scattering. In this mechanism, the incident radar wave resonates with a 'lattice' of ocean surface waves which satisfy a Bragg resonance condition, namely

$$\hat{K}_b = \pm 2\, \hat{k} \sin\theta \,, \qquad (2\text{-}2)$$

where K_b is the Bragg resonant wavenumber and k the incidence radar wavenumber. This is the first order Bragg resonance which generally dominates this scattering process. However, in some circumstances higher order resonances may be important especially if the directional distribution is broad and/or anisotropic. In this Bragg resonance process the radar wave acts as a filter on the surface roughness selecting out waves which have a wavelength $\Lambda_b = \lambda/(2 \sin\theta)$ (where λ is the radar wavelength) and are traveling either directly toward or away from the radar. The radar backscatter cross section resulting from this process can be written (Wright, 1968) as

$$\sigma^0(\theta', k)_{ij} = 16\, \pi^2 k^4 \cos^4\theta' \left| g_{ij}(\theta', \epsilon_r) \right|^2 \psi(K_{x'}, K_{y'}) \qquad (2\text{-}3)$$

where ψ is the directional waveheight spectrum evaluated at $K_{x'} = 2k \sin\theta$, $K_{y'} = 0$, g_{ij} is the radar reflectivity of a planar air-sea water interface, and ij denotes the incident and backscattered polarisations. For the SEASAT SAR ij = HH, i.e., horizontal polarization. The most important feature of equation (2-3) is that σ^0 is proportional to the waveheight variance spectrum evaluated at a specific $\hat{K}$ and is thus proportional to the energy in the Bragg resonant waves.

This scattering process is thought to dominate microwave backscatter from the ocean at $\theta' \approx 20^0$ to 70^0 as shown in Figure 2-8 where the Bragg resonance model is labeled as the 'slightly rough' curve. Strictly speaking this model is valid only for a slightly rough surface in the sense that $|k\zeta \cos \theta'| << 1$ where ζ is the rms height deviation. The Bragg-resonance model is supported not only by the argeement with observations shown in Figure 2-8, but also by measurements of the radar echo frequency spectrum which show strong peaks at frequencies corresponding to the expected Doppler shift of the first order Bragg waves (Graf, et al. 1977). Some evidence for higher order phenomena were presented by Gotwols et al. (1984).

2.4.1.2 Quasi-Specular Scattering. This scattering mechanism applies to situations where ζ may be large, but the surface is gently undulating (radius of curvature >> radar wavelength). The term quasi-specular refers to scattering from a statistical ensemble of facets (with randomly distributed normals) some of which are oriented so as to backscatter via specular reflection (for reference see Bass & Fuks, 1979, chapter 7). With reference to the ocean surface this mechanism is thought to dominate microwave backscatter from the sea at $\theta' \lesssim 20^0$, i.e., at near normal incidence. The radar cross section for the quasi-specular mechanism is given in concise form by Kodis (1966) as

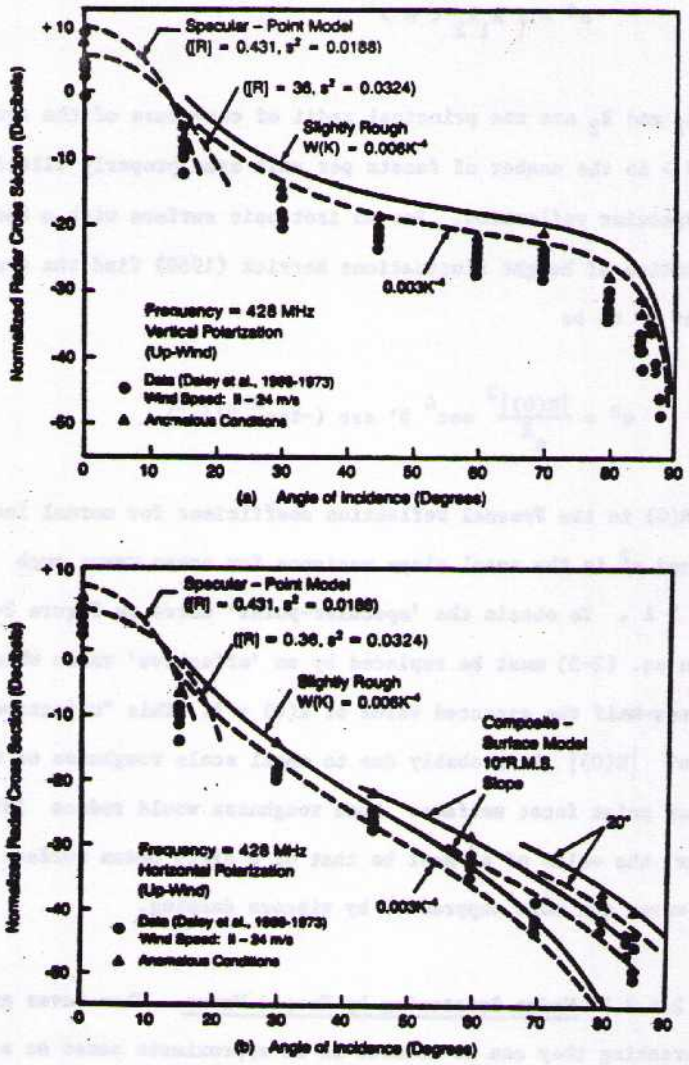

Figure 2-8. Comparison of measured and model calculations of the radar backscatter cross section of the ocean at 4.5 GHz for (a) vertical and (b) horizontal polarization. After Valenzuela (1978).

$$\sigma^0 = \pi \overline{R_1 R_2} < N > \qquad (2\text{-}4)$$

where R_1 and R_2 are the principal radii of curvature of the surface and $< N >$ is the number of facets per unit area properly tilted to yield specular reflection. For an isotropic surface with a Gaussian distribution of height fluctuations Barrick (1968) find the quasi-specular σ^0 to be

$$\sigma^0 = \frac{|R(0)|^2}{s^2} \sec^4 \theta' \exp(-\tan^2 \theta'/s^2) \qquad (2\text{-}5)$$

where R(0) is the Fresnel reflection coefficient for normal incidence and s^2 is the total slope variance for ocean waves such that $A > \lambda$. To obtain the 'specular-point' curve in Figure 2-8, R(0) in eq. (2-5) must be replaced by an 'effective' value which is about one-half the expected value of $R(0) \sim 1$. This "effective" value of $|R(0)|$ is probably due to small scale roughness on the specular point facet surface. Such roughness would reduce $|R(0)|$. Further, the value of s^2 must be that of a dirty ocean surface where short waves are more suppressed by viscous damping.

2.4.1.3 Wedge Scattering by Cusped Waves. When waves are near breaking they can be modeled in an approximate sense as a wedge having a 120° included angle corresponding to the limiting slope for

surface gravity waves. Scattering from the edges of such wedges (local radius of curvature << radar wavelength) can be treated analytically. If one distributes wedges randomly over a model ocean surface with an appropriate density, backscattering from cusped waves may be estimated. Lyzenga et al. (1983) have performed such a calculation. Their results show that backscattering from cusped waves is important at large angles of incidence. Comparison with ocean backscatter measurements shows that for horizontal polarization at X-band, wedge scattering from cusped waves dominates σ^0 at $\theta' \geq 60^0$ and agrees much better with measured σ^0 for high winds ($U > 10$ m/s). At L-band for horizontal polarization the cusped wave model again dominates backscattering for $\theta' \geq 60^0$, but yields a σ^0 somewhat above measured values. Wedge backscattering from cusped waves is not important for vertical polarization except for θ' very near grazing incidence where shadowing may very well reduce its importance.

2.4.1.4 Two-scale Scattering Models. Two-scale scattering models are almost always used in calculating the radar backscatter characteristics of the ocean surface. In connection with SAR images of ocean surface phenomena two distinct two-scale models are relevant: the electromagnetic-hydrodynamic (emh) model and the SAR model. In both these models radar backscatter is fundamentally due

to radar wave interaction with small scale roughness ($\lesssim 10\ \lambda$). However, the large scale behavior of the ocean is allowed to influence the properties of this small scale roughness in particular ways. The dichotomy between large and small scale ocean surface behavior is illustrated in Figure 2-9.

In the emh two-scale model Bragg resonance scattering arises from the small scale roughness ($K_b >> K_{emh}$ where K_{emh} is the separation wavenumber for this model). The behavior of these small scale ripples is governed in terms of a spectral transport equation where the large scale waves advect the small scale waves by their orbital velocities and refract them due to horizontal shear in the orbital velocities of the long waves. A spectral transport equation could incorporate source terms corresponding to generation by wind, energy loss due to damping and energy transfer via wave-wave (non-linear) interaction.

The SAR two-scale model divides the wave spectrum at the SAR resolution scale size (K_{sar}). Large waves ($K < K_{sar}$) are treated deterministically and small waves ($K > K_{sar}$) are treated statistically. As it turns out, the two models may be combined by statistically averaging the results of the emh model over the intermediate scale waves shown in Figure 2-9.

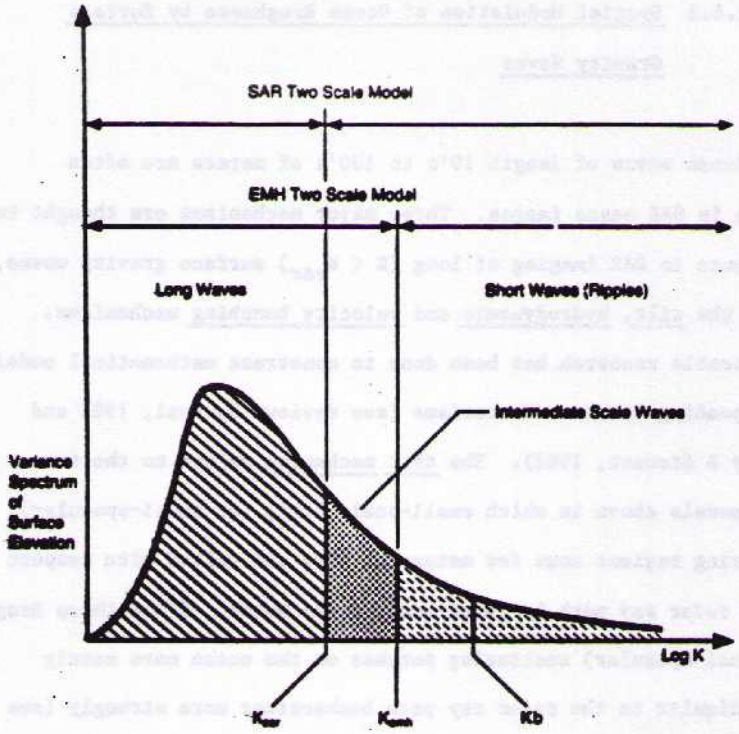

Figure 2-9. Dichotomy of ocean surface behavior into large and small scales divided by a separation wavenumber (K_{emh} for the emh model, K_{sar} for the SAR model). The first-order Bragg resonant wavenumber $K_b = 2\ k \sin\theta$. Generally $K_{sar} < K_{emh} < K_b$ and for SEASAT $K_{sar} \approx (2\ \pi/25)m^{-1}$, $K_{emh} \approx (2\pi/3)m^{-1}$ and $K_b \approx (2\pi/0.3)m^{-1}$. Figure after Hasselmann et al. (1984).

2.4.2 Spatial Modulation of Ocean Roughness by Surface Gravity Waves

Ocean waves of length 10's to 100's of meters are often visible in SAR ocean images. Three major mechanisms are thought to contribute to SAR imaging of long ($K < K_{ear}$) surface gravity waves, namely the tilt, hydrodynamic and velocity bunching mechanisms. Considerable research has been done to construct mathematical models corresponding to these mechanisms (see reviews by Beal, 1982 and Vesecky & Stewart, 1982). The tilt mechanism refers to the two-scale models above in which small-scale Bragg (or quasi-specular) scattering regions some few meters in size are tilted with respect to the radar ray path by large-scale ocean waves. Since those Bragg (or quasi-specular) scattering patches on the ocean more nearly perpendicular to the radar ray path backscatter more strongly (see Figure 2-8), they are brighter in the image. Thus, for ocean waves approaching the radar the portion of the wave somewhat in advance of the crest would appear brightest and the portion somewhat following the crest would appear darkest. The hydrodynamic mechanism refers to the straining of the water surface by a passing large-scale wave. The region somewhat in advance of the wave crest experiences a velocity convergence which compresses ambient small-scale waves, thus raising their amplitude and hence their radar cross section

(see eq. 2-3). This portion of the wave should then appear brighter in the SAR image. The velocity bunching mechanism is a phenomenon unique to SAR since it relies on Doppler shift. The Doppler shift introduced by the relative motion between the SAR platform and a SAR pixel's surface location allows the SAR to correctly associate back-scattered energy with a given pixel location. The orbital velocity associated with a large-scale wave introduces a periodic perturbation of the basic Doppler shift, and thus periodically shifts, i.e., misplaces, SAR image brightness along the azimuth direction (y'- direction in Figure 2-2). This periodic misplacement could then produce a wave image in the SAR output. There are other mechanisms which could conceivably affect SAR imaging of ocean waves, e.g., cusped waves, breaking waves, foam, etc. However, no quantitative investigations of these mechanisms have yet been done.

The modulation transfer function R relates the change in radar cross section ($\Delta\sigma^o$) associated with a large-scale ocean wave to the wave's physical characteristics by

$$\frac{\Delta\sigma^o}{\sigma^o} = |R|\, A \cos\left(\vec{K} \cdot \vec{r} - \Omega t + \gamma\right) \qquad (2\text{-}6)$$

where $\gamma = \arctan\left[\mathrm{Im}(R)/\mathrm{Re}(R)\right]$ and A, $\vec{K}$ and Ω are the long wave's amplitude, vector wavenumber and frequency; $\vec{r}$ is distance in the

(x', y') plane. It is interesting to note that when R is calculated as a function of θ' for the tilt mechanism alone, there are two maxima and one maximum is near $\theta' \approx 20^0$, i.e., near the angle of incidence at which SEASAT SAR operated (Bahar, 1983c and Vesecky et al., 1983). This implies that SEASAT SAR was particularly sensitive to small tilts of the ocean surface. Comparing the general visibility of ocean wave fields between the first shuttle imaging radar (SIR-A) which operated at $\theta' \sim 45^0$ and SEASAT we find waves much more prevalent for SEASAT in agreement with the above implications. Further, the aforementioned calculations of R indicated that quasi-specular as well as Bragg-resonance scattering were important for SEASAT SAR observations of ocean waves.

2.4.3 Spatial Modulation of Ocean Roughness by Internal Waves

One of the surprises of the SEASAT mission was the almost ubiquitous nature of internal wave surface effects in SAR ocean images. Particularly along coasts (out to the continental shelf) and over sea mounts strong SAR images of internal wave packets were very frequently observed. An example is shown in Figure 2-10. In many cases, such as Figure 2-10, internal waves are presumably associated with strong tidal currents as they encounter shallow water near coasts.

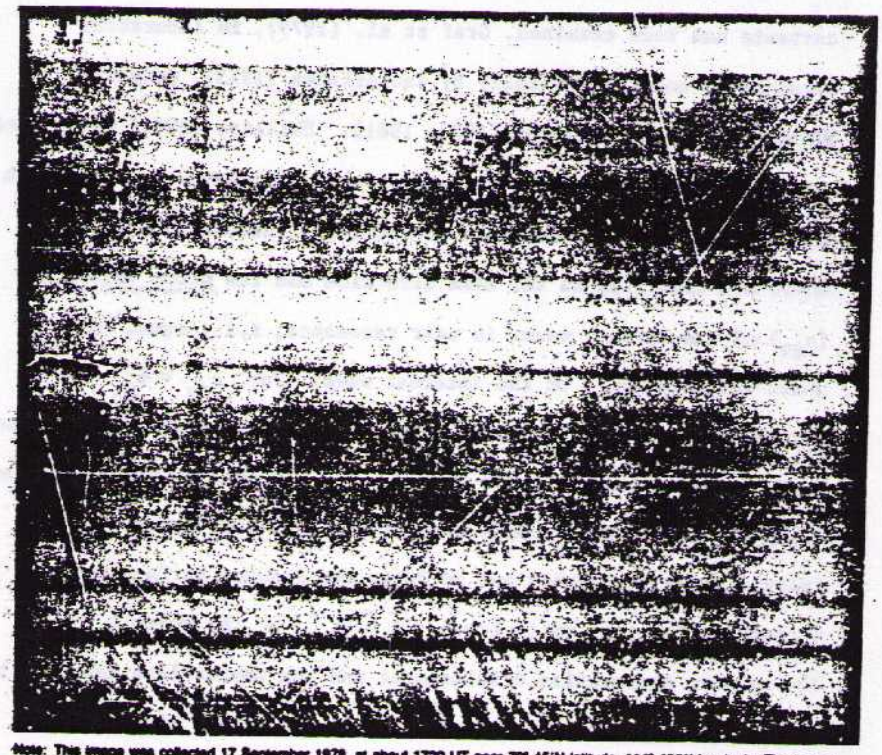

Note: This image was collected 17 September 1978, at about 1720 UT near 79° 45'N latitude, 114° 40'W longitude. The image is approximately 100 km top to bottom. The wavelengths in the internal wave packets range from about 0.5 to 5 km. The white specks are defects in the archive negative. Spacecraft ground track was parallel to the bottom of the image going from right to left along 340°. This digital image was kindly provided by Jet Propulsion Laboratory.

Figure 2-10. SEASAT SAR image (orbit 1183) of internal waves off the island of Angel de la Guarda in the Gulf of California.

Modulation of surface waves by internal waves and surface currents has been examined, Graf et al. (1979), in laboratory experiments and theoretically by Zachariasen (1973), Gargett & Hughes (1981) and Phillips (1973, 1981). Phillips (1981) notes that small-scale Bragg resonant surface waves can interact strongly with internal wave surface currents provided the internal and surface waves are traveling in the same direction and the group velocity (c_{gs}) of the surface waves is near resonance, i.e., equal to, the phase velocity (c_{pi}) of the internal wave. For $c_{gs} = c_{pi}$ internal-wave induced surface currents can modulate the SAR resonant surface waves, i.e., ripples with $K = K_b$. In shallow water, such as along the continental shelf, near islands and over sea mounts, internal wave amplitudes can be large and induced surface current velocities (u) also quite large, $u = (\zeta_{max}\, c_{pi}/h)$ where ζ_{max} is the maximum thermocline displacement and the thermocline depth is h. Large u means significant modulation of small-scale ripples can occur over a wider range of $(c_{pi} - c_{gs})$ and SAR detection of the resulting σ^0 modulation is more likely. Nevertheless, Phillips (1981) finds it remarkable that internal wave images are so frequently observed by SEASAT SAR in continental shelf waters.

One clear implication of the mechanism discussed above is that internal waves traveling approximately in the range direction (y'-

direction in Figure 2-2) are more likely to be imaged than those traveling along the azimuth (or x'- direction in Figure 2-2). Indeed this phenomena occurs in Figure 2-10 where we observe very bright wave crests for internal wave packets traveling approximately in the range direction at center right and upper right. Why should this be so? The group velocity of Bragg resonant waves for SEASAT SAR is ~ 35 cm/s. Typical internal wave phase velocities are also ~ 10's of cm/s. So if the internal wave is traveling in nearly the same direction as the Bragg resonant ripples, then relatively strong interaction between the two is likely and relatively strong modulation of surface roughness at $\Lambda \sim \Lambda_b$ is likely to occur. In Figure 2-10 we expect this to occur for internal waves traveling approximately along the ordinate of the figure. We associate the bright wave packet features mentioned above with this mechanism for modulation of small-scale surface roughness particular because the bright portions of the wave packet rise significantly above the background $\langle \sigma^0 \rangle$. Internal waves packets traveling in other directions in Figure 2-10 tend to be more a darkening relative to the background $\langle \sigma^0 \rangle$.

The mechanism described above would tend to <u>enhance</u> SAR image brightness over regions of internal-wave induced downwelling (converging surface currents) and visa-versa for upwelling regions.

Similar enhancements would be produced if some type of radar backscattering objects; such as flotsam, foam, debris, etc; were concentrated by the downwelling.

An alternative mechanism would have surface films being concentrated in current-convergence regions, damping the local SAR resonant ripples and hence reducing SAR image brightness. In current divergent regions the dispersal and breaking of surface films would allow higher energy density levels of SAR resonant waves and hence a SAR image brightness at the background level or above. We suggest that this process might dominate for the internal waves traveling more nearly along the abscissa in Figure 2-10 since the SAR resonant ripples would be traveling nearly perpendicular to the internal wave surface currents and thus would not interact strongly with them.

At present the question of a physical mechanism for the visibility of internal waves in SAR images must remain open for two reasons. First, to the author's knowledge, no theoretical attack has yet been mounted incorporating both the necessary hydrodynamics and radar scattering theory. Second, no experimental data set containing both SAR and appropriate in-situ hydrodynamic measurements has yet been analyzed. Data from Boundary Passage collected

during the Georgia Strait experiment provide the opportunity to attack the latter point of the two mentioned above.

Some interesting empirical data from a comprehensive survey of SEASAT SAR images of natural internal waves in the northeast Atlantic was presented by Bagg (1983). After examining some 5×10^6 km^2 of SAR images in this region Bagg concluded that:

a. Internal wave surface features can be imaged by SAR in water depths ranging from very shallow to very deep.
b. Internal wave surface features can be imaged with winds ranging from light airs to gale force.
c. The likelihood of imaging internal waves with SAR decreases with increasing water depth and/or wind speed.
d. The effect of increasing wind speed causes an increasing limitation on internal wave imaging as the water depth increases.

Further information on internal wave images in this region is supplied by Kasischke et al. (1983).

2.4.4 Other Surface Roughness Modulation Observed by SAR

2.4.4.1 Winds. Since surface wind stress is the primary source of radar resonant ripples, radar σ^0 is clearly a function of local wind speed. Since radar measurement of ocean winds is normally done at K_a band ($\lambda \sim 2$ cm), little work with L-band ($\lambda \sim 20$ cm) SAR has been done. Vesecky and Stewart (1982) review research in this area. Two principal research results standout:

a. SAR σ^0 at L-band is only weakly dependent on wind speed, σ^0 being approximately proportional to U_b^γ where U is the neutral stability wind at height b above the surface and
$\gamma = 0.2$ for $b = 10$ m and $\gamma = 0.4$ for $b = 19$ m.

b. SAR σ^0 at L-band is insensitive to wind direction. (Although roll instabilities may cause large scale, ~ few km, structures aligned with the wind direction.)

However, this relatively weak sensitivity of σ^0 to wind speed does not prevent regions of differing wind speed from being very

evident in SAR images. Examples in Beal et al. (1981) and Lyden et al. (1983) aptly demonstrate this point.

2.4.4.2 Surfactants. It is well known that surfactant films strongly damp surface waves. For example, Phillips' (1977) calculations indicate that Bragg resonant waves for SEASAT SAR ($A_b \sim 30$ cm) have an energy density decay (e-folding) time of $\tau \sim 450$ s for a perfectly clean ocean surface, but $\tau \sim 16$ s for a surface covered by an inextensible surface film. Features in SAR images which are apparently related to slicks are commonly seen. A particularly striking example is shown in Figure 2-11 where a ship is apparently discharging oil. Little experimental research utilizing SAR images and surfactants with measured characteristics has been done. Huhnerfuss et al. (1983) report experiments with mono-molecular films observed by L and X-band aircraft SAR. Surfactant films reduced X-band radar cross section by a factor of ~ 15 to 200% ; while L-band cross section was reduced by about 20%. Differing chemical structure in the surfactant does alter the effect on radar cross section. Further, Huhnerfuss et al. (1981) have investigated the fundamental issue of surface wave attenuation by artificial surface films of different chemical structure.

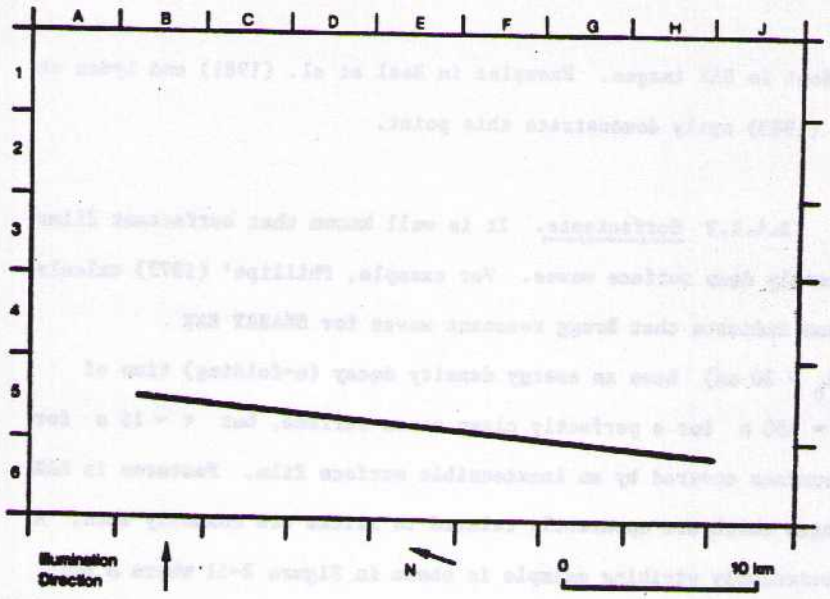

Figure 2-11. Ship in the Atlantic ocean apparently discharging oil or other surfactant which damps the surface ripples to which SAR is sensitive. This image was collected 19 Sept. 1978 at 1442 GMT about 500 km out from Delaware Bay by SEASAT SAR on orbit 1210. After Fu & Holt (1982).

2.4.4.3 Spray, Foam and White Caps. Spray, foam and white caps can clearly contribute to microwave scattering from the ocean surface. However, not much is known quantitatively about these processes. SAR images of breaking waves indicate that the bright wave crests are observed by the SAR at a Doppler frequency corresponding approximately to the wave phase velocity (Lyzenga, et al., 1984).

2.5 SAR System and Wave Scattering Effects Upon Ship Wake Images

2.5.1 Effects Upon Wakes in General

There are several SAR system and wave scattering effects which are relevant to SAR ship wake images irrespective of the physical mechanisms which cause the wakes to be imaged. These are discussed first in this section while other items associated more specifically with surface or internal waves are covered later in Sections 2.5.2 and 2.5.3, respectively.

2.5.1.1 Contrast Stretching and Fine Wake Features.

Curiously the linear features which form the bright lines in SAR ship wake images are very fine, i.e., very narrow. Estimates of the width of these lines run to several SAR resolution cells or less. If indeed these lines are very fine features contrasting strongly with the background, then this is an important feature of SAR ship images that must be explained by any candidate model for the wake imaging mechanism. However, many of the estimates of wake feature characteristics are based on photographic prints which have undergone a "contrast stretching" process described in Section 2.0 above. This process could give the impression that wake lines are very fine, high contrast features when in fact the backscattered energy

returned by the features could be only tens of percent above the background. Therefore, it is necessary to know what contrast stretching has been applied to an image before making any conclusions regarding the fineness of wake features in the image. To make quantitative measurements of wakes images digital format data and image processing apparatus are required as discussed in Section 2.0 above.

2.5.1.2 Spatial and Temporal Limits to Coherent Scatter. Fresnel zone size (appropriately calculated) determines approximately the maximum size scale over which an individual scattering element (facet) on the ocean surface can backscatter coherently. In the temporal domain an element's backscattering properties must not fluctuate significantly over the integration time (T) of the SAR system in order to contribute coherently to the received SAR signal. While integration time for a SAR system can be varied (up to some maximum limit related to the system bandwidth) after signal collection, the Fresnel Zone size is fixed by the SAR wavelength and the observational geometry. Thus Fresnel zone size could be an important parameter in the scattering of SAR signals from the ocean. Fresnel zone size for a plane surface perpendicular to $\hat{k}$, the radar wave vector, is $= \sqrt{\lambda R/4}$.

TABLE 2-2

TYPICAL FRESNEL ZONE SIZES

SAR System	R	λ	$\sqrt{\lambda R/4}$	Typical Resolution
SEASAT	850 km	23 cm (L-band)	221 m	25 m
High Altitude Aircraft SAR	10 km	23 cm (L-band)	24 m	10 m
High Altitude Aircraft SAR	10 km	10 cm (X-band)	16 m	3 m
Low Altitude Aircraft SAR	3 km	23 cm (L-band)	13 m	5 m
Low Altitude Aircraft SAR	3 km	10 cm (X-band)	9 m	2 m

We see from the table that, in fact, SAR resolution cell size is usually much smaller than the Fresnel zone size. So, in practice, it is the SAR resolution cell size (discussed below) which limits the spatial scale of coherent backscatter.

2.5.1.3 Effects of Resolution Cell Size. Referring to Figure 2-9 we note that in the SAR two-scale model the wavenumber K_{sar} (= π/SAR resolution) separates the small scale waves $K > K_{sar}$ which must be treated statistically and the large scale waves

$K < K_{sar}$ which are resolved by the SAR and can be treated deterministically. For the Bragg resonance scattering mechanism the individual scattering facets (consisting of sets of ~ 10 resonant waves $A = A_b$) will be tilted by intermediate scale waves $K_{sar} < K < K_{emh}$. In some situations, e.g., horizontal polarization and angles of incidence $\theta' \lesssim 30^\circ$ it is important to average the contributions of the Bragg scattering facets over the slope probability distribution of these intermediate scale waves. Clearly the value of K_{sar} is a determining factor in this averaging process. This process is discussed further below.

2.5.1.4 Wave-Wave and Wave-Current Interaction Hydrodynamics. The action spectral density $N(\vec{K}, \vec{x}, t)$ $(= E(\vec{K})/\Omega'$, where E is wave energy spectral density and Ω' is the intrinsic wave frequency) is commonly used to describe the state of small ripples which interact with radar waves via Bragg resonance scattering. The radiation or action balance equation (a WKB approximation) describes how N is transported or radiated in space, time and wavenumber $(\vec{x}, t, \vec{K})$ upon interaction with a surface current $\vec{u}(\vec{x}, t)$ or other perturbation, to wit

$$\frac{dN}{dt} = \left(\frac{\partial}{\partial \tau} + \dot{\vec{x}} \frac{\partial}{\partial \vec{x}} + \dot{\vec{K}} \frac{\partial}{\partial \vec{K}}\right) N = S(\vec{x}, \vec{K}, t) \qquad (2\text{-}7)$$

[For references see Keller & Wright (1975), Alpers and Hasselman (1978) or Wright (1978).] The waves propagate in four-dimensional phase space along trajectories described by ray equations as follows

$$\dot{\vec{x}} = \frac{\partial \Omega}{\partial \vec{K}} \quad , \quad \dot{\vec{K}} = -\frac{\partial \Omega}{\partial \vec{x}}$$

where (2-8)

$$\Omega(\vec{\chi}, \vec{K}, t) = \Omega'(\vec{K}) + \vec{K} \cdot \vec{u}(\vec{\chi}, t)$$

and $\vec{u}$ is the current with which the waves of action density N are interacting. S is the source term describing energy input to and loss from the waves described by N.

In certain special cases, S = 0 and (2-7) becomes a more simple equation expressing the conservation of action spectral density. In this case, the waves propagate without energy gain or loss through the slowly varying medium. Phillips (1981) uses this case to describe the interaction of small $A \sim A_b$ ripples with long ocean waves. The interacting current $\vec{u}$ is the tangential surface velocity of the long wave at some given point. Further gravitational accelaration $g + g'$ where g' is the component of g normal to the long wave surface at the given point modified by the acceleration due to the long wave orbital motion.

If a perturbation approach (based on the ad hoc assumption that the action tends to return to an equilibrium state) is used with regard to N, $\hat{u}$, and S (Alpers and Hasselman, 1978), then the radiation balance equation (2-7) can be approximated as

$$\frac{dN}{dt} = -\mu \delta N \qquad (2\text{-}9)$$

where μ is the relaxation rate associated with a relaxation time $\tau_r = \mu^{-1}$ and δN is a perturbation in action spectral density with respect to a constant spectrum $N_o(\vec{K})$. The relaxation time is determined by the totality of energy gain and loss processes, such as wave generation by wind, energy exchange by resonant wave-wave interaction and energy loss by viscous damping and wave breaking. Notwithstanding a lack of knowledge of the physics of these processes, τ_r is thought to be of the order of 10 to 100 wave periods. For Bragg resonant waves in the case of SEASAT SAR $\Lambda_b \sim 30$ cm τ_r would be ~ 5 to 50 seconds. No experimental measurements of τ_r have yet been made in the open ocean to the author's knowledge. However, recent work by Alpers (1984) suggests that τ_r probably lies toward the upper end of the range.

The important point here is that for the interaction of Bragg resonant ripples ($\Lambda \sim \Lambda_b$) with currents due to gravity waves of

lengths like that of waves in a Kelvin wake or in ocean swell the source term S in (2-7) can be set to zero with some confidence and the spectral density conservation equation used. This is because the current associated with the long waves varies over a time scale $\lesssim (P/4)$ where P is the wave period, and this time is typically about an order of magnitude less than τ_r. Thus, the hydrodynamic interaction of Bragg resonant waves with long gravity waves is relatively weak since the currents associated with the long gravity waves do not act in a given direction for a long enough time.

Other surface currents may vary relatively slowly, i.e., on time scales much longer than τ_r. Hence, use of the $S \to 0$ approximation is probably not justified and the form (2-9) is appropriate. Work by Alpers (1984) on currents related to underwater typography in shallow depths suggests that analysis based on (2-9) (see, for example, Alpers and Hasselmann, 1978) would predict relatively strong modulation of Bragg resonant ripples and hence relatively strong radar cross section modulations due to equally strong currents associated, for example, with shallow water internal waves. Relatively here refers to the case of gravity waves in the paragraph above.

The important point here is that for gravity wave modulation of Bragg resonant ripples the surface currents can not act for a time comparable to τ_r and so S can be set to zero in (2-7). However, for slowly varying surface currents, the interaction time is probably much longer and the use of a source term is probably appropriate, e.g., equation (2-9). Experimental work suggested in Section 2.6 below could help sort out the role of S in describing the SAR imaging of internal waves. The approach to S described here is probably the simplist aside from letting S go to zero. Other treatments exist addressing particular source mechanisms, e.g. wind energy input to waves (Hughes, 1978).

2.5.2 Effects Associated with Kelvin Wakes

2.5.2.1 Elementary Properties of Kelvin Wakes. Dashen et al. (1982) give a concise review of the properties of Kelvin wakes. Further information is given in Section 4.0 of this report and by Lighthill (1978) and references therein. To make matters clear, we reproduce a convenient illustration from Dashen et al. as Figure 2-12. First, we remark that the classical solution to the Kelvin wake problem, used here to illustrate several points, is an idealized model of a real ship wake. Hence, we expect that elementary calculations made here will have to be modified

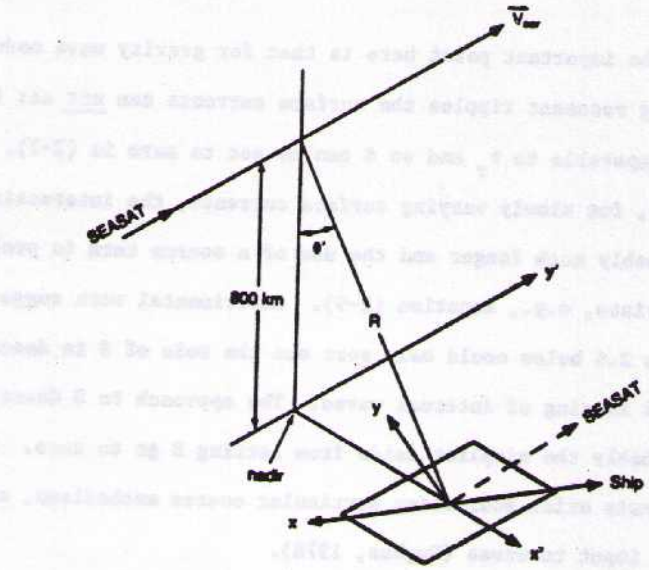

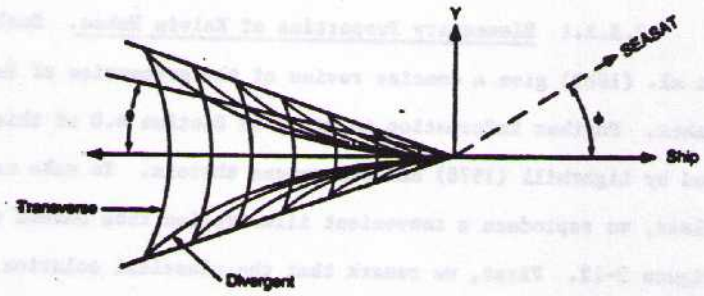

Figure 2-12. First, we remark that the classical solution to the Kelvin wake problem, used here to illustrate several points, is an idealized model of a real ship wake. Hence, we expect that elementary calculations made here will have to be modified significantly in order to apply to a real ship wake. Further, we Figure 2-12: SEASAT SAR Observes a ship's Kelvin wake. The ship is moving at an angle ϕ relative to a line parallel to the SEASAT velocity vector. The SEASAT angle of incidence is $\theta' \sim 23°$. Adapted from Dashen et al. (1982).

significantly in order to apply to a real ship wake. Further, we note that many ships utilize modified bows which reduce the wave drag on the ship, and hence modify the Kelvin wake pattern; for example, reducing the wave height of the long wavelength waves near the cusps.

Perhaps the most important feature of the Kelvin wake pattern is the similarity of the wake form along a line of constant θ (see Figure 2-12). First, the orientation (in the x,y plane) of the divergent or transverse wave crests (or any locus of constant wave phase) is constant along constant θ. Second, the wavenumber of the waves in either the divergent or transverse wakes is constant along a line of constant θ. As Dashen et al. (1982) point out, these properties would lead to a V-shaped wake if there is some selection process which leads to a local maximum of σ_o at a given wavenumber K or crest orientation.

2.5.2.2 Quasi-Specular and Bragg Resonance Backscatter. Bahar et al. (1983a,b,c) discuss radio wave scattering from rough surfaces which is relevant to the ocean. This work is a comprehensive treatment of rough surface scattering in that the formalism includes both the Bragg resonance and quasi-specular mechanisms is a self-consistent manner as well as shadowing effects important at

large angles of incidence. Further, this theory claims to handle a more general class of composite rough surfaces; namely, those that cannot be decomposed into small-scale surface perturbations (amenable to Bragg resonance theory) riding on a filtered large-scale surface (amenable to quasi-specular theory). A draw back of this formalism is that the mathematics are relatively complicated and hence not too useful in analytic work as they stand. However, suitable approximations can be made and reduce some expressions to tractable forms useful in analytic work. For example, under the appropriate restrictions, Bahar et al.'s formalism reduces to equations (2-2, 2-3 and 2-4) in Section 2.4 above.

Bahar et al. (1983c) calculate the backscatter cross section for arbitrarily oriented composite rough surface regions of limited extent. This is just the sort of information one needs to deal with the resolution cell sized patches observed by SAR within a ship's Kelvin wake.

Bahar et al. (1983a,b,c) view ocean surface height fluctuations $\zeta(x,y)$ as being composed of two components

$$\zeta(x,y) = \zeta_1(x,y) + \zeta_s(x,y) \qquad (2\text{-}10)$$

where 1 and s refer to large and small-scale spectral components. The mean radar cross section of the surface is thus given by

$$\langle \sigma^{PQ} \rangle = \langle \sigma^{PQ} \rangle_1 + \langle \sigma^{PQ} \rangle_s \quad . \tag{2-11}$$

where PQ refers to the received and transmitted polarizations, e.g., PQ = HH for SEASAT. The cross section from the large-scale components is given as

$$\langle \sigma^{PQ} \rangle_1 = |\chi^s (\hat{\nu} \cdot \bar{n}_s)|^2 \langle \sigma_m^{PQ} \rangle \quad . \tag{2-12}$$

χ^s is the characteristic function of the small scale surface structure (where for backscatter $\hat{\nu} = 2\hat{k}$ and $\hat{n}_s$ is the unit vector normal to the surface at a specular point). $\langle \sigma_m^{PQ} \rangle$ is the specular point cross section for the large scale surface. The expression for $\langle \sigma_m^{PQ} \rangle$ (Bahar et al., 1983c, p. 677) is somewhat involved, but analogous to eq. (2-4). The χ^s term reduces the cross section $\langle \sigma_m^{PQ} \rangle$ to account for the fact that the small-scale roughness (ζ_s in 2-10) makes the specular points less effective scatters (c.f. section 2.4.1.2 and Figure 2-8). For a Gaussian distributed rough surface ζ_s

$$\langle \sigma^{PQ} \rangle_s = \sum_{m=1}^{\infty} \langle \sigma^{PQ} \rangle_{sm} \quad . \tag{2-13}$$

The first term in this series $\langle \sigma^{PQ} \rangle_{s1}$, corresponds to the first-order Bragg scattering (c.f. eq. 2-3).

Although Bahar et al. do not calculate which term dominates in (2-10) under various conditions, Vesecky et al. (1983) have shown that for surface tilt modulation of σ^0, quasi-specular scattering is an important factor at the SEASAT angle of incidence. Although there is still a little controversy it is pretty clear that scattering from Bragg resonant ripples will be perceived by the radar as having a doppler shift corresponding to the small (~ 0.7 m/s) phase velocity of the Bragg waves themselves plus the comparable orbital velocity of the large waves which advect the small waves (Graf et al., 1977). However, it is not clear what doppler shift should be associated with the quasi-specular scattering process. Hasselmann et al. (1984) suggest that for quasi-specular scatter the long wave phase velocity is important. If this is so, wake waves scattering by the quasi-specular process would have substantial doppler shifts and the SAR process would misplace scattered energy by at least several resolution cells along the azimuth direction. We note that in most cases (e.g., Figure 2-4) the ship and its wake are not displaced together. This argues that the doppler shift of the ship and its wake are distinctly different. Further our calculations in Section 2.5.2.3 show that the size of the displacement of

the ship from its wake is very close to what one would expect from the ship's speed alone. This implies that the doppler shift of the wake (in Figure 2-4) is virtually stationary with respect to the mean ocean surface and that the phase velocities of the large (greater than twice SAR resolution) waves in the wake are not determining the doppler shift observed by the SAR. Hence for Figure 2-4 we conclude that quasi-specular scattering plays at most a minor role. However, in Figure 2-7 there are very bright linear features in some wakes which appear to end on the ship (rather than being displaced as is often the case). This suggests that these bright features may be scattering via the quasi-specular mechanism, and therefore have a doppler shift comparable to the ship speed.

While large scale surface height fluctuations ($K < K_{sar}$) would be associated with the large scale waves of a Kelvin ship wake (θ not near zero in Figure 2-12); small-scale roughness ($K > K_{emh}$) must be generated either by an ambient wind or by the ship itself (see Figure 2-9). If an ambient wind is involved, then the wake would have small scale structure approximately uniformly distributed over the wake, but subject to modification by large scale roughness via tilting and wave-wave interaction as discussed below. Also, both wake features and the background on which the wake is superimposed are similarly enhanced as wind speed increases.

While wind direction does not seem very important at the L-band frequency of SEASAT it is more so at higher radar frequencies. This comment is based on the known wind direction dependence of ocean radar cross section at varicus frequencies (Jones & Schroeder, 1978).

Small-scale roughness is also associated with the Kelvin wake itself for regions close to the velocity axis of the ship. Classical Kelvin wake theory predicts small scale roughness for small θ (see Figure 2-12) in that the waves near the ship velocity axis must travel slowly, and therefore via their dispersion relation have small wavelengths. Dashen et al. (1982) discuss this phenomena. In addition small scale roughness may be generated by wave breaking and other processes which occur when a real ship of finite size generates a wake. For example generation of small waves by a real ship probably occurs non-uniformly (in both space and time) over the length of the ship (and possibly behind it).

Finally, the quasi-specular process being related to large scale roughness does not require generation of small scale waves as does the Bragg mechanism. Hence for large scale ($\gtrsim 20\lambda$) waves generated in a ship's Kelvin wake quasi-specular backscatter can occur whether or not a wind is blowing.

2.5.2.3 Tilt Mechanism. SEASAT SAR observed the ocean at an angle of incidence $\theta \sim 23^0$ with horizontal polarization. These parameters are particularly well suited to distinguishing resolution cell sized patches tilted at different angles relative to the radar line of sight. The tilts here refer to the tilting introduced by the waves of the Kelvin wake. Figure 2-13 shows calculations by Bahar et al. (1983c) of fractional changes in radar cross section $d\sigma/\langle\sigma\rangle$ with respect to tilts in $(d\Omega)$ and perpendicular to $(d\tau)$ the plane of incidence. Although these curves are for K-band (λ = 3 cm), not L-band (λ = 23 cm) as used by SEASAT SAR, and use a particular sea surface model (see Bahar et al., 1983c, p. 626), we can note general features using a similar calculation by Vesecky et al. (1983) at L-band for reference. First, tilting in the plane of incidence (with respect to Ω) is much more effective in modulating $\langle \sigma^{HH} \rangle$ than is tilting perpendicular to the plane of incidence (with respect to τ). Thus so far as tilting induced by waves in the Kelvin wake is concerned, waves in the divergent portion of the wake should be more prominent when the ship is traveling nearly along the azimuth direction (ϕ near 0 or 180^0 in Figure 2-12). Waves in the transverse portion of the wake should be more visible when the ship is traveling near the range direction (ϕ near 90^0 or 270^0 in Figure 2-12). Referring to Section 2.5.2.3 above, we see from Figure 2-4 that indeed the transverse waves are

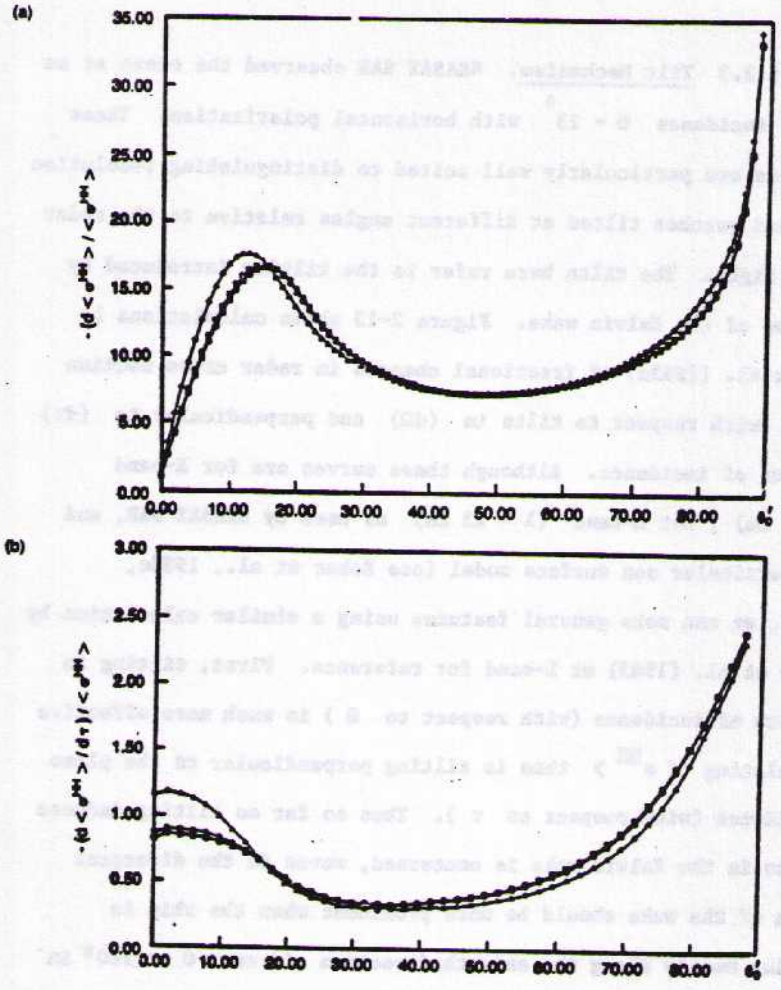

Figure 2-13. Rate of fractional change of radar backscatter cross section (horizontal transmit and receive polarization) with respect to tilts of the resolution cell (a) in the plane of incidence ($d < \sigma^{HH} > / d\Omega) / < \sigma^{HH} >$ and (b) perpendicular to the plane of incidence ($d < \sigma^{HH} > / d\tau) / < \sigma^{HH} >$). Triangles, octagons and squares refer to resolution cell sizes of 3 m, 10 m and 25 m (SEASAT), respectively. θ'_o is the angle of incidence in the absence of any tilt. Radar wavelength is λ = 3 cm (X-band). After Bahar et al. (1983c).

more prominent in this case when $\phi = -112^0$. Further the transverse waves in the upper portion (above the dark turbulent wake) of Figure 2-4 are more visible than in the lower portion of the wake. And indeed ϕ is closer to 90° in the upper portion of the wake. As a crude estimate of the expected peak to trough cross section variation for the transverse wake waves in Figure 2-4, we let the transverse waves be sinusoidal with a wavelength $\Lambda = 94$ m (see Section 2.5.2.3 above) and amplitude $A = 0.5$ m (1 m peak to trough). The slope thus varies by $\pm \Delta K = \pm 0.034$ radians $= \pm 1.9°$ around $\theta_o' = 23.8^0$, the mean angle of incidence for this image. Referring to Figure 2-13(a) $[(d \langle \sigma^{HH} \rangle / d\Omega) / \langle \sigma^{HH} \rangle] = 12$ and $\delta \langle \sigma^{HH} \rangle = \pm \Delta K [(d\langle \sigma^{HH} \rangle / d\Omega) / \langle \sigma^{HH} \rangle] = \pm (0.5)(2\pi/93)(12) = \pm 0.4$ which implies a maximum to minimum cross section variation of ~ 2.5 dB. One would have to do a quantitative calculation using the digital version of Figure 2-4 to check this figure, but qualitatively the expected and observed cross section variations are small.

Another implication of Figure 2-13 is that since the angle of incidence for SEASAT was $\theta_o' \sim 23^0$, SEASAT operated near the combination of maximum mean $\langle \sigma^{HH} \rangle$ (see Figure 2-8) and maximum sensitivity of $\delta \langle \sigma^{HH} \rangle$ to changes in surface slope. Note that Figure 2-13 refers to a tilted resolution cell; hence we have implicitly assumed that any wave slopes referred to are for waves

with wavelength at least two resolution cells in size, i.e., $\lambda > 50$ m for SEASAT.

In some cases, e.g., Figure 2-4, a wake feature associated with the line of cusps at $\theta = \pm 19.5^0$ in Figure 2-12 can be identified. The wave shape for a Kelvin wake is unique along the cusp line in that first, the wave height is generally largest there and second, the wave decays in nearly every direction away from the crest. In terms of the tilt mechanism one would expect enhanced radar backscatter if the radius of curvature of the "boss" shaped features at the cusp were large enough (much larger than a resolution cell size) and properly oriented. Otherwise, one could expect reduced radar cross section since the boss would either have only small portion tilted more nearly (than the mean surface) toward the radar and the rest tilted less nearly toward the radar. This second case appears to obtain in Figure 2-4, since the cusp line is dark in the SAR image. However, there are in other cases bright cusp lines, e.g., Figure 22 of Shuchman et al. (1983) where the X-band aircraft SAR resolution cell is much smaller than SEASAT's 25 m.

In the above discussion we have not included the ambient ocean waves which may be present and of higher amplitude than waves in Kelvin wakes. In general, a spectrum of ambient ocean waves large

compared to the Kelvin wake should tend to obscure the Kelvin wake since they increase the mean ocean radar cross section, and hence this cross section's variance from one resolution cell to the next--cross section variance is approximately equal to the mean for one-look SAR processing.

2.5.2.4 Hydrodynamic Wave-Wave Interaction. Both experimental and theoretical studies indicate that hydrodynamic wave-wave interaction causes short waves (wavelengths $\sim \Lambda_b$) riding on longer waves to be strained by the long waves such that the amplitude of the short waves is enhanced somewhat in advance of the long wave crest at the position where a surfer would ride. For waves traveling toward the radar this position coincides approximately with the portion of the long wave tilted toward the radar $\hat{K}$ vector. Hence, the tilt and hydrodynamic mechanisms would both enhance the radar cross section at nearly the same portion of the long wave for waves traveling toward the radar. However, for waves traveling away from the radar the two effects would tend to cancel. Overall one would expect to find wake waves traveling toward the radar to be more prominent in SAR images than waves traveling away, provided the tilt and hydrodynamic mechanisms are about equally effective in modulating the radar cross section wake waves. Because of this effect one would usually expect one arm of a wave image to

be more prominent than the other. There are many examples of wakes with only one arm visible in the SAR image. However, there are images in which two (or more) arms of a V-shaped wake are visible, e.g., Figures 2-4, 2-5 and 2-6. Shuchman et al. (1983, p. 33) find that, "Usually, one side of the Kelvin wake envelope was more visible than the other side."

2.5.2.5. Surface Motion Doppler Effects--Velocity Bunching and Resolution Smearing. Motion of certain local portions of the ocean surface with respect to the motion of the large scale mean surface produces two major effects. First, if the motion in a resolution cell sized patch of surface is largely coherent, i.e., there is a dominant velocity in terms of both space and time on scales comparable to the SAR resolution cell size and the SAR integration time, then the radar echo energy associated with this dominant velocity will be doppler shifted differently than the mean large scale surface and the echo energy will be shifted along the azimuth direction to an incorrect location. The ship in Figure 2-4 illustrates this point well. Second, if the motion in a resolution cell sized patch is spread over a range of velocities, i.e., there is no strong dominant velocity and a range of velocities exists over the aforementioned spatial and temporal scales, then the radar echo energy is spread in the azimuth direction over a number of SAR

resolution cells. This smearing makes long ocean waves traveling nearly along the azimuth direction difficult to image (viz. Beal et al., 1983 and Vesecky et al., 1984).

As Alpers and Rufenach (1979) and Alpers et al. (1981) have pointed out coherent and systematic spatial patterns of surface motion can cause ocean surface phenomena to be imaged by a SAR (see Section 2.4.2). For example, the periodic variations of surface motion related to long ocean waves. This mechanism is most effective for gravity waves traveling near the azimuth direction (y'- direction in Figures 2-2 and 2-12) and is least effective for gravity waves traveling in the range direction (x'- direction in Figures 2-2 and 2-12). In connection with natural ocean gravity waves there has been considerable controversy over the effectiveness of the velocity bunching mechanism. Both Harger (1984) and Jain (1981) argue that for natural ocean gravity waves no velocity bunching modulation should occur.

As analyzed by Alpers et al., velocity bunching is in general a nonlinear process. The parameter which governs the nonlinearity is C where the change from linear to nonlinear behavior occurs for $C \gtrsim 0.3$ where

$$C = (R/V)\ \Omega A\ (\sin^2\theta'\ \sin^2\phi + \cos^2\theta')^{1/2}\ \cos\phi \qquad (2\text{-}14)$$

and R is range to target, V is SAR platform velocity, A and Ω are wave amplitude and frequency and θ' and ϕ are given in Figure 2-2. Since R/V is relatively large for SEASAT, namely 128, one expects nonlinear behavior to set in for rather small values of wave amplitude. Thus for ship wakes where wave amplitude may be low, but Ω is relatively high nonlinear behavior is very likely.

Since velocity bunching relies on spatial modulation of surface velocity which is on a scale larger than the SAR resolution cell, resolution cells which contain more than one wavelength of the waves making up the Kelvin wake at a given location can not show much velocity bunching modulation (from one resolution cell to the next). That is, resolution cell sizes greater than the spatial scale of orbital velocity variations effectively average out any velocity bunching modulation present. We discuss how this translates into wake effects in Section 2.5.2.6 below.

An effect related to the resolution cell averaging above is degradation of azimuth resolution by surface velocity variations within a resolution cell. These velocity variations effectively smear out (along the azimuth direction). The backscattered energy

which should be associated with a single resolution over two or more resolution cells. Since any resolution cell sized patch of ocean surface contains a statistical distribution of ambient ocean waves in addition to any wake related waves a statistical distribution of surface velocities will be present to degrade azimuth resolution. Similarly Beal et al. (1983) model this effect as a gausian-shaped impulse response function

$$h_v(y) = \exp\left(-y^2/2\,\Sigma_{yv}^2\right) \qquad (2\text{-}15)$$

where $\Sigma_{yv} = (R/V)\,\Sigma_v$ and Σ_v^2 is the variance of the radial (with respect to the radar) velocity distribution averaged over a SAR resolution cell. Similarly if there is acceleration in a coherent (over the resolution cell) surface motion, degradation of resolution along the azimuth direction results. Alpers et al. (1981) give this degradation in azimuth resolution as a function of undegraded resolution, SAR integration time, number of looks, long wave amplitude and frequency and other observational parameters such as (R/V). Beal et al. (1983) and Alpers et al. (1981) give different expressions combining both effects. The principal point here is that resolution cell degradation can effectively average out any velocity bunching (or other) modulation mechanisms by enlarging the resolution cell to a size where waves traveling along the azimuth direction can not be

resolved, i.e., the Nyquist sampling criterion cannot be satisfied. Clearly waves observed on a calm day [low Σ^2_{yv} in equation (2-15)] would be most likely to be imaged via the velocity bunching mechanism. Indeed ship wakes are more frequently imaged on calmer days. However, ship wakes are more frequently imaged when the wake waves are traveling near the range direction where the velocity bunching mechanism is weakest.

2.5.2.6 Effects of Finite Resolution Cell Size. Although one usually thinks of SAR as creating a map of the surface distribution of radar cross section, the process of making the map, i.e., achieving high spatial resolution, actually alters the cross section observed. Further the finite resolution of a SAR causes variations in radar cross section on scales smaller than the resolution cell size to be averaged.

With regard to changes in cross section we refer to material in Section 2.4 and to Figure 2-9. We note that in averaging Bragg resonant scattering over the intermediate scale wavelengths the resulting cross section is determined by an integral in which K_{sar} is the lower limit. Clearly then this integral is dependent on its lower limit and thus on resolution cell size. Work by Vesecky et al. (1983) illustrates these points.

Most of the discussion above concerns expected radar cross section variations from one portion (crest, trough, etc.) to another of a surface gravity wave. Obviously, it is of interest to know how many wavelengths of Kelvin wake waves there are in a SAR resolution cell for different locations in a Kelvin wake. Because if there is more than about one wavelength within a SAR resolution cell the variations between different portions of wave will be averaged out and little variations (from the mechanisms discussed above) from one resolution cell to the next. This does not mean that difference between one resolution cell and the next might not occur because of changes in wave or observational parameters from one resolution cell to the next--we discuss this notion below. In Figure 2-14, we display computations of the number of wavelengths (of the local Kelvin wake waves) per SAR resolution cell. The Kelvin wake wavelengths are computed using the formulas given by Dashen et al. (1982). The important parameters are angle θ in Figure 2-12, ship speed U and SAR resolution. We consider only the divergent waves in the wake since most of the ship wakes of interest (narrow Vees as in Figure 2-5) apparently involve the divergent waves rather than the transverse ones. It is interesting to note that the angle θ at which SAR resolution equals Kelvin wake wavelength decreases with increasing ship speed from about 17° for U_{ship} = 10 m/s to about 12° at 15 m/s to 9° at 20 m/s. There is a suggestion that narrower

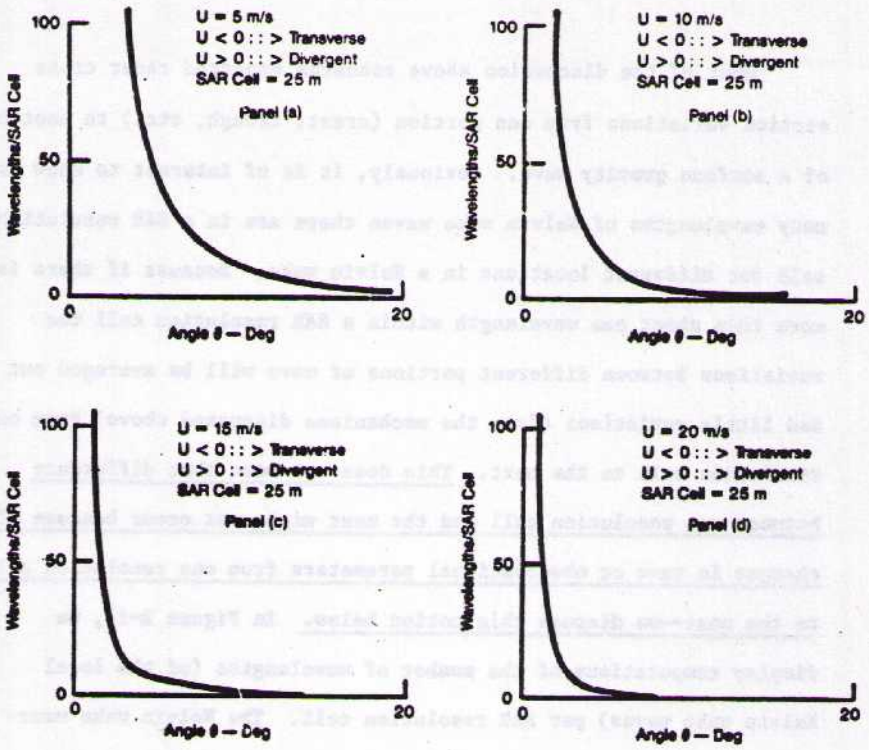

Figure 2-14. Number of wavelengths of the local Kelvin wake surface waves per SAR resolution cell. Panels (a) through (d) correspond to ship speeds of 5 to 20 m/s. The angle θ is measured relative to the ship's velocity axis with the vertex on the ship.

wites in terms of θ are associated with faster ships, for example, Figure 2-5 is thought to be a fast bulk carrier while Figure 2-6 is thought to be a fleet of relatively slow fishing ships. Nevertheless, from these calculations one would not expect to see individual wake waves imaged for θ less than 9° and there are clearly wake images associated with $\theta \sim 3^0$ or 4^0 .

2.5.2.7 An Hypothesis for SAR Imaging of Kelvin Wake Waves for $\theta \geq 10^0$. To explain the fine linear features in ship wakes illustrated in Section 2.3 one must find mechanisms to enhance the radar return at one or more singular values of θ. The hypothesis described here makes use of the tilt, hydrodynamic and velocity bunching mechanisms which are thought to make natural ocean surface waves visible in SAR images. As we have just argued in Section 2.5.2.6 above, this hypothesis can not apply to the region of the wake where $\theta \leq 10^0$ because the wavelengths of the Kelvin wake waves are too small, i.e., smaller than a SEASAT resolution cell. This hypothesis argues that for a given wake and observation situation a particular wavenumber (K^*) in the Kelvin wake will cause a constructive combination of one or more of the above mechanisms. This particular wavenumber corresponds to a particular $\theta = \theta^*$ and hence to a bright line in the wake's SAR image. At wavenumbers near but not at K^* the tilt, hydrodynamic and velocity bunching

mechanisms do not operate "in phase" and hence appear much like the ocean clutter background. The constructive combination occurs over only a small range of θ because ocean wavenumber in the wake changes rapidly with θ. The constructive combination occurs at different values of θ for different cases because the wake itself as well as observational parameters change, e.g., aspect angle ϕ and incidence angle θ'. Figure 2-15 illustrates that the strength of the tilt mechanism is a strong function of angle of incidence θ' especially near the SEASAT observational angles of incidence $\theta' \approx 19^0$-25^0 .

Some wakes, such as Figures 2-6 and 2-7, may be explained by this hypothesis. Even some wakes having bright lines meeting at narrow angles may be explained by arguing that there are two singular values of θ^*, namely θ_1^*, and θ_2^* on the same side of the ship velocity vector and greater than $\sim 10^0$. This could produce two bright linear features meeting at a small angle ($\sim 6^0$). The wake at upper left of Figure 2-7 appears to correspond to this situation.

Very bright linear features could be produced by the tilt mechanism if the tilts were large enough to cause a significant specular or quasi-specular echo. Except for short wavelength waves

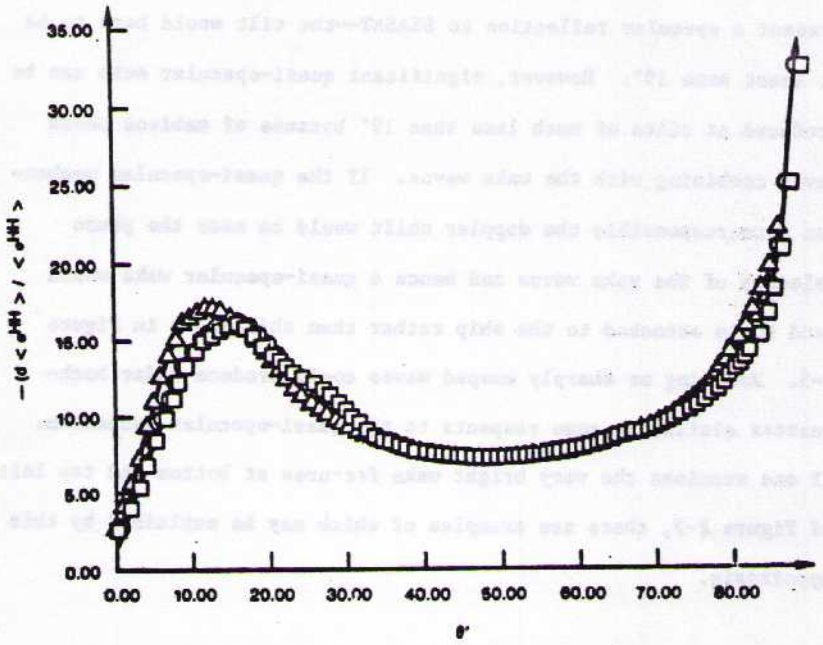

Figure 2-15. Fractional variation of radar cross section with tilt in the plane of incidence — $(d < \sigma^{HH} > / d\Omega) / < \sigma^{HH} >$ for different angles of incidence θ'. The triangles, circles and squares refer to SAR resolution cells 3 m, 10 m and 25 m in size respectively. The radar frequency is X-band, λ = 3 cm. After Bahar et al. (1983c).

(Section 2.5.2.8) it is unlikely that the tilt of a wake wave would present a specular reflection to SEASAT--the tilt would have to be at least some 19°. However, significant quasi-specular echo can be produced at tilts of much less than 19° because of ambient ocean waves combining with the wake waves. If the quasi-specular mechanism were responsible the doppler shift would be near the phase velocity of the wake waves and hence a quasi-specular wake would tend to be attached to the ship rather than shifted as in Figure 2-5. Breaking or sharply cusped waves could produce radar backscatter similar in some respects to the quasi-specular mechanism. If one examines the very bright wake features at bottom and top left of Figure 2-7, there are examples of which may be explained by this hypothesis.

Since the wake waves discussed here are of lengths greater than 25 m, they can persist for long enough times that a long wake feature is possible. At 25 m the period is 4 s and a ship at 10 m/s goes 40 m in 4 s. If the wave persists for several hundred periods corresponding to several e-folding decay times, a wake feature dependent on these waves could be several times 4 km long. Small Bragg waves needed for Bragg resonance scatter would be generated continuously by the wind.

This hypothesis is presently only a sketchy notion. It needs further development using empirical and theoretical models of ship wakes. At present the scattering theory and SAR imaging mechanism theory is enough in hand to make appropriate calculations given a wake model.

2.5.2.8 Narrow Wakes at $\theta \lesssim 10^0$. For Kelvin wakes at $\theta \lesssim 10^0$ the waves involved are smaller than the SAR resolution cell size. To explain wake features here one must rely on changes in scattering properties (of the sea surface) which are averaged over one or more wavelengths of the wake waves at a given θ. Hence, the wave imaging mechanisms discussed above are not directly relevant--crests and troughs lie in the same resolution cell. What is required here is a local (in terms of θ) enhancement of the radar cross section averaged over the numerous wake waves in a SAR resolution cell. For the first order Bragg mechanism this requires an enhancement of wake waves at $\lambda = \lambda_b$ and propagating along the radar range direction. And indeed the simple Kelvin wake model provides this local enhancement since surface gravity waves are dispersive. Waves at longer wavelengths (and in directions other than along the radar range direction) might be involved if higher order Bragg scattering were involved (see Johnstone, 1975 for reference). For the quasi-specular mechanism a statistical ensemble

of wave slopes with a high variance is needed so that a significant number of specular points will appear in a resolution cell. The short wavelength of the wake waves in this region ($\theta \lesssim 10^0$) contributes to a relatively high slope variance for a given wave-height. However, the short wavelength decreases the local radius of curvature and hence lowers the radar cross section (see eq. 2-4). Whether these two contending effects raise or lower $\langle \sigma^{HH} \rangle$ depends on the details of the wake in this region.

In order to make a first order estimate of the radar cross section (using eqs. 2-3 and 2-4) in this portion of a Kelvin wake one needs to know the basic observational parameters, the directional waveheight spectrum at $K = K_b$ along the range direction, and the total waveslope variance--all as functions of θ. To make a better estimate the complete directional waveheight spectrum from K_{sar} upwards to K_b should be known. Breaking waves <u>if they exist in sufficient quantity</u> could be important for narrow wakes. Recall that if there is sufficient random surface motion in a resolution cell the azimuth resolution of the SAR will be degraded and a smearing of the image along the azimuth direction will occur. Since most narrow wakes are linear features along the azimuth direction, this smearing would tend to accentuate features along this direction. Azimuthal smearing would be enhanced if the scattering

features were exhibited doppler shifts associated with wave phase velocities rather than wave orbital velocities. Breaking waves would tend to travel at wave phase velocities and hence would be smeared in azimuth. Evidence of this phenomena is given by Shuchman et al. (1984). Whether one might expect enhanced wave breaking in the interior portions of a Kelvin wake is at present an open question.

Relevant wake hydrodynamics are discussed elsewhere in this report. Several factors which may be important in the $\sigma \lesssim 10^{\circ}$ region are mentioned below. The turbulent wake smoothes the water and reduces $< \sigma >$ for very small values of θ. Short wavelength waves at $1^{\circ} \lesssim \sigma \lesssim 10^{\circ}$ could be generated by mechanisms other than the idealized Kelvin wake point source; for example, by breaking waves along the side of the ship, by interaction of turbulent wake related currents with ambient internal waves and or existing short wavelength waves, and by wave-wave interaction between the short waves of the divergent wake and the relatively long waves of the transverse wake. The lifetime of Bragg resonant waves can be short relative to the length of the observed wakes (~ 10 km).

2.5.3 Effects Associated with Internal Waves

Although the hydrodynamics of surface wave and internal wave wakes are obviously very different (see other sections of this report), there are many scattering and radar effects which are analogous with those discussed above in connection with surface wave wakes.

2.5.3.1 Relevant Scattering Mechanisms. The scattering mechanisms involved in internal wave wakes are the same as those discussed in Section 2.4.1 above. One relevant difference which we discuss below is that internal waves do not tilt the surface. Hence quasi-specular scattering should play a smaller role than in connection with surface wave wakes.

2.5.3.2 Mechanisms for Spatial Modulation of Radar Cross Section. There are several means by which internal wave surface currents may influence radar cross section, namely:

a. Modulation of local waveheight and slope (including breaking waves) by wave-current interaction.

b. Current-induced concentration of surfactants which damp existing waves.

c. Current-induced concentration of surface debris.

d. Velocity bunching due to surface currents.

Each of these items is discussed briefly below. It is important to note that any of these mechanisms might conceivably dominate under some circumstances. Item (a) is the mechanism most often discussed in connection with internal wave wakes. However, surfactants can strongly influence ripples which are involved in Bragg scattering and surface currents imply velocity bunching (see Section 2.5.2.5).

Increased wave height and slope. As discussed in Section 2.4.3 above, surface currents can spatially modulate the ripples and longer waves involved in both Bragg and quasi-specular scattering. If an internal wave packet could sufficiently enhance existing surface waves at current convergence zones, then clearly the internal wave wake would be imaged. The degree of enhancement depends on the induced currents and the wave current interaction discussed briefly in Section 2.4.3 and at length in Section 3.0 below. Two points of interest here are that some of the other

mechanisms discussed immediately below may be involved and that a source term may need to be involved in calculating the wave-current interaction (see Section 2.4.3).

Radar wave scattering from breaking waves is not well understood. However, as discussed in Section 2.5.2.8 above, breaking waves do scatter strongly and the SAR image is smeared along the azimuth direction. If the internal wave current convergence were strong enough, an increase in the area density of breaking waves would presumably occur. The increased density of strongly scattering breaking waves would be particularly evident for a current convergence zone oriented nearly along the azimuth direction because of the concurrent azimuthal smearing.

Concentration of Surfactants. Current convergence zones associated with internal waves would presumably concentrate surfactants as well as concentrating the spectral density of existing ripples. Clearly these two effects would tend to counteract each other if they were "in phase," i.e., active at the same location of the internal wave as one expects they should be. Work by Huhnerfuss (1983) shows that surfactants do indeed show up as dark patches on SAR images. Further there is some evidence that in the tropical Atlantic ocean surfactants of natural origin are almost

always present (Huhnerfuss, et al., 1977). Work by Bagg (1983) indicates that there is no pronounced latitudinal dependence (from 40°N to 66°N) in the frequency of observation of internal waves by SEASAT SAR.

Concentration of Surface Debris. In some waters particularly along coasts there is a significant amount of surface debris. For example debris, such as foam, flotsam and natural floating matter, collect along the boundaries of the Gulf Stream. If such matters were concentrated by internal waves in a ship wake if could conceivably cause enhanced backscatter. At this point such a mechanism is speculative.

Velocity Bunching. Since surface currents associated with internal waves impart a Doppler shift to a radar echo, the different portions of the surface corresponding to the varying phase of an internal wave will have their backscattered energy misplaced in the SAR image as discussed in Section 2.5.2.5. If the velocity varies significantly over a resolution cell, the image will be smeared along the azimuth direction. For SEASAT SAR a surface current velocity of u_x m/s directed in the radar wave plane of incidence (along x' in Fig. 2-1) is sufficient to shift backscattered energy by Δx where

$$\Delta x = U_x \, (R/V) \sin \theta' \qquad (2\text{-}16)$$

and for SEASAT SAR

$$\Delta x = 50 \, u_x .$$

Hence a surface current along x of 50 cm/s is sufficient to shift backscattered energy by a resolution cell size (25 m). It has been suggested that wake-related internal waves could have surface current velocities comparable to 50 cm/s. The phase velocity of Bragg scattering waves is ~ 30 cm/s and is also seen as a Doppler shift, and hence a position shift by the SAR. The two effects are additive; but whereas the Bragg phase velocity would be homogeneous over a large number of resolution cells, the surface current would vary substantially over several resolution cells for a ~ few hundred meter wavelength internal wave associated with a ship.

Combination Effects. Above there are listed several internal wave effects which could spatially modulate the radar cross section mapped into a SAR image. Depending on the nature of the surface current field associated with the internal wave wake, the ocean surface conditions and observational geometry the relative strength and phase of these effects could enhance or degrade the backscatter

cross section making a wake pattern visible or undetectable in the SAR image speckle background. An important point here is that consideration of the combination of effects could produce a result significantly different (in terms of visibility) from the consideration of one effect alone.

Background. The visibility of internal wave effects in SAR images clearly depends strongly on the background upon which the wake is imposed. Some notion of the background issue can be obtained from the work of Bagg (1983). The average ocean backscatter strength increases with wind speed for SEASAT angles of incidence. Bagg noticed in studying 128 observations of natural internal waves by SEASAT that over 2/3 of the observations were in winds of 10 kts or less while only 1/10 of the observations were in wind speeds of 20 kts or more. Thus, as the mean background backscatter level was raised by increased wind speed the number of internal waves observed decreased dramatically. Similarly SAR image features associated with wake related internal waves should become less detectable as wind speed increases.

2.6 Conclusion and Recommendations Associated with Radar Effects

2.6.1 Conclusions

All important radar scattering and SAR system effects must be combined with analytical (or emperical) models of the surface morphology and currents in a wake to order to obtain an accurate estimate of what a SAR would image.

Purturbations of ocean surface roughness and currents by Kelvin wakes can produce different images when viewed by a SAR under different observational and environmental conditions. This is also true for internal wave wakes.

Photographs corresponding to SAR images of ship wakes may produce a distorted idea of ship wake features because contrast stretching is used to obtain a "interesting" photograph.

First order Bragg resonant scattering has almost always been assumed to cause ocean surface backscatter observed by SAR. It now appears that quasi-specular and perhaps higher order Bragg resonant scatter or mechanisms related to breaking waves may also be important.

2.6.2 Recommendations

SAR image data on ship wakes should be examined in digital form using an image processing system because photographic prints can be misleading if they are contrast stretched. Some issues of interest regarding ship wake images are: line width of wake features, multiple or striated wakes, smearing of wake features along the azimuth direction and length of wake features.

It would be useful to do a comprehensive computation of the SAR image produced by even a crude model of wake surface roughness and currents. This idea would be to get a feel for how a SAR interprets the surface morphology and currents expects from Kelvin and internal wave wakes.

Data on natural internal waves gathered both by SAR and by in situ measurements should be examined to better understand SAR images of internal waves. In particular is a relaxation time approach to the modulation of ocean surface roughness viable - what is the relaxation time?

Further research is needed to discover the role of quasi-specular, higher-order Bragg resonant backscatter and other mechanisms in SAR imaging of the ocean surface.

REFERENCES FOR SECTION 2.0

1. Alpers, W.R., private communication (1984).

2. Alpers, W.R. and K. Hasselmann, The Two-Frequency Microwave Technique for Measuring Ocean Wave Spectra from an Airplane or Satellite, Appendix B, Boundary-Layer Meteorl., 13, 215-230 (1978).

3. Alpers, W.R., D.B. Ross and C.L. Rufenach, On the Detectability of Ocean Surface Waves by Real and Synthetic Aperture Radar, J. Geophys. Res., 86, 6481-6498 (1981).

4. Alpers, W.R. and C.L. Rufenach, The Effect of Orbital Motions on Synthetic Aperture Imagery of Ocean Waves, IEEE Trans. Antenna & Propagat., AP-27, 685-690 (1979).

5. Bahar, E. & D.E. Barrick, Scattering Cross Sections for Composite Surfaces that cannot be Treated as Perturbed-Physical Optics Problems, Radio Science, 18, 129-137 (1983a).

6. Bahar, E., D.E. Barrick and M. A. Fitzwater, Computations of Scattering Cross Sections for Composite Surface and the Specification of the Wavenumber Where Spectral Splitting Occurs, IEEE Trans. Antennas & Propagat. AP-31, 698-709 (1983b).

7. Bahar, E., C.L. Rufenach, D.E. Barrick, and M.A. Fitzwater, Scattering Cross Section Modulation for Arbitrarily Oriented Composite Rough Surfaces: Full Wave Approach, Radio Sci., 18, 675-690 (1983c).

8. Bass, F. G. and I. M. Fuks, Wave Scattering from Statistically Rough Surfaces, Pergamon, Oxford (1979).

9 Beal, R. C., The value of spaceborne SAR in the study of wind wave spectra, unpublished manuscript, Johns Hopkins Applied Physics Laboratory, Laurel, MD 20707 (1982).

10. Beal, R. C., P. deLeonibus and I. Katz (eds.), Spaceborne Synthetic Aperture Radar for Oceanography, Johns Hopkins Press, Baltimore, MD (1981).

11. Beal, R.C., D.G. Tilley, and F.M. Monaldo, Large- and Small-Scale Spatial Evolution of Digitally Processed Ocean Wave Spectra from SEASAT Synthetic Aperture Radar, J. Geophy. Res., 88, 1761-1778 (1983).

12. Bennet, J. R. and I. G. Cumming, Digital SAR image formation: Airborne and satellite results, in Proceedings of the 13th International Symposium on Remote Sensing of the Environment, University of Michigan, Ann Arbor, MI (1979).

13. Fu, L. L., and B. Holt, "SEASAT Views Oceans and Sea Ice with Synthetic-Aperture Radar," JPL Publication 81-120, Jet Propulsion Laboratory, Pasadena, CA (1982).

14. Gargett, A. E. and B. A. Hughes, On the interaction of surface & internal waves, J. Fluid Mech., 52, 179-192 (1981).

15. Harger, R.O., The SAR Imaging of Short Gravity Waves on a Long Gravity Wave, in Proceedings of the IUCRM Symposium on Wave Dynamics and Radio Probing of the Ocean, (O.M. Phillips, ed.), Plenum Press, N.Y., in press (1984).

16. Hasselmann, K., R. K. Raney, W. J. Plant, W. R. Alpers, R. A. Shuckman, D. R. Lyzenga, C. L. Rufenach & M. J. Tucker, Theory of SAR ocean wave imaging: A MARSEN view, J. Geophys. Res., (submitted manuscript, 1984).

17. Huhnerfuss, H. W. Alpers, A. Cross, W.O. Garrett, W.C. Keller, P.A. Lange, W.J. Plant, F. Schlude and D.L. Schuler, J. Geophys. Res., 86, 9817-9822 (1983).

18. Huhnerfuss, H., W. R. Alpers, P. A. Lange and W. Walter, Attenuation of wind waves by artificial surface films of different chemical structure, Geophys. Res. Letters., 8, 1184-86 (1981).

19. Huhnerfuss, H., W. Walter and G. Kruspe, On the variability of surface tension with mean wind speed, J. Phys. Ocean., 7, 567-571 (1977).

20. Jain, A., SAR Imaging of Ocean Waves: Theory, IEEE J. Ocean Eng., OE-6, 130-139, (1981).

31. Vesecky, J.F., R.H. Stewart, R.A. Shuchman, H.M. Assal, E.R. Kasischke, and J.D. Lyden, On the Ability of Synthetic Aperture Radar to Measure Ocean Waves, Proceedings of the IUCRM Symposium on Wave Dynamics & Radio Probing of the Ocean Surface, O.M. Phillips, ed., Plenum, N.Y. in press (1984).

32. Vesecky, J. F., and R. H. Stewart, "The observation of ocean surface phenomena using imagery from the SEASAT synthetic aperture radar: an assessment," J. Geophys. Res., 87, 3397-3430 (1982).

33. Wright, J.W., Detection of Ocean Waves by Microwave Radar; the Short Gravity-Capillary Waves, Boundary-Layer Meteorl., 13, 101-112 (1978).

34. Zachariasen, F., The effects of surface currents on the equilibrium surface-wave spectral energy density, Tech. Rpt. TSR-73-2, Stanford Research Inst., Menlo Park, CA 94025 (1973).

35. Valenzuela, G.R., Theories for the interaction of electromagnetic and ocean waves - A review, Boundary Layer Meteorol., 13, 61-85 (1978).

36. Kodis, R., A note on the scattering from an irregular surface, IEEE Trans. Antennas Propagat., AP-14, 77-82 (1966).

37. Barrick, D.E., Rough surface scattering based on the specular point theory, IEEE Trans. Antennas Propagat., AP-16, 449 (1968).

38. Hughes, B.A., The effect of internal waves on surface wind waves; Part 2, theoretical analysis, J. Geophys., Res., 83, 455-465 (1978).

39. Dashen, R., W. Munk & F. Zachariasen, "Letter to Andreassen & Harper," Report JSN-83-01, MITRE Corp., 1820 Dolley Madison Blvd., McLean, VA (1982).

40. Lighthill, J., Waves in Fluids, Cambridge Univ. Press, Cambridge (1978).

41. Graf, K.A., D.E. Tremain and H. Guthart, Induced current effects on microwave backscatter, IEEE Trans. Antennas Propagat., AP-25, 36-42 (1977).

42. Shuchman, R.A., E.S. Kasischke, D.R. Lyzenga and A. Klooster, "Ship Wake Signatures," ERIM Report 157700-1-X, Environmental Research Inst. of Michigan, Box 8618, Ann Arbor, MI (1983).

43. Scnuchman, R.A., W. Rosenthal, J.D. Lyden, D.R. Lyzenga, E.S. Kasischke, H. Gunther and H. Linne, Analysis of MARSEN X-band SAR Ocean Wave Data, J. Geophys. Res., 88, 9757-9768 (1984).

44. Huhnerfuss J., W. Walter and G. Kruepe, On the variability of surface tension with mean wind speed, J. Phys. Ocean., 7, 567-571 (1977).

45. Gotwols, B.L., R.E. Sterner, W.C. Keller and W.J. Plant, Optical and radar measurements of long wave/short wave interactions in a wind wave tank (abstract EOS, 64, 1052, 1983), paper presented at AGU Ocean Sciences Meeting, New Orleans, La., January (1984).

46. Lyden, J.D., D.R. Lyzenga, R.A. Shuchman and W.L. Jones, "Measurement of Ocean Surface Winds by Synthetic Aperture Radar," ERM Report 155900-15-T, Environmental Research Inst. of Michigan, Ann Arbor, MI 48107 (1983).

47. Bagg, M.T. and K.I. Johnson, Internal wave features in the northeast Atlantic as imaged by SEASAT-SAR, paper presented at Remote Sensing Society one day meeting on Active Microwave (SAR) Sensing of Oceans (proceedings available) convened by D.W.S. Lodge at Royal Aircraft Establishment, Farnborough, UK, April 4 (1984).

48. Lyzenga, D.R. and R.A. Shuchman, Analysis of scatterer motion effects in MARSEN x-band imaging, J. Geophys. Res., 88, 9769-9755 (1984).

49. Kasischke, E.S., R.A. Shuchman, J.D. Lyden and Y.C. Tseng, "Analysis of SEASAT SAR Imaging collected during the JASIN Experiment," Report 155900-16-T, Environmental Research Institute of Michigan, Ann Arbor, MI, 48107 (1983).

3.0 INTERNAL WAVE WAKES

3.1 Internal Wave Wakes

Physically, a ship moving on the surface of the sea generates an internal wave wake by disturbing the ambient density profile. The internal waves are thus the oscillations of this profile around its equilibrium value. The disturbance can be produced by several effects, including the potential flow around the ship, and the turbulent wake it leaves behind, among others. For simplicity, we will concentrate here on the first of these; that should be sufficient for a rough estimate, at least, of the surface currents the internal wave wake will produce. As will be discussed in the following section, it is these surface currents which generate the radar return from the internal wave wake.

The vertical displacement $\zeta(\vec{x},z)$ at depth z (z is, of course, positive upwards) and horizontal position $\vec{x}$ satisfies the internal wave equation

$$\left[\frac{\partial^2}{\partial t^2}\left(\frac{\partial^2}{\partial z^2} + \nabla_\perp^2\right) + N^2(z)\nabla_\perp^2\right] \zeta\,(\vec{x},z,t) = S(\vec{x},z,t) \qquad (3\text{-}1)$$

where S is a source and $N^2(z) \equiv -\frac{g}{\rho}\frac{\partial \rho}{\partial z}$ is the buoyancy frequency. We specialize to a moving source $S = S(\vec{x} - \vec{U}t, z)$ (we take $\vec{U}$ in the positive x direction) and look in the rest frame of the source. In this frame S and ζ both become independent of time, and the solution to (3-1) may then be written in the form

$$\zeta(\vec{x},z) = \int \frac{d^2k}{(2\pi)^2} \int dz' e^{i\vec{k}\cdot\vec{x}} \sum_n \frac{\omega_n^2(k) W_n(z,k) W_n(z',k)}{k^2(k_x^2 U^2 - \omega_n^2(k))} S(\vec{k},z') \quad . \tag{3-2}$$

Here $S(\vec{k},z)$ is the horizontal Fourier transform of the source, and W_n and ω_n are the eigenfunctions and eigenvalues of the operator in (3-1), so that

$$[\omega_n^2(k)(\frac{\partial^2}{\partial z^2} - k^2) + k^2 N^2(z)] W_n(z,k) = 0 \tag{3-3}$$

subject to the appropriate boundary conditions that $W_n = 0$ at $z = 0$ and $z = -\infty$.

The integral over k_x can now be evaluated by contour integration, locating the poles at $k_x = \pm \omega_n(k)/U$ in the lower half plane to ensure causality. We note that, for internal waves,

$1/U\left(\partial\omega_n(k)/\partial k_x\right) \ll 1$ and $k_y \gg k_x$; with these simplifications (3-2) becomes

$$\zeta(\vec{x},z) = \theta(-x) \int \frac{dk_y}{2\pi} e^{ik_y y} \int dz'$$

$$\sum_n \frac{\omega_n(k)}{k^2 U} W_n(z,k) W_n(z',k) \sin \frac{\omega_n(k)}{U} x \cdot S(k,z') \qquad (3\text{-}4)$$

where now $k = |k_y|$ to a very good approximation.

Thus ζ is a sum of contributions, one from each internal wave mode. We may write $\zeta = \sum_n \zeta_n$, with ζ_n identified in Eq. (3-4).

In the far field, the integral over k_y in Eq. (3-4) can be evaluated by stationary phase. This yields two wave systems, one traveling in the $+y$ direction, with $k_y = k > 0$ and k determined from the stationary phase condition

$$\tan\theta \equiv y/(-x) = \frac{1}{U} \frac{\partial\omega_n(k)}{\partial k} \qquad (3\text{-}5)$$

and another traveling in the $-y$ direction with $k_y = -k < 0$. Evidently, θ in Eq. (3-3) is the angle off the wake axis. It is sufficient to fix our attention on only one of these, say that in

the $+y$ direction, call it $\zeta_n^{(+)}$. Evaluating the integral over k_y then yields

$$\zeta_n^{(+)}(\vec{x},z) = \frac{\theta(-x)}{\sqrt{-2\pi x}} \sqrt{\frac{1}{-\frac{1}{U}\frac{\partial^2 \omega_n}{\partial k^2}}} \frac{\omega_n(k)}{k^2 U}$$

$$W_n(z,k) \int dz' W_n(z',k) S(k,z') \sin\left(k_y + \frac{\omega_n(k)}{U} x + \pi/4\right) \tag{3-6}$$

where k is determined from Eq. (3-5).

Now let us take as a source the potential flow around the ship hull in an unbounded ocean where the ship is made symmetrical about the plane $z = 0$; call its vertical displacement $\zeta_{POT}(\vec{x},z)$. Then

$$S(\vec{x},z) = - N^2(z) \nabla_\perp^2 \zeta_{POT}(\vec{x},z) \quad ,$$

or

$$S(k,z) = k^2 N^2(z) \zeta_{POT}(k,z) \quad .$$

Let us also specialize to a two fluid model of the thermocline. Then there is only one mode, and we have

$$N^2(z) = g'\delta(z + d)$$

with $g' = g\Delta\rho/\rho$, where $\Delta\rho$ is the density jump at depth $z = -d$. We have, also,

$$\omega(k) = \sqrt{\frac{g'k}{1 + \cosh kd}}$$

and

$$W(z,k) = \begin{cases} -\frac{1}{\sqrt{g}} \frac{\sinh kz}{\sinh kd} , & -d < z < 0 \\ \frac{1}{\sqrt{g}} , & -\infty < z < -d . \end{cases}$$

Thus we get

$$\zeta^{(+)}(\vec{x},z) = \frac{\theta(-x)}{\sqrt{-2\pi x}} \sqrt{\frac{1}{-\frac{1}{U}\frac{\partial^2\omega}{\partial k^2}}} \frac{\omega}{U}$$

$$\zeta_{POT}(k,-d)\sin\left(k_y + \frac{\omega}{U}x + \pi/4\right)$$

$$\times \begin{cases} -\frac{\sinh kz}{\sinh kd} , & -d < z < 0 \\ 1 , & -\infty < z < -d . \end{cases} \qquad (3\text{-}7)$$

Let us simplify further by limiting ourselves to the case $kd \gg 1$. Under these circumstances, Eq. (3-7) simplifies to

$$\zeta^{(+)}(\vec{x},z) = \frac{\theta(-x)}{\sqrt{-2\pi x}} \frac{(g')^{3/2}}{8U^3(\tan\theta)^{5/2}}$$

$$\zeta_{POT}(k,-d)\sin\left(k_y + \frac{\omega}{U}x + \pi/4\right)$$

$$\times \begin{cases} -\dfrac{\sinh kz}{\sinh kd}, & -d < z < 0 \\ 1, & -\infty < z < -d \end{cases} \qquad (3\text{-}8)$$

where

$$k = g'/8U^2\tan^2\theta$$

and

$$\omega = g'/4U\tan\theta \quad .$$

Finally, to obtain a completely explicit answer, let us suppose the ship is spherical. Then

$$\zeta_{POT}(\vec{x},z) = \frac{3}{8\pi} \nabla \frac{z}{(\vec{x}^2 + z^2)^{3/2}} \qquad (3\text{-}9)$$

and hence

$$\zeta_{POT}(k,-d) = \frac{3}{2} V e^{-kd} \qquad (3\text{-}10)$$

where V is the ship volume. As will be made clear in the following section, the quantity relevant for radar backscatter is the surface strain, defined by

$$\epsilon = \frac{\partial \zeta}{\partial z}\bigg|_{z=0} .$$

From Eqs. (3-8) and (3-10), we see that the surface strain is

$$\epsilon = -\theta(-x)\sin\left(k_y + \frac{\omega}{U}x + \pi/4\right)$$

$$\frac{1}{\sqrt{-2\pi x}} \frac{3}{128} \frac{V(g')^{5/2}}{U^5(\tan\theta)^{9/2}} e^{-g'd/8U^2\tan^2\theta} . \qquad (3\text{-}11)$$

As a numerical illustration, suppose we take the following values:

$$V = 10^4 \ m^3$$

$$U = 10 \ m/sec$$

$$g' = 10^{-2} \ m/sec^2$$

$$x = 10^3 \ m$$

$$d = 10^2 \ m$$

$$\theta = 2^\circ = 1/30$$

Then we find the strain amplitude to be

$$\epsilon = 4 \times 10^{-4} \quad .$$

Since our approximation assumed $kd \gg 1$, while with the above parameters kd is only 9/8, this result is probably a slight overestimate. For more accurate values, one should use Eq. (3-7) with the correct value of $\omega(k)$, not assuming $kd \gg 1$.

3.2 Radar Observations of Internal Waves

3.2.1 Abstract

Radar images of weak internal waves are obscured by the speckle associated with any form of coherent illumination. It can only be removed by averaging. A precise method is given for identifying and counting the necessary degrees of freedom.

3.2.2 Introduction

It is well known that large amplitude internal waves can be detected by their effect on surface roughness. The basic hydrodynamic mechanism[1] is straining of the surface by the internal

waves which changes the slopes of small, ambient ripples. The eye then sees a change in the reflected sky brightness. Recently, there has been considerable interest in the use of radar to monitor the sea surface. The radar cross section is a direct measure of surface roughness.

Radar images from SEASAT[2,3] clearly show some internal waves. However, these are believed to be rather special waves that are both long crested and have large amplitudes. It is interesting to ask if a space-based SAR could detect weaker (more typical) internal waves. The problem is speckle. Speckle is a graininess or noise in the image which is always present when a rough surface is illuminated coherently. It can be removed only by incoherent averaging. Low contrast features (e.g., weak internal waves) will be lost in a random pattern of speckle unless enough averaging can be done.

Detection of weak internal waves from a satellite is not a-priori hopeless. Satellites can image large areas of the ocean and considerable averaging is possible. It is a quantitative issue; one has to compute the signal to noise. Simple numerical estimates can be obtained with the following two rules:

(i) The variance in the radar cross-section is equal to its average. This is true independent of the size of the resolution cell.

(ii) An average with N degrees of freedom will reduce the variance of the cross section by a factor of $1/\sqrt{N}$.

Thus an average over N degrees of freedom will yield the (true) average of the cross section to within a fractional error of $1/\sqrt{N}$. Roughly speaking, if an internal wave makes a fractional change ε in the radar cross-section, then an average with ε^{-2} degrees will be required in order to observe it. Very large ambient waves have $\varepsilon \sim .1$; a more typical number is $\varepsilon \sim 10^{-3}$.

The subtle issues arise when one tries to rigorously count the available degrees of freedom. It seems intuitively clear that looking at several pieces of the ocean will produce a better average, but how about looking at the same patch at different angles or (radar) frequencies? The purpose of this report is to give a definitive answer to these questions. The calculations are a bit longer than one would like, but the answer is simple and satisfying. In particular, the way in which the fluctuations depend on the size of a resolution cell is worked out in detail. It turns out that if

one uses all available information, then the size of a cell is irrelevant. However, this is generally not true in practice.

It is simplest to work things out for an ordinary monostatic radar system. The bulk of the text is devoted to this analysis. SEASAT is actually a synthetic aperture radar (SAR). This introduces some further complications, but once the simple monostatic case is understood, it is not hard to make the transition to SARs.

All the calculations are done under the assumption that the Born approximation is valid. The results are actually more general, but the proof will not be given here. In practice, the Born approximation is usually adequate. Also, the problem will be set up in terms of a scalar wave equation. The results apply separately to either vertical or horizontal polarization.

The report is organized as follows. Section 3.2.3 is a summary of the statistical properties of ripples and the way in which they are affected by an internal wave. The information contained in the ripples is computed in Section 3.2.4. Section 3.2.5 discusses simple radar scattering and the transition to a SAR is carried out in Section 3.2.6.

3.2.3 Wave Statistics

Let $h(\underline{r})$ be the height of the ocean surface at the point $\underline{r} = (x,y)$ and let $a(\underline{k})$ be its Fourier transform $h(\underline{r}) = \int d^2k\, a(\underline{k})\, e^{i\underline{k}\cdot\underline{r}}$. It will be assumed that, in the absence of a perturbing internal wave, the $a(\underline{k})$ are independent random variables with a Gaussian distribution. The unperturbed statistics are then specified by the correlation function

$$\langle a(\underline{k})\, a^*(\underline{k}')\rangle = \delta^2 (\underline{k}-\underline{k}')\, F(\underline{k}) \qquad (3\text{-}12)$$

where $F(\underline{k})$ is adequately described (Ref. 1) by

$$F(\underline{k}) = \frac{B}{\pi} k^{-4}, \qquad B = 0.005 \qquad (3\text{-}13)$$

for the wavelengths (tens of centimeters) which will be of interest. Physically, one can think of the ocean surface as a sum of plane waves $a(\underline{k})\, e^{i\underline{k}\cdot\underline{r}}$ whose phases are random and whose amplitudes have the average value $[F(\underline{k})]^{1/2}$.

Now supppose that this random collection of plane waves is allowed to interact with a weak internal wave whose wavelength and period are long compared to those of the relevant ripples. What

will happen is that a plane wave of amplitude $|a|$ and wave number $\underline{k}$ will be converted into a new wave of amplitude $|a'|$ and wave number $\underline{k}'$. The phases remain random. Thus, the effect of an internal wave is to take a distribution of random plane waves and replace it by a different one. For a weak internal wave the changes $\delta\underline{k} = \underline{k}' - \underline{k}$ and $\delta|a| \equiv |a'| - |a|$ will be small. Also for small $|a|$, which is the situation in practice, $\delta\underline{k}$ will be independent of $|a|$ and $\delta|a|$ will be proportional to $|a|$. Thus $\delta\underline{k}$ and $\delta|a|/|a|$, in contrast to $\delta|a|$ itself, are not random variables but are completely determined by $\underline{k}$ and the internal wave. This allows one to write

$$F'(\underline{k}) - F(\underline{k}) \equiv \delta F(\underline{k}) = \frac{2\delta|a(\underline{k})|}{|a(\underline{k})|} F(\underline{k}) - \delta\underline{k} \cdot \frac{\partial}{\partial \underline{k}} F(\underline{k}) \tag{3-14}$$

$$= \left(2 \frac{\delta|a(\underline{k})|}{|a(\underline{k})|} + \frac{4\underline{k} \cdot \delta\underline{k}}{k^2}\right) F(\underline{k}) = 2\gamma(\underline{k})\, F(\underline{k})$$

where F' is the new distribution function, Eq. (3-13) has been used, and the last line defines $\gamma(\underline{k})$. The factor $\gamma(\underline{k})$ is a dimensionless number which can be computed from hydrodynamics. It is a numerical factor of order one times the internal wave strain and is small for weak (linear) internal waves. The precise form of γ will not be needed here.

The total effect of an internal wave is, then, to change the probability distributions of the independent random quantities $a(\underline{k})$. No coherent effects or new correlations are introduced. If the unperturbed a's were Gaussian-distributed, so are the perturbed ones $a + \delta a$. The function $\delta F(\underline{k})$ in Eq. (3-14) therefore contains all available information. It is important to keep this in mind.

3.2.4. Information Contained in the Ripples

The wavelength of interesting internal waves is always much longer than that of the surface ripples. One can take advantage of these quite different scales of length in the following way. Divide the area to be observed into square patches whose linear dimension L is small compared to the internal wavelength. Label these patches by $\alpha = 1, 2, \ldots,$ and let $\underline{R}_\alpha$ be the center of the α-th patch. Next choose some length ℓ which is long compared to the ripple wavelengths of interest but small compared to L . Subdivide each L-by-L patch into $(L/\ell)^2$ smaller squares of linear dimension ℓ . Let $\underline{R}_\alpha + \underline{r}_i$ $(i = 1, 2, \ldots,)$ be the center of the small patches in the α-th large patch and define the Fourier coefficient

$$A_i(\underline{R}_\alpha, \underline{k}_{nm}) = \frac{1}{(2\pi)^2} \int e^{-i\underline{k}_{nm} \cdot \underline{x}} h(\underline{R}_\alpha + \underline{r}_i + \underline{x}) d^2x \quad (3\text{-}15)$$

where $\underline{k}_{nm} = (2\pi n/\ell, 2\pi m/\ell)$ and $n, m = 0, 1, 2, \ldots, .$ The quantity $A_i(\underline{R}_\alpha, \underline{k}_{nm})$ is evidently a local Fourier transform which is capable of resolving wave numbers which differ by more than $2\pi/\ell$. By the definition of ℓ, this is adequate to resolve the ripples of interest. Furthermore, by the definition of L, the statistical properties of $A_i(\underline{R}_\alpha, \underline{k}_{nm})$ must be (nearly) independent of i. In fact, no information is lost if one considers only the average quantity

$$G(\underline{R}_\alpha, \underline{k}_{nm}) \equiv \left(\frac{\ell}{L}\right)^2 \sum_i |A_i(\underline{R}_\alpha, \underline{k}_{nm})|^2 \quad . \quad (3\text{-}16)$$

Any method of observing the ocean surface that determines $G(\underline{R}_\alpha, \underline{k}_{nm})$ provides all the information that is relevant for detecting the internal waves. Any more detailed information about the sea surface is superfluous. The phases of the A_i are purely random and therefore uninteresting. The individual amplitudes $|A_i|^2$ are also uninteresting. Since the internal wave is supposed to change little over a length L, the individual A_i's differ from G only in that they fluctuate more. According to what was said in the last section these fluctuations of A_i^2 around its average are the same in the presence or absence of internal waves.

The average value of G in the absence of an internal wave is

$$\langle G(\underset{\sim}{R}_\alpha, \underset{\sim}{k}_{nm})\rangle = F(\underset{\sim}{k}_{nm}) \quad , \qquad |\underset{\sim}{k}_{nm}| \gg 2\pi/L \tag{3-17}$$

with the stated proviso that $|\underset{\sim}{k}_{nm}|$ is large compared to $2\pi/L$. With a perturbing internal wave, the shift in the average is

$$\frac{\delta\langle G(\underset{\sim}{R}_\alpha, \underset{\sim}{k}_{nm})\rangle}{F(\underset{\sim}{k}_{nm})} = 2\gamma(\underset{\sim}{R}_\alpha, \underset{\sim}{k}_{nm}) \tag{3-18}$$

where γ depends on the patch location $\underset{\sim}{R}_\alpha$.

Having decided what there is to be measured, the next question is signal to noise. For $|\underset{\sim}{k}_{nm}| \gg 2\pi/L$ it can be shown from Eqs. (3-13) and (3-16) that the $G(\underset{\sim}{R}_\alpha, \underset{\sim}{k}_{nm})$ are, to a good approximation, independent Gaussian-distributed random variables satisfying

$$\langle G(\underset{\sim}{R}_\alpha, \underset{\sim}{k}_{nm})G(\underset{\sim}{R}_{\alpha'}, \underset{\sim}{k}_{n'm'})\rangle = \delta_{\alpha\alpha'}\delta_{nn'}\delta_{mm'}[1 + 2(\tfrac{L}{L})^2]F^2(\underset{\sim}{k}_{nm}) \quad ,$$

$$|\underset{\sim}{k}_{nm}| \gg 2\pi/L \quad . \tag{3-19}$$

A reasonable definition of signal-to-noise $\sum$ is then

$$\sum^2 = \sum_{nm\alpha} \frac{L^2}{L^2}\frac{1}{2}\frac{\delta\langle G(\underset{\sim}{R}_\alpha, \underset{\sim}{k}_{nm})\rangle^2}{F(\underset{\sim}{k}_{nm})} = \sum_{nm\alpha} \frac{L^2}{L^2}\gamma(\underset{\sim}{R}_\alpha, \underset{\sim}{k}_{nm}) \quad . \tag{3-20}$$

The quantity $e^{-\Sigma^2}$ has a simple interpretation. It is the probability of "false alarm" when an ideal matched filter is used.

To compute Σ it is convenient to replace the sum $\sum_{nm}$ by the integral $(\ell/2\pi)^2 \int d^2\underline{k}$. Similarly, the sum $\sum_{\alpha}$ can be replaced by $L^{-2} \int dR$ if $\delta\langle G\rangle$ varies slowly with $\underline{R}_\alpha$. The definitions of ℓ and L were just such as to guarantee these conditions. Thus, regarding G as a function of the continuous variables $\underline{R}$ and $\underline{k}$, one has

$$\Sigma = \left(\frac{1}{2}\frac{1}{(2\pi)^2}\int d^2k d^2R \frac{\delta\langle G(\underline{R},\underline{k})\rangle^2}{F(\underline{k})}\right)^{1/2} = \frac{1}{2\pi}\left[\int d^2k d^2R \gamma(\underline{R},\underline{k})\right]^{1/2} . \tag{3-21}$$

Notice that the lengths ℓ and L have cancelled out of the final answer.

All of the above discussion refers to a single observation of the ocean surface. One might make several observations at different times. If the observations are done over a time T, the number of statistically independent looks will be T divided by the relaxation time of ripples t_R. Then by the usual rules of probability, one can define an effective Σ

$$\Sigma_{eff} = \left(\frac{T}{t_R}\right)^{1/2} \Sigma \quad . \tag{3-22}$$

3.2.5 Radar Scattering

For scattering of microwave radar off small ripples, the Born approximation is adequate. If the radar illuminates an area S the scattered power is proportional to

$$P = \left| \int_S e^{i\underline{k} \cdot \underline{x}} h(\underline{x})\, d^2x \right|^2 \tag{3-23}$$

where $\underline{k}$ is the change in the radar propagation vector. Evidently, if the illuminated area S is a square of area ℓ^2 then the scattered power is just $|A_1(\underline{k})|^2$ defined in the previous section. The power averaged over the L^2/ℓ^2 radar resolution cells in a patch is proportional to $G(\underline{R},\underline{k})$. To get the normalization, it is easiest to take the ratios. If σ is the unperturbed radar cross section averaged over a patch and $\delta\sigma$ is the variation due to an internal wave then

$$\frac{\delta\sigma(\underline{R},\underline{K})}{\sigma(\underline{k})} = 2\gamma(\underline{R},\underline{k}) \quad . \tag{3-24}$$

Detailed formulas for γ can now be obtained by comparing with Ref. (2).

Taking the average over a patch assumes, of course, that ℓ is of a reasonable size. What is a reasonable size? Remember that the ratio ℓ/L canceled out of the final expression for signal to noise. In fact, one can easily see that ℓ could have been any length larger than a ripple wavelength and smaller than or equal to L. Thus it appears that the signal to noise is independent of the radar spot size. In a sense it is.

Although the formal expression for $\sum$ is independent of ℓ, one suspects that somehow a price must be paid if ℓ is large. This is indeed true. In Eq. (3-20) for $\sum$ one has to sum over all values of $\underset{\sim}{k}_{nm} = (2\pi n/\ell, 2\pi m/\ell)$ up to the point where $2\pi/|\underset{\sim}{k}_{nm}|$ is smaller than the smallest ripple wavelength of interest λ_{min}. There are roughly $(\ell/\lambda_{min})^2$ terms in the sum. Therefore when ℓ is large, one has to take measurements for many values of $\underset{\sim}{k}$ in order to even approximate the ideal signal-to-noise ratio. This would have to be done either by changing the radar frequency or by looking at the same spot from many different angles.

The above discussion about radar is a good illustration of an interesting general principle. The length ℓ can be thought of as the resolution length of the system in coordinate space. The ideal signal-to-noise ratio is thus obtained only if the resolution in

wave number space is the best possible, namely $2\pi/\ell$. If the resolution in $\underline{k}$-space is changed to $\xi\, 2\pi/\ell$ with $\xi > 1$, then the number of available terms in the sum over n and m in Eq. (3-20) is clearly reduced by a factor of ξ^{-2}, and $\sum$ is correspondingly reduced by a factor of ξ. Evidently, the following general statement can be made. Given a system with resolution Δr in coordinate space and a resolution Δk in wave number space, subject only to the conditions that

$$\Delta r < \text{a typical internal wavelength}$$
$$2\pi/\Delta k > \text{relevant ripple wavelengths} \qquad (3\text{-}25)$$

then the effective $\sum$ is

$$\sum_{\text{eff}} = \frac{2\pi}{\Delta k\, \Delta r} \sum \qquad (3\text{-}26)$$

where, of course, the usual inequality $\Delta k\, \Delta r > 2\pi$ must be satisfied. Furthermore, if either of the inequalities in Eq. (3-25) is violated so that the characteristic patterns are not resolved, then $\sum_{\text{eff}}$ is less than that given in Eq. (3-26). Note that the conditions of Eq. (3-25) allow $2\pi/\Delta k\, \Delta r$ to be quite small. The extra "resolving power" needed to achieve the ideal has nothing to

do with the characteristic sizes of the internal waves or ripples. Its role is simply to reduce the effect of fluctuations in the ambient background.

Evidently, it is possible to make tradeoffs between resolution in $\underset{\sim}{k}$ and in $\underset{\sim}{r}$. Radar generally has a poor Δr and therefore requires a high resolution in $\underset{\sim}{k}$ to achieve good statistics. High resolution in $\underset{\sim}{k}$ means, of course, the ability to accurately map out G as a function of $\underset{\sim}{k}$, not just making precise masurements at one value of $\underset{\sim}{k}$.

3.2.6 Synthetic Aperture Radars (SARS)

A SAR like that on SEASAT gets it azimuthal resolution from doppler information.

It is convenient to do the analysis in three steps. In step one the sea surface is assumed to be independent of time. The motion of ripples and internal waves is included in step two and in step three the remaining effects are considered.

3.2.6.1 Frozen Sea Surface. When there is no motion of the sea surface all doppler effects are due to the velocity of the SAR

platform. In this case the analysis of sections (3)-(5) requires only trivial changes.

From the linearity of Maxwell's equations and the Born approximation, it follows that after the synthetic aperture has been formed, the scattered power can be written as

$$P \propto \left| \int e^{i\underline{k} \cdot \underline{x}} h(\underline{x}) W(\underline{x}) d^2x \right|^2 \qquad (3\text{-}27)$$

where W is a weighting function which depends on the precise algorithm used to form the aperture. If W were equal to one inside of a region S and zero outside, then Eq. (3-27) would be identical to Eq. (3-23). It is not, but the point is that a SAR is designed so the W is almost equal to unity in a resolution cell and is nearly zero outside. Thus for a well designed SAR, Eqs. (3-23) and (3-27) are almost indentical and consequently the analysis of sections (3) and (5) remains valid.

3.2.6.2 Ripples and Internal Waves. For backscattering from a ripple convected by an internal wave there is a doppler shift

$$\Delta\omega = \pm \omega_k + \underline{k} \cdot \underline{U} \qquad (3\text{-}28)$$

where $\omega_k = \sqrt{gk}$ (for gravity waves) is the intrinsic frequency of the ripple, $\underset{\sim}{k}$ is the scattering vector (twice the horizontal wave number of the radar, and $\underset{\sim}{U}$ is the internal wave water velocity. This extra doppler shift causes a SAR to slightly displace the image of the ripple. It is sufficient to work to first order in $\Delta\omega$: the two terms in Eq. (3-28) then represent independent additive effects. The first term, ω_k , is a purely kinematic effect which is independent of the internal wave. It can be ignored. The second term, $\underset{\sim}{k} \cdot \underset{\sim}{U}$, produces a local distortion of the image which is proportional to the internal wave strength. In the language of section 3 this is a deterministic effect which can be absorbed into a redefinition of γ . In radar parlance, it produces the "velocity bunching" term in the SAR cross section[2]. The detailed way in which velocity bunching enters into γ can be obtained by comparing Eq. (3-24) to the formulas given in Ref. (2).

3.2.6.3 Other Sea Surface Motions. Currents and other flows with a horizontal velocity at surface act just like internal waves.

The only other phenomenon of any significance is the tilting of ripples by long surface waves. This has the effect of adding a non-deterministic perturbation to the ω_k term in Eq. (3-28). The net result is a small random distortion of the image. When compared

to the velocity bunching term this whole effect is down by a factor of $m \sim 0.1$, where m^2 is the mean square slope of the sea surface. It is not likely to be of much consequence in practice.

In summary, to a good approximation the only difference between an ordinary radar and a SAR is that in the latter case the velocity bunching term should be included in γ.

3.2.7 Conclusions

The main results of this report are:

(i) Eqs. (3-20) and (3-21) which give the signal to noise ratio for any method of detecting an internal wave via surface roughening.

(ii) Eq. (3-24) which relates the quantities needed in (i) to radar cross sections.

(iii) The fact that to a good approximation (i) and (ii) apply to SAR provided only that the velocity bunching term^2 is included in $\frac{\delta\sigma}{\sigma}$ (or γ).

As an example, consider SEASAT. An analysis of the SEASAT geometery and processing algorithm[2] shows that: (i) the function W in Eq. (3-23) is close to unity in a region of area $\sim 100\ m^2$ and nearly zero elsewhere and, (ii), SEASAT measures the cross section only at one value of $\underline{k}_{nm}$. Then according to Eq. (3-20)

$$\sum^2 = \sum_a \frac{L^2}{\ell^2} \gamma\left(R_a\right) = \frac{1}{\ell^2} \int d^2R\gamma(\underline{R}) \qquad (3\text{-}29)$$

where the $\underline{k}$ dependence of γ has been suppressed and ℓ^2 is to be interpreted as $100\ m^2$. From Eq. (3-29) it is clear that the number of degrees of freedom available to SEASAT is one per $100\ m^2$ of ocean surface.

Finally, it is possible to extend the analysis to the more general problem of finding a special internal wave in a background which contains both speckle and random ambient internal waves. At a formal level, the only difference is that there is now a random component in γ. One is free to assume that the random part of γ averages to zero so that the expected values of G and σ are unchanged. What does change is the variance of G [Eq. (3-19)]. In computing this variance one can assume that the fluctuations in γ and h are independent (the coupling between surface and internal waves is weak). The result is an additional term on the

right hand side of Eq. (3-19) which is diagonal in the wave number indices n and m but is not diagonal in the patch indices α and α'. To proceed further it is necessary to make a Fourier transform with respect to the α indices. The variance is then diagonal, and the rest of the calculation goes through as before.

REFERENCES FOR SECTION 3.0

1. Phillips, O. M., The Dynamics of the Upper Ocean, Cambridge University Press, 1966.

2. Vesecky, J. F., and R. H. Stewart, J. Geophys. Res., 87, 3397, (1982).

3. Fu, L. L., and B. Holt, SEASAT Views Oceans and Sea Ice with Synthetic-Aperture Radar, Jet Propulsion Laboratory, Pasadena, California (1982).

4.0 KELVIN WAKES

4.1 Kinematics

The geometry of the Kelvin wake behind a ship is determined by the fact that the wave pattern is steady in the rest frame of the ship, and by the consequent dispersion relation

$$\sqrt{gk} = k_x U \tag{4-1}$$

where $k = \sqrt{k_x^2 + k_y^2}$ is the wave number of the wave, and k_x and k_y are its x and y components in a coordinate system in which the ship is moving with velocity U along the negative x axis and y is the crosstrack direction.

In the far field, the phase $k_x x + k_y y$ of the wave pattern will be stationary, so that

$$-\frac{1}{\tan\theta} = \frac{\partial k_x}{\partial k_y} \tag{4-2}$$

where θ is the angle in the wake measured from the x axis: $x = r\cos\theta$ and $y = r\sin\theta$ where r is the distance to a point in the wake from the source. The geometry is shown in Figure 4-1.

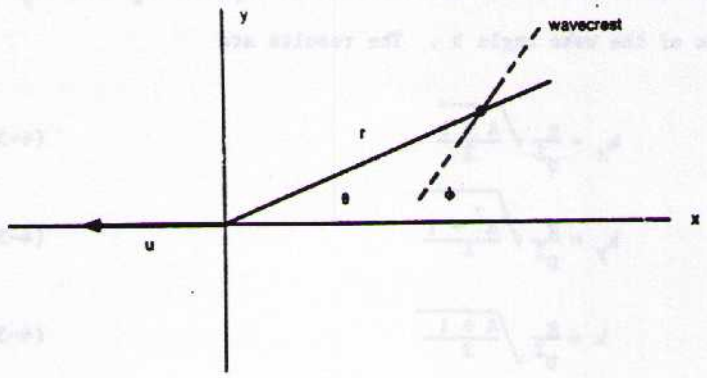

Figure 4-1. Wavecrest.

Eqs. (4-1) and (4-2) can be solved to express k_x and k_y as functions of the wake angle ϑ . The results are

$$k_x = \frac{g}{U^2}\sqrt{\frac{A+1}{2}} \qquad (4\text{-}3a)$$

$$k_y = \frac{g}{U^2}\sqrt{\frac{A^2-1}{4}} \qquad (4\text{-}3b)$$

$$k = \frac{g}{U^2}\sqrt{\frac{A+1}{2}} \qquad (4\text{-}3c)$$

where

$$A = \frac{1 \pm \sqrt{1 - 8\tan^2\theta}}{4\tan^2\theta} \quad . \qquad (4\text{-}4)$$

The two signs in Eq. (4-4) refer to two different wave systems, divergent (+ sign) and transverse (- sign). These coincide when $\tan^2\theta = 1/8$ and $A = 2$; these are the Kelvin wake caustics at $\theta = \pm \theta_c = \pm 19.5^\circ$, where $\partial^2 k_y/\partial k_x^2 = 0$. The wavelengths of the divergent waves blow up near the axis; for small θ we have

$$k_x \to \frac{g}{U^2} \cdot \frac{1}{2\theta} \qquad (4\text{-}5)$$

$$k_y \to k \to \frac{g}{U^2} \cdot \frac{1}{4\theta^2} \quad . \qquad (4\text{-}6)$$

Numerically, if $U = 10$ m/sec , a wake angle of 6° corresponds to a wavelength of 3 m; a wake angle of 3° corresponds to a wavelength of less than 1 m.

The angle the wave crests make with the axis is called ϕ , and is defined by $\tan\phi = k_x/k_y$. Then

$$\tan\phi = \frac{\tan\phi}{2 + \tan^2\phi} \qquad (4\text{-}7)$$

and for small θ , $\phi = 2\theta$.

To derive the geometry of the Kelvin wake is easy; to derive the amplitudes and slopes in the wake is hard, especially at small wake angles. As a point of reference for more sophisticated calculations, we describe below a standard approximation known as "thin ship theory."

The linearized equations of motion obeyed by the velocity potential ϕ , written in the rest frame of the ship and with z vertically upwards, are:

(i) $\nabla^2\phi = 0$

$$\text{(ii)} \quad \partial\phi/\partial z + U^2/g \; \partial^2\phi/\partial x^2 = 0 \quad \text{at} \quad z = 0$$

$$\text{(iii)} \quad \hat{n} \cdot \vec{\nabla}\phi = \hat{n} \cdot \vec{U} = n_x U \qquad \text{on hull.}$$

The first of these says the flow is incompressible and irrotational; the second is the (linearized) free surface boundary condition; the third says that the normal (to the hull) water velocity equals the (normal) ship speed on the hull ($\hat{n}$ is the unit normal to the hull). The surface displacement ζ can be calculated from the velocity potential through the (linearized) relation

$$\zeta = \frac{U}{g} \frac{\partial\phi}{\partial x} \bigg|_{z=0} .$$

Eqs. (i) through (iii) define the "Kelvin-Neumann" problem, which has never been solved. (A further discussion of it appears in Section 4.3.) "Thin ship theory" consists of replacing Eq. (iii) by the much simpler condition

$$\text{(iii)}' \quad n_y \frac{\partial\phi}{\partial y} = n_x U \qquad \text{at} \quad y = \pm 0 \; ;$$

that is, the actual hull is replaced by an infinitely thin (in the transverse direction) plate. The solution to (i), (ii), and (iii)'

can be written down easily, and one obtains for the amplitude at a point x,y in the wake

$$|\zeta(x,y)| = \frac{\sqrt{g}}{U^2}\frac{F(\theta)}{\sqrt{x}}\ \phi(k_x) \qquad (4\text{-}8)$$

where

$$F(\theta) = \frac{1}{2}\left(\frac{A+1}{2}\right)^{1/4}\sqrt{\frac{A(A-1)}{A-2}}\ , \qquad (4\text{-}9)$$

and

$$\phi(k_x) = \frac{2U^3}{g}\frac{k_x^2}{\sqrt{k_x^2 - \frac{U^4}{g^2}k_x^4}}\int_{-\infty}^{\infty} dx \int_{-}^{0} dz\ e^{-ik_x x}\, e^{(U^2/g)k_x^2 z}\,\frac{\partial Y(x,z)}{\partial x}\ . \qquad (4\text{-}10)$$

In Eq. (4-10), k_x is given by Eq. (4-3a), and $y = Y(x,z)$ is the equation of the ship's hull. Thus the integrals over dx and dz actually extend only over the ship's side, where $Y \neq 0$.

The thin ship solution, for divergent waves, gives wave amplitudes behaving like $\theta^{3/2}$ for small θ, near the wake axis, and wave slopes behaving like $\theta^{-1/2}$. In this approximation, then, larger wave slopes occur at smaller angles. Obviously this solution

fails at small θ, presumably where θ is of the order ship beam divided by ship length. If the correct theory cuts off the slope for small θ, we would expect a maximum in slope at some small wake angle; possibly this maximum could explain the SEASAT observations. We must therefore find an improvement on the thin ship solution, valid as $\theta \to 0$, to see if such a maximum actually occurs. Attempts to do this occupy Sections 4.2 and 4.3.

4.2 Kelvin-Neumann Problem (A)

4.2.1 Introduction

Wakes produced by ships have been a subject to investigation for many years.(1) There has been particular interest recently because of the pictures obtained with SEASAT.

Here we present an approximation technique to calculate wakes. As a basic assumption we assume linearization is acceptable. Further, we will assume low Froude number. For some cases this may be of interest. In any event, the structure of the solution will be instructive. In particular, it will be found that in this limit the displacements are indeed small. This lends credibility to the linearization procedure.

It has been stated[2] that the solutions have essential singularities at zero Froude number. In our treatment it will be seen how these can come about. Such a singularity does not mean we cannot approximate for small Froude number. It merely means that a convergent power series cannot be obtained.

As an example consider the function

$$f(x) = e^{x\sin\frac{1}{x}} - 1 \quad .$$

This indeed has an essential singularity at $x = 0$. However, for small (real) x it is well approximated as

$$f(x) \approx x \sin(1/x) \quad .$$

Our method consists of using Green's theorem to form an integral representation for the desired potential function. Passing to the limit where the field point is on the body of the ship yields an integral equation for the potential there. For small Froude numbers the kernel is essentially that for the potential of the flow past the ship plus its reflection in the ocean surface but without a free surface. The approximation consists in using the solution of the simplified problem as the zeroth order solution of the integral

equation. The solution elsewhere is then obtained from the integral representation. Higher order corrections (including neglected non-linear terms) can then be found by iteration--at the cost of increasing complexity.

This note is organized as follows: In Section 4.2.2 the general form of the linear problem is given. This immediately suggests the form for a perturbation theory. The possible occurrence of an essential singularity is made clear in Section 4.2.3. Further, an ambiguity which is to be resolved by physical considerations is found.

To see with clarity how the approach is implemented, Section 4.2.4 is devoted to the two dimensional case. Finally, in Section 4.2.5 the result is obtained for a two dimensional example. This is immediately generalized to a large class of bodies.

4.2.2 Formulation

Consider a ship moving with velocity U in the direction x on a sea with surface $z = 0$. Transforming to a coordinate system at rest with respect to the ship we can write the velocity potential as

$$\phi = Ux + \phi \quad . \tag{4-11}$$

Then ϕ satisfies

$$\nabla^2\phi = 0 \tag{4-12}$$

$$\frac{\partial\phi}{\partial n} = -n_x U \tag{4-13}$$

on the surface of the ship and (in linear approximation)

$$\frac{\partial^2\phi}{\partial x^2} + \frac{g}{U^2}\frac{\partial\phi}{\partial z} = 0 \tag{4-14}$$

on the free ocean surface ($z = 0$).

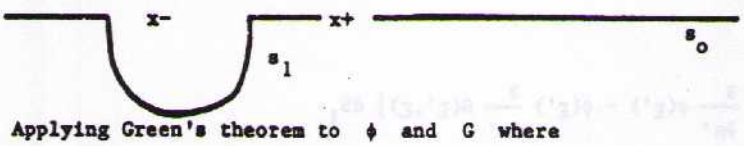

Applying Green's theorem to ϕ and G where

$$\nabla'^2 G(\xi',\xi) = \delta(\xi'-\xi) \tag{4-15}$$

and G vanishes appropriately as $|\xi'| \to \infty$ yields

$$\phi(\underset{\sim}{x}) = \int_{S_o} \left\{ G(\underset{\sim}{\xi}',\underset{\sim}{x}) \frac{\partial}{\partial z'} \phi(\underset{\sim}{\xi}') - \phi(\underset{\sim}{\xi}') \frac{\partial}{\partial z'} G(\underset{\sim}{\xi}',\underset{\sim}{x}) \right\} dS_o$$

$$+ \int_{S_1} \left\{ G(\underset{\sim}{x}',\underset{\sim}{x}) \frac{\partial}{\partial n'} \phi(\underset{\sim}{\xi}') - \phi(\underset{\sim}{\xi}') \frac{\partial}{\partial n'} G(\underset{\sim}{\xi}',\underset{\sim}{x}) \right\} dS_1 \qquad (4\text{-}16)$$

where S_i is the surface of the ship and S_o is the ocean surface (excluding the region of the ship).

Many choices of $G(\underset{\sim}{x}',\underset{\sim}{x})$ are possible. However, the most useful seems to be

$$\left\{ \frac{\partial G}{\partial z'} (\underset{\sim}{\xi}',\underset{\sim}{x}) + \frac{U^2}{g} \frac{\partial^2}{\partial x'^2} G(\underset{\sim}{\xi}',\underset{\sim}{x}) \right\} z' = 0 = 0 \qquad (4\text{-}17)$$

With this choice of G the integral over S_o reduces to an integral around the water line of the ship, i.e., the Eq. (4-16) becomes

$$\phi(\underset{\sim}{x}) = \int_{S_1} \left\{ G(\underset{\sim}{\xi}',\underset{\sim}{x}) \frac{\partial}{\partial n'} \phi(\underset{\sim}{\xi}') - \phi(\underset{\sim}{\xi}') \frac{\partial}{\partial n'} G(\underset{\sim}{\xi}',\underset{\sim}{x}) \right\} dS_1$$

$$+ \frac{U^2}{g} \int_{c-} \left\{ \phi(\underset{\sim}{\xi}') \frac{\partial}{\partial x'} G(\underset{\sim}{\xi}',\underset{\sim}{x}) - \frac{\partial \phi}{\partial x'} G(\underset{\sim}{\xi}',\underset{\sim}{x}) \right\}_{z'=0, x'=x_-(y')} dy' \qquad (4\text{-}18)$$

$$- \frac{U^2}{g} \int_{c+} \left\{ \phi(\underset{\sim}{\xi}') \frac{\partial}{\partial x'} G(\underset{\sim}{\xi}',\underset{\sim}{x}) - \frac{\partial \phi}{\partial x'} G(\underset{\sim}{\xi}',\underset{\sim}{x}) \right\}_{\substack{z'=0 \\ x'=x_+(y')}} dy'$$

Notice that Eq. (4-18) plays two roles:

(1) If $\underline{\xi}$ is on S_1 this gives an inhomogeneous integral equation for ϕ on S_1, (inhomogeneous since $\frac{\partial \phi}{\partial n'}$ is given).

(2) Given ϕ on S_1 we then have $\phi(\underline{\xi})$ everywhere.

What is needed is an approximation to the solution of the integral equation. For this we first construct the Green's function.

4.2.3 The Green's Function

This is readily constructed by Fourier transforming in x and y. The result can be written as

$$G(\underline{\xi}',\underline{\xi}) = G_o(\underline{\xi}',\underline{\xi}) + G_1(\underline{\xi}',\underline{\xi}) \tag{4-19}$$

where

$$G_o(\underline{\xi}',\underline{\xi}) = -\frac{1}{4\pi}\left\{\frac{1}{|\underline{\xi}'-\underline{\xi}|} + \frac{1}{|\underline{\xi}'-\hat{\underline{\xi}}|}\right\} \tag{4-20}$$

with

$$\hat{\xi} = (x,y,-z)$$

and

$$G_1(\xi',\xi) = -\frac{1}{(2\pi)^2}\iint \frac{d^2k}{k}\frac{k_x^2}{\left[\frac{gk}{U^2} - k_x^2\right]} e^{k(z+z')}\, e^{i[k_x(x'-x)+k_y(y'-y)]} \tag{4-21}$$

where

$$k = +\sqrt{k_x^2 + k_y^2} \quad .$$

A number of points should be noted:

(1) G_o is precisely the Green's function which would be used to calculate the potential flow in an infinite medium caused by a body consisting of the ship and its image in the $z = 0$ plane moving with velocity U. In particular, then, the solution of the integral equation with σ replaced by G_o can be determined by any of the classical methods.

(2) For small Froude number G_1 is in some sense small. Thus if we introduce dimensionless quantities in terms of a typical length of the boat, the Eq. (4-21) involves g/U^2 in the denominator. For this number large G_1 should be small. The obvious perturbation theory is then to take as the lowest order solution of the integral equation the solution $_o$ of the equation with G replaced by G_o. In particular, the lowest order wave field far from the ship can be computed from Eq. (4-18) with replaced by $_o$. Iterating, we can compute corrections to on the body and then corrections to the wave field.

(3) In this way we do not obtain a power series in U^2/gL. Such a power series would be obtained if in Eq. (4-21) we introduced the expansion

$$\frac{1}{\frac{g}{U^2}k - k_x^2} = \frac{U^2}{kg\left[1 - \frac{U^2}{g}\frac{k_x^2}{k}\right]}$$

$$= \frac{U^2}{kg}\left\{1 + \frac{U^2}{g}\frac{k_x^2}{k} + \left(\frac{U^2}{g}\frac{k_x^2}{k}\right)^2 + \ldots\right\} .$$

However, the terms in this series are successively more and more divergent. This is the origin of the "non-analytic" behavior at zero Froude number. Successive terms in our iterative series will indeed be smaller and smaller—but it will not be a power series in $U^2/\ell g$!

(4) The G of Eq. (4-21) looks peculiarly symmetric in x and $-x$. But we expect waves to appear far behind the ship and not far in front.

(5) There is an ambiguity in Eq. (4-21). Indeed singularities occur where the denominator vanishes. How are these to be treated? Physically the reason for the singularities is clear. They occur at wave numbers such that the corresponding free surface waves travel with velocity U.

The points (4) and (5) are intimately connected. Indeed, as we will see, the treatment of the singularities is completely determined by the requirement that there be waves far behind the ship but not in far in front.

It may be noted that with our choice of Green's function the integral around the water line in Eq. (4-18) is not small. Indeed it is of order

$$\ell U\left\{\frac{U^2}{\ell g}\right\}^0 .$$

However, we will see that part of the integral over S_1 cancels this identically and so we will be left with an expression of the form

$$\phi \sim \ell U\left\{\frac{U^2}{\ell g}\right\}^1 .$$

These points become especially clear if we look at the two dimensional problem to which we now turn.

4.2.4 The Two-Dimensional Problem

The formulas become much more transparent when we consider the "ship" to be infinite in the y direction and therefore omit the dependence in this direction. With obvious modifications we can take over the previous work. Thus the integral representation (and the integral equation) become

$$\phi(\xi) = \int_{S_1} \left\{ G(\xi',\xi) \frac{\partial}{\partial n'} \phi(\xi') - \phi(\xi') \frac{\partial}{\partial n'} G(\xi',\xi) \right\} dS_1$$

$$+ \frac{U^2}{g} \left\{ \phi(\xi') \frac{\partial}{\partial x'} G(\xi',\xi) - \frac{\partial \phi}{\partial x'} G(\xi',\xi) \right\}_{\substack{z'=0 \\ x'=x_-}} \qquad (4\text{-}22)$$

$$- \frac{U^2}{g} \left\{ \phi(\xi') \frac{\partial}{\partial x'} G(\xi',\xi) - \frac{\partial \phi}{\partial x'} G(\xi',\xi) \right\}_{z'=0, x'=x_+} .$$

Thus the integral over the surface of the boat is replaced by one over the arc S_1, and the integral over the waterline is replaced by contributions from the front and back.

G becomes:

$$G = G_o + G_1$$

with

$$G_o(\xi',\xi) = 1/2\pi \left\{ \ln |\xi'-\xi| + \ln |\xi'-\hat{\xi}| \right\} \qquad (4\text{-}23)$$

and

$$G_1(\underline{\xi}',\underline{\xi}) = \frac{1}{2\pi}\int_{-\infty}^{\infty} \frac{dk_x}{|k_x|}\,\frac{k_x^2}{\left[\frac{g|k_x|}{2} - k_x^2\right]}\, e^{|k_x|(z+z')}\, e^{ik_x(x'-x)} \qquad (4\text{-}24)$$

which is conveniently written without absolute values as

$$G_1 = -\frac{1}{2\pi}\int_{-\infty}^{0} \frac{dk_x}{k_x - \frac{g}{U^2}}\, e^{k_x(z+z')}\, e^{ik_x(x'-x)} + \frac{1}{2\pi}\int_{0}^{\infty} \frac{dk_x}{k_x - g/U^2}\, e^{k_x(z-z')}\, e^{ik_x(x'-x)} \,. \qquad (4\text{-}25)$$

Now it is intuitively clear that the dominant contribution to G_1 for $|x'-x|$ large will come from the poles, at $k_x = \pm g/U^2$. For simplicity consider $z = z' = 0$. Then G_1 can be written as

$$G_1 = -\frac{1}{2\pi}\int_{-\infty}^{\infty} \frac{dk_x}{k_x + \frac{g}{U^2}}\, e^{ik_x(x'-x)} + \frac{1}{2\pi}\int_{-\infty}^{\infty} \frac{dk_x}{k_x - \frac{g}{U^2}}\, e^{ik_x(x'-x)} + \frac{1}{2\pi}\int_{0}^{\infty} \frac{dk_x}{k_x + \frac{g}{U^2}}\, e^{ik_x(x'-x)} - \frac{1}{2\pi}\int_{-\infty}^{\infty} \frac{dk_x}{\left[k_x - \frac{g}{U^2}\right]}\, e^{ik_x(x'-x)} \qquad (4\text{-}26)$$

Now integrating by parts we readily see that for large $|x-x'|$ the sum of the last two terms is $O\left(\frac{1}{|x-x'|^2}\right)$.

We are left with

$$G_1 = -\frac{1}{2\pi}\int_c e^{ik_x(x'-x)}\left\{\frac{1}{k_x+\frac{g}{U^2}}-\frac{1}{k_x-\frac{g}{U^2}}\right\}dk_x \quad . \qquad (4\text{-}27)$$

It is asserted that the correct choice of c is such that one goes below both poles. Then one finds

$$G_1 = -2\sin\frac{g}{U^2}(x'-x) \quad , \quad x < x'$$

$$= 0 \quad , \quad x > x' \quad , \qquad (4\text{-}28)$$

which justifies the choice of c .

Appending the z,z' dependence gives similarly

$$G_1 = -2\,e^{\frac{g}{U^2}(z+z')}\sin\frac{g}{U^2}(x'-x) \quad , \quad x < x'$$

$$= 0 \quad , \quad x > x' \qquad (4\text{-}29)$$

4.2.5 An Example

To illustrate, we consider the case where the "ship" is an infinite semi-elliptic cylinder, i.e., in the x,z plane the bottom of the ship is described by the lower half of the ellipse

$$\frac{x^2}{a^2} + \frac{z^2}{b^2} = 1 \quad . \tag{4-30}$$

The potential flow around the full ellipse described by Eq. (4-30) is readily found.[3] It can be written so:

If

$$x = \sqrt{a^2-b^2}\,\cosh u \cos\theta$$

$$z = \sqrt{a^2-b^2}\,\sinh u \sin\theta$$

then

$$\phi_o = Ub\,\sqrt{\frac{a+b}{a-b}}\,\cos\theta\, e^{-u} \quad . \tag{4-31}$$

With $\xi = \cosh u$, the surface S_1 is given by $\xi = \xi_o$ where

$$\xi_o = -\frac{a}{\sqrt{a^2-b^2}} \quad ,$$

For a point on S_1 Eq. (4-31) gives

$$\phi_o = bU \cos\theta \tag{4-32a}$$

$$\frac{\partial \phi_o}{\partial n} = \frac{bU \cos\theta}{(a^2-b^2)(\xi_o^2-\cos^2\theta)} \quad . \tag{4-32b}$$

To calculate the surface waves produced we use Eq. (4-22) with G replaced by the asymptotic form of Eq. (4-28). (The terms in Eq. (4-22) involving G_o merely reproduce ϕ_o or give other terms which fall off algebraically behind the ship.) Let F denote the contribution to ϕ due to the integral over S_1, i.e.,

$$F = F_1 + F_2$$

where

$$F_1 = \int_{S_1} G_1^{(as)}(\xi',\xi) \frac{\partial}{\partial n'} \phi_o(\xi') \, dS_1 \tag{4-33}$$

and

$$F_2 = -\int_{S_1} \phi_o(\xi') \frac{\partial}{\partial n'} G_1^{(as)}(\xi',\xi) \, dS_1 \quad . \tag{4-34}$$

We obtain:

$$F_1 = iUb\, e^{\frac{g}{U^2}(z-ix)} \int_{\pi}^{2\pi} \cos\theta\, d\theta\, e^{\frac{g}{U^2}[b\sin\theta + ia\cos\theta]}$$

$$+ \text{complex conjugate} \qquad (4\text{-}35)$$

and

$$F_2 = i\,\frac{gb}{U}\, e^{\frac{g}{U^2}(z-ix)} \int_{\pi}^{2\pi} \cos\theta\, d\theta\, [a\sin\theta + ib\cos\theta]\, e^{\frac{g}{U^2}[b\sin\theta+ia\cos\theta]}$$

$$+ \text{complex conjugate} \qquad (4\text{-}36)$$

These integrals are readily evaluated in the limit $gb/U^2 \gg 1$ (which we have been assuming all along). Thus only the immediate vicinity of $\theta = \pi$ and $\theta = 2\pi$ will give contributions.

Thus the first approximation to the integral in Eq. (4-35) is

$$\int_{\pi}^{2\pi} \cos\theta\, e^{\frac{g}{U^2}[b\sin\theta+ia\cos\theta]}\, d\theta$$

$$= \left[-e^{\frac{-iga}{U^2}} + e^{\frac{iga}{U^2}} \right] \int_0^\infty e^{\frac{-gb}{U^2}\epsilon} \, d\epsilon = \frac{U^2}{gb} \, 2i \sin \frac{ga}{U^2} \quad , \qquad (4\text{-}37)$$

$$\text{i.e.,} \qquad F_1 \sim \frac{-2U^3}{g} e^{\frac{g}{U^2}(z-ix)} \sin \frac{ga}{U^2} + \text{c.c.} \quad .$$

Similarly, in lowest order we find

$$F_2 \sim -2Ub \, e^{\frac{g}{U^2}(z-ix)} \cos \frac{ga}{U^2} + \text{complex conjugate} \quad . \qquad (4\text{-}38)$$

One readily checks that the contributions of Eqs. (4-37) and (4-38) exactly cancel the "end point" terms in Eq. (4-22). Remark: This is a general result. The lowest order terms of the surface integral cancel the line integral in our representation.

To get a non-zero radiated field we must calculate to one higher power in U^2/gb . This only arises from F_2 and is due to the $\sin\theta$ in Eq. (4-36). Our result for the radiated field far behind the ship then becomes

$$\phi \approx 4aU \left(\frac{U^2}{bg}\right) \sin \frac{ga}{U^2} \sin \frac{gx}{U^2} e^{\frac{gz}{U^2}} \quad . \qquad (4\text{-}39)$$

Remark: This is indeed small if $\frac{U^2}{bg}$ is small.

4.2.6 Generalization

Looking at what has been done, it is seen that all that has been used were the values of ϕ_o at the endpoints and the form of the surface in the immediate neighborhood. This suggests a general class of problems for which the solution is immediate.

Thus let the backend be at $-a_1$ and the front at a_2. Assume that the surface in the vicinity of these points can be described as portions of ellipses with axis a_1, b_1, and a_2, b_2, respectively. Following our argument exactly we obtain

$$\phi(x,z) = -\phi_o(-a_1,0)2\left(\frac{a_1}{b_1}\right)\left(\frac{U^2}{b_1 g}\right)e^{gz/U^2}\sin\frac{g}{U^2}(x+a_1)$$

$$-\phi_o(a_2,0)2\left(\frac{a_2}{b_2}\right)\left(\frac{U^2}{b_2 g}\right)e^{gz/U^2}\sin\frac{g}{U^2}(x-a_2) \quad . \qquad (4\text{-}40)$$

4.2.7 Conclusion

(1) The method seems to produce reasonable results for small Froude number.

(2) What needs to be done?

(a) Realistic examples in 3 dimensions.

(b) Estimates of the corrections obtained by iteration.

(c) Estimates of the effect of neglected non-linear terms.

4.3 Kelvin-Neumann Problem (B)

4.3.1 Introduction

In Section 4.2(A) we considered the wake problem in the low Froude number limit. This was an attempt to see if there is some limit in which linear theory is adequate.

Using a coordinate system at rest with respect to the boat, we obtained an integral representation for the velocity potential $\phi(\underline{r})$. When $\underline{r}$ is on the boat hull (S) this gives an integral equation for ϕ on S. The inhomogeneous part of this equation is given in terms of the known normal component of velocity. The exact solution of the linear problem would involve solving the integral equation and then using the integral representation to obtain ϕ when $\underline{r}$ is far from S.

An approximate solution will be good if we can construct an adequate description of ϕ on S. For low Froude numbers this seems possible. The kernel of the integral equation decomposes into two parts. The first corresponds to the flow past the boat plus its image in the plane $z = 0$ in an infinite medium. The second part should be small for low Froude numbers.

The approximation suggested is to use the solution of the simple potential flow problem in the full integral representation. In Section 4.2(A) the general formulation was given. For illustrative purposes the two-dimensional case was treated. It was indicated that three-dimensional examples should be calculated. Here we consider a simple but not completely ridiculous case.

4.3.2 Boat Model

We model the hull as half of a prolate ellipsoid. To be specific, we introduce spheroidal coordinates such that

$$x = c \cosh\eta \cos\theta \tag{4-41}$$

$$y = c \sinh\eta \sin\theta \cos\omega \tag{4-42}$$

$$z = c \sinh\eta \sin\theta \sin\omega \tag{4-43}$$

Then the hull is the surface

$$\eta = \eta_o \ , \qquad 0 \leq \theta \leq \pi \ , \qquad \pi \leq \omega \leq 2\pi \ .$$

Thus the major and minor axes are $a = c \cosh\eta_o$ and $b = c \sinh\eta_o$, respectively.

4.3.3 The Potential Flow Problem

The problem to be solved is that of finding the solution of Laplace's equation with the boundary conditions $\phi_o \to 0$ as $|\Sigma| \to \infty$ and

$$\frac{\partial}{\partial n} \phi_o = -n_x U \tag{4-44}$$

on the surface

$$\eta = \eta_o \ , \qquad 0 \leq \theta \leq \pi \ , \qquad 0 \leq \omega \leq 2\pi \ .$$

In general orthogonal coordinates, Laplace's equation becomes

$$\left\{\frac{\partial}{\partial u_1} \frac{h_2 h_3}{h_1} \frac{\partial}{\partial u_1} + \frac{\partial}{\partial u_2} \frac{h_3 h_1}{h_2} \frac{\partial}{\partial u_2} + \frac{\partial}{\partial u_3} \frac{h_1 h_2}{h_3} \frac{\partial}{\partial u_3}\right\}\phi = 0 \ . \tag{4-45}$$

In our present coordinates

$$h_1 = h_2 = c\sqrt{\sinh^2\eta\cos^2\theta + \cosh^2\eta\sin^2\theta}$$

$$h_3 = c\sinh\eta\sin\theta \quad .$$

Note: It is convenient to introduce

$$\zeta = \cosh\eta \ , \qquad \mu = \cos\theta \quad .$$

Then

$$h_1 = h_2 = c\sqrt{\zeta^2 - \mu^2}$$

$$h_3 = c\sqrt{(\zeta^2-1)(1-\mu^2)}$$

and Laplace's equation becomes

$$\frac{\partial}{\partial\zeta}\left\{(\zeta^2-1)\frac{\partial\phi_o}{\partial\zeta}\right\} + \frac{\partial}{\partial\mu}\left\{(1-\mu^2)\frac{\partial\phi_o}{\partial\mu}\right\} + \frac{(\zeta^2-\mu^2)}{(1-\mu^2)(\zeta^2-1}\frac{\partial^2\phi_o}{\partial\omega^2} = 0 \quad . \tag{4-46}$$

The close relation of this problem to the two dimensional problem of an ellipse described in Section 4.2(A) suggests looking for a solution of the form

$$\phi_o = \mu g(\zeta) \quad . \tag{4-47}$$

(One readily shows that the boundary condition of Eq. (4-44) can then be satisfied). Inserting this ansatz in Eq. (4-46) yields

$$\frac{\partial}{\partial \zeta}\left[(\zeta^2 - 1)\frac{\partial g}{\partial \zeta}\right] = 2g(\zeta) \quad . \tag{4-48}$$

We need the solution of this which vanishes at ∞. [An overall constant is then determined by Eq. (4-44)].

One solution of Eq. (4-48) is found by inspection. It is

$$g_1(\zeta) = \zeta \quad .$$

This, of course, does not satisfy the condition at infinity. However, it is well known that given one solution of a linear second order differential equation a second can be obtained in terms of quadrature. In this case, the requisite integrals can be explicitly evaluated. We find

$$g_2(\zeta) = 2 + \zeta \ln\left[\frac{\zeta - 1}{\zeta + 1}\right] \quad . \tag{4-49}$$

One readily checks that Eq. (4-48) is satisfied and $g_2(\zeta) \to 0$ as $\zeta \to 0$.

Using Eq. (4-44) we then obtain

$$\phi_o = -\mu U c \frac{\left\{2 + \zeta \ln \frac{(\zeta-1)}{(\zeta+1)}\right\}}{\frac{2\zeta_o}{\zeta_o^2 - 1} + \ln \frac{(\zeta_o - 1)}{(\zeta_o + 1)}} \equiv -\mu U c f(\zeta) \quad . \tag{4-50}$$

4.3.4 Asymptotics of the Green's Function

The radiated wave field is to be calculated from Eq. (4-15) of 4.2(A) by inserting ϕ_o for ϕ , and G_1 for G . In particular, for the far field we need G_1 for large distances back of the boat. Let us evaluate the asymptotic form in the low Froude number limit.

In 4.2(A) Eq. (4-21) we had found that

$$G_1(\xi', \xi) = -\frac{1}{(2\pi)^2} \iint \frac{d^2k}{k} \frac{k_x^2}{\left[\frac{gk}{U^2} - k_x^2\right]} e^{k(z+z')} e^{i\left[k_x(x'-x) + k_y(y'-y)\right]} \tag{4-51}$$

Guided by the two-dimensional case we expect the major contribution to the asymptotics to come from the zeros of the denominator. These are where

$$k_x^2 = \frac{g}{U^2} k$$

and k_x on the real axis. (We remember that the causality requirement means we are to go below both poles). These points are at

$$k_x = \pm K(k_y) \tag{4-52}$$

where

$$K(k_y) = \frac{\sqrt{\frac{g^2}{U^4} + \sqrt{\frac{g^4}{U^8} + \frac{4g^2}{U^4} k_y^2}}}{2} . \tag{4-53}$$

The contribution from these points is then

$$G_1 = \frac{-i}{2\pi} \int_{-\infty}^{\infty} dk_y \left. \frac{k_x^2 e^{k(z+z')}}{k \frac{\partial}{\partial k_x} \left[\frac{gk}{U^2} - k_x^2\right]} \right|_{k_x = K} e^{i\left[K(x'-x) + k_y(y'-y)\right]} + \text{c.c.} \tag{4-54}$$

We further approximate this when $|x'-x|$ is large, by using stationary phase to do the k_y integration. For simplicity we look at the not uninteresting region where $|y-y'| \ll |x-x'|$. The stationary phase point

$$\frac{\partial K}{\partial k_y} = 0 \qquad (4\text{-}55)$$

yields

$$k_y = 0 \quad .$$

The stationary phase integration is then readily performed with the result

$$G_1 = A(x,y,z)\, B(z',x') + c.c. \quad , \qquad (4\text{-}56)$$

where

$$A = \frac{e^{-(i\pi)/4}}{\sqrt{2\pi}} \quad \frac{\overline{g}}{(-x)U^2}\, e^{igy^2/2U^2x}\, e^{g(z-ix)/U^2} \quad , \qquad (4\text{-}57)$$

and

$$B = e^{g(z'+ix')/U^2} \quad . \qquad (4\text{-}58)$$

Here we have also assumed $|x| \gg |x'|$, $|y| \gg |y'|$.

4.3.5 The Radiated Wave Field

The velocity potential far behind the boat is now to be obtained using Eq. (4-18) of 4.2(A) with ϕ replaced by the ϕ_o of Eq. (4-20) and G replaced by G_1 of Eq. (4-26), i.e.,

$$\phi(\underline{r}) = A[I_1 + I_2 + I_3 + I_4 + I_5 + I_6] + c.c. \qquad (4\text{-}59)$$

Here,

$$I_1 = \frac{U^2}{g} \int_{c+} \frac{\partial \phi_o}{\partial x'} B \, dy'$$

$$I_2 = -\frac{U^2}{g} \int_{c-} \frac{\partial \phi_o}{\partial x'} B \, dy'$$

$$I_3 = \int_S B \frac{\partial}{\partial n'} \phi_o \, dS'$$

$$I_4 = -\frac{U^2}{g} \int_{c+} \phi_o \frac{\partial}{\partial x'} B \, dy'$$

$$I_5 = \frac{U^2}{g} \int_{c-} \phi_o \frac{\partial}{\partial x'} B \, dy'$$

$$I_6 = -\int_S \phi_o \frac{\partial}{\partial n'} B \, dS'$$

We now calculate these integrals tc the first non-vanishing order in Froude number.

Let us illustrate: For I_1 we need $\frac{\partial \phi_o}{\partial x'}$ on the water line. This can be written as

$$\frac{\partial \phi_o}{\partial x'} = \frac{\mu(\zeta_o^2 - 1)\frac{\partial \phi_o}{\partial \zeta} + \zeta_o[1 - \mu^2]\frac{\partial \phi_o}{\partial \mu}}{c[\zeta_o^2 - \mu^2]} \quad . \tag{4-60}$$

It will be seen that the dominant contribution to our integrals come from the regions $\mu^2 \approx 1$. Then to calculate to zeroth and first order we can replace $\frac{\partial \phi_o}{\partial x'}$ by

$$\frac{\partial \phi_o}{\partial x'} = \frac{\mu}{c}\frac{\partial \phi_o}{\partial \zeta}\bigg|_{\zeta_o} \quad . \tag{4-61}$$

Then

$$I_1 \approx \frac{-U^3}{g}\frac{\partial f}{\partial \zeta}\bigg|_{\zeta_o} \int_{c+} e^{igacos\theta/U^2}\cos^2\theta \, dy \quad . \tag{4-62}$$

Here $c+$ is the part of the waterline of the hull for $x > 0$. The spheroidal coordinates of this curve are so:

$c+$ is $0 \leq \theta \leq \frac{\pi}{2}$.

Then

$$y = b \sin\theta \cos\omega \quad ,$$
$$z = b \sin\theta \sin\omega \quad .$$

The waterline is clearly

$$\omega = 2\pi \quad \text{and} \quad \omega = \pi \quad .$$

As y goes from 0 to b, θ goes from 0 to $\pi/2$, and $dy = b \cos\theta \, d\theta$. As y goes from $-b$ to 0, θ goes from $\frac{\pi}{2}$ to 0, and $dy = -b \cos\theta \, d\theta$. Therefore, the total integral over $c+$ is:

$$I_1 = \frac{-U^3}{g} \frac{\partial f}{\partial \zeta_o} c \sqrt{\zeta_o^2 - 1} \left\{ \left(\int_0^{\pi/2} - \int_{\pi/2}^{0} \right) e^{igac\cos\theta/U^2} \cos^3\theta \, d\theta \right. \quad ,$$

i.e.,

$$I_1 = \frac{-2U^3}{g} \frac{\partial f}{\partial \zeta_o} c \sqrt{\zeta_o^2 - 1} \int_0^{\pi/2} e^{igac\cos\theta/U^2} \cos^3\theta \, d\theta \quad . \qquad (4\text{-}63)$$

Similar considerations lead to the result

$$I_2 = -\frac{2U^3}{g}\frac{\partial f}{\partial \zeta_o} c \sqrt{\zeta_o^2 - 1} \int_{\pi/2}^{\pi} e^{igacos\theta/U^2} \cos^3\theta \, d\theta \quad . \tag{4-64}$$

Putting in the appropriate surface element area and normal derivative, we have for I_3 the formula

$$I_3 = Uc^2(\zeta_o^2 - 1)\frac{\partial f}{\partial \zeta_o}\int_{o}^{\pi} d\theta \, \sin\theta \cos\theta \, e^{igacos\theta/U^2}\{\ \} \quad , \tag{4-65}$$

$$\text{with} \quad \{\ \} = \int_{\pi}^{2\pi} e^{gbsin\theta sin\omega/U^2} d\omega \quad .$$

The principal contributions here come from the end points. To the first two orders we get

$$\{\ \} = \frac{2U^2}{gbsin\theta} \quad . \tag{4-66}$$

Then

$$I_3 = \frac{2U^3}{g} c \sqrt{\zeta_o^2 - 1}\frac{\partial f}{\partial \zeta_o}\int_{o}^{\pi} e^{igacos\theta/U^2} \cos\theta \, d\theta \quad . \tag{4-67}$$

Adding Eqs. (4-62), (4-64), and (4-67) we obtain

$$I_1 + I_2 + I_3 = \frac{2U^3}{g} c \sqrt{\zeta_o^2-1} \frac{\partial f}{\partial \zeta_o} \int_o^\pi e^{igacos\theta/U^2} cos\theta[1-cos^2\theta]d\theta \quad . \tag{4-68}$$

But this shows that the sum is zero to the first two orders.

Similarly, almost all the terms of first two orders in $I_4 + I_5 + I_6$ cancel. One does not. This arises in I_4 and is

$$I = -Uc^2 f(\zeta_o) \sqrt{\zeta_o^2-1}\, \zeta_o \frac{gc}{U^2} \int_o^\pi sin^2\theta\, cos\theta\, e^{igacos\theta/U^2}\, d\theta\, K(\theta) \tag{4-69}$$

with

$$K(\theta) = \int_\pi^{2\pi} e^{gbsin\theta sin\omega/U^2} sin\omega\, d\omega \quad . \tag{4-70}$$

In lowest order, this gives

$$K(\theta) = 2\left(\frac{U^2}{gbsin\theta}\right)^2 \quad . \tag{4-71}$$

Then

$$I = -2Uacf(\zeta_o) \frac{U^2}{gb} \int_o^\pi e^{igacos\theta/U^2} cos\theta\, d\theta \quad . \tag{4-72}$$

The integral in Eq. (4-72) is recognizable as a Bessel function. We can look up the asymptotic form or directly use the stationary phase approximation. Thus

$$\int_0^{\pi} e^{iga\cos\theta/U^2} \cos\theta \, d\theta \approx i \frac{2\pi U^2}{ga} \sin\left(\frac{ga}{U^2} - \frac{\pi}{4}\right) \quad . \qquad (4.73)$$

Then Eq. (4-72) becomes:

$$I = -2i \sqrt{2\pi}\, U a c f(\zeta_o) \frac{\overline{b}}{a} \left(\frac{U^2}{gb}\right)^{3/2} \sin\left(\frac{ga}{U^2} - \frac{\pi}{4}\right) \quad . \qquad (4-74)$$

Using this result and Eq. (4-57), we see that Eq. (4-58) says that

$$\phi = -4Ucf(\zeta_o) \frac{\overline{a}}{(-x)} \frac{U^2}{gb} e^{gz/U^2} \sin\left(\frac{ga}{U^2} - \frac{\pi}{4}\right)\cos\left[-\frac{g}{U^2}\left(x - \frac{Y^2}{2x}\right) - \frac{\pi}{4}\right] \quad . \qquad (4-75)$$

4.3.6 Conclusions

(1) For smooth hulls of the type considered here, we do seem to have a consistent expansion in Froude number.

(2) All the contributions to the far wake arise from the immediate vicinity of the bow and stern. Presumably, the shape of the boat there will largely determine a specific wake.

(3) Protuberances which emphasize other places on the hull may have large effects.

4.4 Propeller Wakes

As described in Section 4.1 of this report, the kinematics of the Kelvin wake of the ship's hull are determined by the dispersion relation

$$\sqrt{gk} = k_x U \quad ; \tag{4-76}$$

this leads directly to the caustics at angles of $\pm$ 19.5° as well as to the wavelength dependence on wake angle outlined earlier. When the source strength is not steady, but oscillatory, as is the case for the ship's propeller, then the dispersion relation changes to

$$\sqrt{gk} = k_x U + \omega_o \tag{4-77}$$

where ω_o is the angular frequency of the oscillating source. The kinematics associated with the Kelvin wake of the propeller is thus very different from that of the hull.

As before, the stationary phase point is determined from

$$-\frac{1}{\tan\theta} = \frac{\partial k_y}{\partial k_x} \tag{4-78}$$

where θ is the angle in the wake relative to the wake axis. The caustic occurs when, in addition,

$$\frac{\partial^2 k_y}{\partial k_x^2} = 0 \quad . \tag{4-79}$$

From Eqs. (4-77), (4-78), and (4-79), it is straightforward to show that for an oscillating source, the caustic angle θ_c satisfies

$$(y + 1)(y - 1/8) - \frac{18}{\sqrt{6}} \left(\frac{U\omega_o}{g}\right) y^2 \sqrt{\frac{1 + y}{y}} + \frac{27}{2} \left(\frac{U\omega_o}{g}\right)^2 y^2 = 0 \tag{4-80}$$

where $y = \tan^2\theta_c$. When $U\omega_o/g = 0$, this yields $y = 1/8$, which corresponds to the steady source caustics at $\theta_c = \pm 19.5^\circ$. However, when $U\omega_o/g \gg 1$, the solution is

$$y = \frac{1}{\sqrt{108}} \frac{1}{(U\omega_o/g)} \quad . \tag{4-81}$$

In between, y becomes infinite at $U\omega_o/g = \sqrt{2/27}$. A sketch of y versus $U\omega_o/g$ is shown in Figure 4-2.

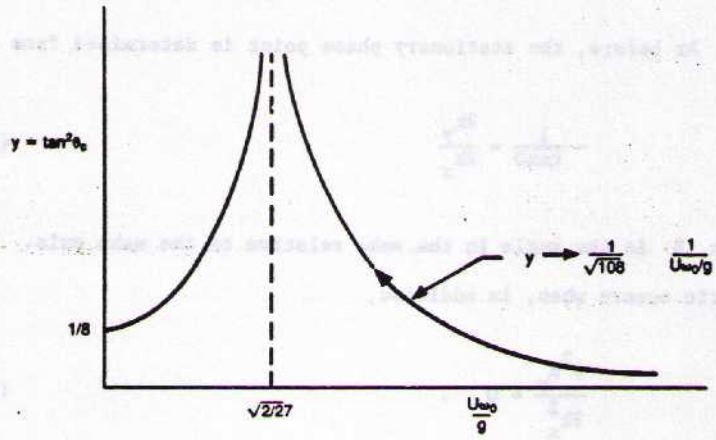

Figure 4-2. A sketch of y versus $U\omega_0/g$ is shown.

Numerically, typical values are $U \sim 10$ m/sec and $\omega_o \gg 1$. The propeller source is thus in the $U\omega_o/g \gg 1$ regime. For $\omega_o = 10$ rad/sec, we have

$$\theta_c = \pm 6^o \quad .$$

The propeller caustics are thus expected to be at quite small angles. Furthermore, since ω_o, the propeller blade rate, is roughly proportional to ship speed U, one expects that θ_c is roughly proportional to U^{-1}: slower ships have wider propeller caustics.

The wavelengths and slopes in the propeller Kelvin wake are determined by Eqs. (4-77) and (4-78). For small values of the wake angle $\theta (\theta < \theta_c)$, the relations between k_x and k_y and θ are nearly the same as in the $\omega_o = 0$ case. Thus we again expect large slopes at small angles.

The difficulty with the propeller caustics as an explanation of the SEASAT images lies in the relatively small amplitudes probably associated with them--though, to be sure, it is difficult to make reliable quantitative calculations. As a model, we may describe the propeller as an oscillating pressure distribution

$p_o(\vec{x})e^{-i\omega_o t}$. The solution of the linearized problem with this source results in wave amplitudes, far from the source and on the caustics, of

$$|\zeta| = \frac{1}{4\pi\rho U} \frac{\Gamma(1/3)}{2^{5/12}\, 3^{1/3}} \frac{g^{1/6}}{U^{11/6}} \frac{\sqrt{\omega_o}}{\theta_c^{5/3}\, x^{1/3}} p_o(k_x, k_y) \qquad (4\text{-}82)$$

where k_x and k_y are to be evaluated at $\theta = \theta_c$. In deriving Eq. (4-82), we have specialized to the case $\theta_c \ll 1$, or $U\omega_o/g \gg 1$. Note the characteristic caustic fall off of $x^{-1/3}$ with distance behind the ship, in contrast to the $x^{-1/2}$ behavior off the caustic.

The source strength $p_o(k_x, k_y)$ is proportional to exp (-kd), where d is the effective depth of the propeller. For the small angles, and short wavelengths, in the divergent wave system of interest to us, k is very large. Therefore, if the effective depth d is anything other than zero, the source is strongly damped and the propeller wake amplitudes and slopes are far too small to be relevant to SEASAT. Only if the source is really the entire turbulent flow field around the propeller, and if this flow field extends up to the surface, could the amplitudes be significant.

We really do not know how to model the propeller source, so we really cannot reliably calculate $p_o(k_x,k_y)$. But it seems unlikely that it could be big enough to give the kind of wave slopes in the wake for which we are looking.

APPENDIX 4A

It is illuminating to treat the two dimensional case in some generality. The nature of the cancellation of the "endpoint" terms and the implicit assumptions of our semi-ellipse model become clear.

Let the hull of the "boat" be described by the curve

$$x = \zeta(z) \quad . \tag{4A-1}$$

The endpoints are to be at $x = -a_1$ and $x = a_2$,

$-a_1 = \zeta(o)$

$a_2 = \zeta(o)$,

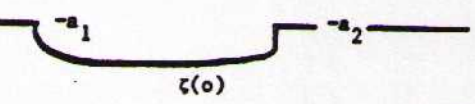

(4A-2)

We will assume

$$\left.\frac{\partial \zeta}{\partial z}\right|_{z=o} = 0 \quad .$$

This seems to be a necessary assumption if we are to argue in any generality. Otherwise the boundary value problem to be solved for ϕ_o will involve a surface with cusps at the ends. In general ϕ_o

(or some of its derivatives) will be singular there. Explicit asymptotic results will depend on the nature of the singularity and hence be very model dependent.

The endpoint terms in Eq. (4-22) are

$$\frac{U^2}{g}\left\{\phi_o(-a_1,0)\frac{\partial}{\partial x'}G_1(-a_1,0;\xi) - \frac{\partial\phi_o}{\partial x'}(-a_1,0)G_1(-a_1,0;\xi)\right\} \qquad (4A\text{-}3)$$

plus similar terms evaluated at a_2 .

The integral over s_1 in Eq. (4-22) can be converted to an integral over z of the form

$$I = \int_{s_1}\left\{G_1(\xi',\xi)\left[\frac{\partial\phi_c(x',z')}{\partial x'} - \frac{\partial\zeta}{\partial z'}\frac{\partial}{\partial z'}\phi_o(x',z')\right.\right.$$

$$\left.\left. - \phi_o(\xi')\left[\frac{\partial}{\partial x'}G_1(\xi',\xi) - \frac{\partial\zeta}{\partial z'}\frac{\partial}{\partial z'}G_1(\xi',\xi)\right]\right]\right\}dz' \quad . \qquad (4A\text{-}4)$$

For G_1 we use the asymptotic form given by Eq. (4-29). With the assumptions that have been made the only significant contributions to the integral come from the vicinity of the points $x' = a_1, z' = o$ and $x' = a_2, z' = 0$.

Since $\left.\frac{\partial \phi_o}{\partial z'}\right|_{z'=o} = 0$ and by assumption $\left.\frac{\partial \zeta}{\partial z'}\right|_{z'=o} = 0$ we readily see that to lowest order the contribution of the left endpoint is

$$I_o = \frac{\partial}{\partial x'} \phi_o(-a_1,0) \int G_1(\xi',\xi)\, dz' - \phi_o(-a_1,0) \int \frac{\partial}{\partial x'} G_1(\xi',\xi)\, dz' \quad . \tag{4A-5}$$

Then since only the vicinity of $z' = 0$ contribute to the integrals, we can write the limits as zero to infinity. But using our asymptotic representation we then obtain

$$\int_o^\infty G_1(\xi',\xi)dz' = \frac{U^2}{g} G_1(-a_1,0;\xi) \tag{4A-6}$$

and

$$\int_o^\infty \frac{\partial}{\partial x'} G_1(\xi',\xi)dz' = \frac{U^2}{g} \frac{\partial}{\partial x'} G_1(-a_1,o);r) \quad . \tag{4A-7}$$

Then Eq. (4A-5) becomes

$$I_o = \frac{U^2}{g} \{\frac{\partial}{\partial x'} \phi_o(-a_1,0) G_1(-a_1,0;\xi) - \phi_o(-a_1,0) \frac{\partial}{\partial x'} G_1(-a_1,0;\xi) \quad . \tag{4A-8}$$

Comparing with the expression of (4A-3) we see that these just cancel.

Similarly, the lowest order contributions from the right end point cancel the other terms in (4A-3).

Thus we must proceed to the next order of approximation to Eq. (4A-4). It is readily seen that this arises from the last term in (4A-4); i.e.,

$$I_1 = \int \phi_o(\xi') \frac{\partial \zeta}{\partial z'} \frac{\partial}{\partial z'} G_1(\xi', \xi)\, dz' \quad . \tag{4A-9}$$

Consider the contributions from the left end point. Since $\frac{\partial \zeta}{\partial z'} = 0$ there we must Taylor expand. This yields

$$I_1 = +\phi_o(-a_1, 0) \frac{\partial^2 \zeta}{\partial z'^2}\Bigg|_{\substack{z'=0 \\ x'=-a_1}} \int z' \frac{\partial}{\partial z'} G_1(\xi', \xi)\, dz' \quad . \tag{4A-10}$$

Again to evaluate the integral we use the asymptotic form of G_1 and extend the limit to infinity. The result is

$$I_1 = -\phi_o(-a_1, 0) \frac{\partial^2 \zeta}{\partial z'^2}\Bigg|_{\substack{z'=o \\ x'=-a}} \frac{U^2}{g} G_1(-a_1, 0; \xi) \quad . \tag{4A-11}$$

There is a similar contribution at the right end point. The overall result [generalizing Eq. (4-40)] is

$$\phi(x,z) = -\phi_o(-a_1,0)\left.\frac{\partial^2\zeta}{\partial x'^2}\right|_{\substack{x'=-a_1\\z'=0}} \frac{U^2}{g}\, 2\, e^{gz/U^2} \sin\frac{g}{U^2}(x+a_1)$$

$$-\phi_o(a_2,0)\left.\frac{\partial^2\zeta}{\partial x'^2}\right|_{\substack{x'=+a_2\\z'=0}} \frac{U^2}{g}\, 2\, e^{gz/U^2} \sin\frac{g}{U^2}(x-a_2) \quad . \tag{4A-12}$$

REFERENCES FOR SECTION 4.0

1. See for example: "Hydrodynamics," H. Lamb, 6th edition, Chap. IX, Dover Publications, N.Y., 1945.

2. M. Tulin, private communication.

3. H. Lamb, op. cit., p. 84.

5.0 TURBULENT WAKES

5.1 Abstract

Turbulent wakes of surface ships can persist for considerable distances. A number of wind tunnel and water tank studies are available for wakes of bodies when cylindrical symmetry obtains. These observations are supplemented in some detail by theoretical calculations. The cases of cylindrical symmetry are reviewed here. The SAI FASTWAKE code can model a surface ship wake in the rigid lid approximation. A review of some calculations done with this code is also given.

5.2 Introduction

Turbulent wakes of surface vessels may often be observed to extend for some kilometers on a relatively calm ocean surface. Such wakes seem also to appear in part of the SEASAT L-Band radar imagery of surface ship wakes. In spite of the ready visibility of turbulent wakes, the hydrodynamic structure and the interaction with ambient surface waves do not seem to have received much study.

In constrast to this, a considerable body of experimental and theoretical literature is devoted to studying turbulent wakes of submerged bodies. This may be associated with the apparent relative simplicity of a wake entirely within a uniform, or slowly varying, fixed medium. In view of this, we are driven to review first the modeling of submerged wakes. To our knowledge there is only one available numerical model (the Science Applications FASTWAKE Model) which can treat surface ship wakes--and this code was originally developed to study submerged body wakes.

5.3 Submerged Body Wake

A number of experimental observations in wind tunnels and water tanks are available for towed and self-propelled bodies. Chevray[1] studied the mean and turbulent flow behind a spheroid. Naudascher[2] studied the flow behind a disc having a jet at the center to simulate a self-propelled body. Gran[3] studied the wake of a slender body in a wind tunnel. A propeller on the body was driven at such a speed to give a momentumless wake. Lin and Pao[4] observed the wake of a slender body in a towing tank (fresh tap water was used). Ten hot-film probes and 20 constant temperature hot-film anemometers were mounted on a carriage moving at a constant distance behind the body.

These observations have provided data on the radial and downstream profile of mean flow, swirl, turbulent energy, and turbulent shear.

Theoretical analysis of these observations all use some form of turbulent closure model. Lin and Pao[4] use a relatively simple eddy viscosity modeling (3 parameters), Lewellen, Teske, and Donaldson[5] employ a considerably more elaborate model.[6] This has four scale parameters which were taken from a match to boundary layer and freejet data (not re-adjusted for the wake calculations). The FASTWAKE model[7],[8] uses a closure scheme of intermediate complexity. A brief discussion of these models is given in the Appendix.

In spite of apparent differences in the turbulent closure scheme, these models all show very similar features for the flow and generally agree pretty well with the observed data. This suggests that momentum and energy conservation, combined with empirically scaled transverse mixing rates, may dominate the physical phenomena in the flow.

To describe this, we choose a cylindrical coordinate system (r, ϕ, z) with the z-axis being an axis of symmetry along the wake. The corresponding velocity components are (u, v, w), with

W_o = free stream velocity.

The body is assumed to be fixed near $z = 0$. We write

$$u = U + u' ,$$
$$v = V + v' ,$$
$$w = W + w' , \qquad (5\text{-}1)$$

where $U = \langle u \rangle$, etc., and V is the "swirl velocity."

Self-similar scaling appears to obtain at $z/D \sim 10$ to 10's (D = body diameter). These relations, as observed in refs. (3) and (4), and calculated, are for a self-propelled body.

$$\frac{(W - W_o)_{r=0}}{W_o} = 1.0\left(\frac{z}{DC_D^{1/3}}\right)^{-1} \text{ (velocity defect)}$$

$$\left(\frac{V}{W_o}\right)_{r=0} = 0.4\left(\frac{z}{DC_D^{1/3}}\right)^{-3/4} \text{ (swirl velocity)}$$

$$\left(\frac{\overline{\langle w'^2 \rangle}}{W_o}\right)_{r=0} = \frac{1}{3}\left(\frac{z}{DC_c^{1/3}}\right)^{-3/4}$$

$$\frac{r_{1/2}}{DC_D^{1/3}} = 0.9\left(\frac{z}{DC_D^{1/3}}\right)^{1/4} \quad . \qquad (5\text{-}2)$$

Here C_D is the drag coefficient of the body (nominally, say, $C_D = 0.2$), z is the downstream distance measured from a point empirically determined (but normally within two or so body diameters from the after end of the body).

For a towed body the mean velocity defect and turbulent velocity decay as $z^{-2/3}$, while the wake radius grows as $z^{1/3}$. In contrast to the above, for a stratified fluid

$$\left(\frac{W-W_o}{W_o}\right)_{\text{on axis}} \sim \frac{1}{\sqrt{z}} \quad . \qquad (5\text{-}3)$$

Quantities measured and calculated as functions of radius and downstream distance are

$$(W-W_o)\ ,\ V\ ,\ \sqrt{\langle w'^2\rangle}\ ,\ \sqrt{\langle u'^2\rangle}\ ,\ \text{and}\ \langle u'w'\rangle \quad .$$

Detailed comparisons are given in refs. (4), (5), and (8). As noted above, the agreement of calculations and observations seems to be pretty good. Lin and Pao[4] had three parameters available for their model. Lewellen et al.[5] had four parameters, but these had

previously been fixed by other experiments with different flow geometry.

5.4 Surface Ship Wakes

Cylindrical symmetry obviously does not obtain for wakes of surface ships. The portion of the wake behind the propeller will have a momentum excess. The turbulent wake from the hull will have a momentum deficit--sharing with the Kelvin wake the drag force on the ship. The swirling wake of the propeller will grow, entraining fluid from the hull boundary layer. Because of wind resistance and surface wave radiation, the total wake is expected to have a momentum excess.

The Science Applications, Inc., FASTWAKE is a three-dimensional, time-independent code capable of handling a surface ship wake in the rigid lid approximation. The model on which this code is based is described briefly in the Appendix.

The FASTWAKE code was run by G. E. Innis[11] to model the turbulent wake of the Quapaw (60 m LWL and D = 7 m beam) at a speed of 15 kts. The results of the run are summarized as follows:

$$q|_{r=0} \sim z^{-\frac{5}{4}},$$

$$(w - w_o)|_{r=0} \sim z^{-6.2} \text{ for } \frac{z}{D} < 400$$

$$\sim z^{-0.5} \text{ for } \frac{z}{D} > 400$$

(= 0.1 m/sec at 3700 m)

$$r_{1/2} \sim z^{1/2} \text{ for } \frac{z}{D} < 100$$

$$\sim z^{1/4} \text{ for } \frac{z}{D} > 100 \qquad (5\text{-}4)$$

For further details reference (11) should be consulted.

It is likely that the turbulent wake is sensitive to the radial structure of the hull induced drag field. This sensitivity has not at present been explored.

APPENDIX TO SECTION 5.0

In this appendix we give a short review of the LP [ref. (4)], the LTD [ref. (5)], and the FW [ref. (7)] models. For simplicity of presentation we assume axial symmetry (only the FW model does not).

The equations for the mean flow are given, for example, on pg. 27 of ref. (9): For example, incompressible fluid of uniform density the equation of continuity reads

$$\frac{1}{\gamma}\frac{\partial}{\partial \gamma}(\gamma U) + \frac{\partial W}{\partial z} = 0 \quad . \tag{5A-1}$$

If $\underset{\sim}{f} = (f_z, f_\phi)$ represents a body force acting on unit mass of fluid, the equations of motion are

$$W\frac{\partial W}{\partial z} + U\frac{\partial W}{\partial \gamma} = -\frac{1}{\rho}\frac{\partial \overline{P}}{\partial z} -$$

$$-\frac{\partial}{\partial z}\langle w'^2\rangle - \frac{1}{\gamma}\frac{\partial}{\partial \gamma}(\gamma\langle u'w'\rangle) + f_2 \, , \tag{5A-2}$$

$$W\frac{\partial V}{\partial z} + U\frac{\partial V}{\partial \gamma} + \frac{UV}{\gamma} = -\frac{1}{\gamma^2}\frac{\partial}{\partial \gamma}(\gamma^2\langle u'v'\rangle)$$

$$-\frac{\partial}{\partial z}(\langle v'w'\rangle) + f_\phi \quad , \tag{5A-3}$$

$$W \frac{\partial U}{\partial z} + U \frac{\partial U}{\partial r} - \frac{V^2}{r} = - \frac{1}{\rho} \frac{\partial \bar{P}}{\partial r} - \frac{1}{r} \frac{\partial}{\partial r} \left(\langle u'^2 \rangle \right)$$

$$+ \frac{\langle v'^2 \rangle}{r} - \frac{\partial}{\partial z} \left(\langle u'w' \rangle \right) \quad . \qquad (5A-4)$$

Here ρ is the fluid density and $\bar{P}$ is the mean pressure.

Equations to determine $\langle u'v' \rangle$, $\langle u'^2 \rangle$, etc., are reviewed in Hinze.[9] These equations contain third order quantities $\langle u'^3 \rangle$, $\langle u'v'w' \rangle$, etc., for which there is another set of equations involving fourth order averages, etc. All models employ some closure scheme.

Relations expressing conservation of momentum and angular momentum may be obtained directly from (5A-3) and (5A-4).

First, we re-write (5A-3) as

$$\frac{\partial}{\partial z} (VW) + \frac{1}{r^2} \frac{\partial}{\partial r} (r^2 VU) = - \frac{1}{r^2} \frac{\partial}{\partial r} (r^2 \langle u'v' \rangle)$$

$$- \frac{\partial}{\partial z} \langle v'w' \rangle + f_\phi \quad . \qquad (5A-5)$$

Let the propelier be at $z = 0(+)$ and integrate (5A-5) as

$$2\pi\rho \int_0^z dz \int_0^\infty \gamma^2 \, d\gamma \; . \; . \; . \quad .$$

The results

$$2\pi\rho \int_0^\infty VW \, \gamma^2 \, d\gamma + 2\pi\rho \int_0^\infty \langle v'w' \rangle \, \gamma^2 \, d\gamma$$

$$= 2\pi\rho \int_0^\infty \gamma^2 \, d\gamma \int_0^- dz \, f_\phi = \text{torque of propeller} \quad .$$

Now, in the far wake, $W = W_o$ and $\langle v'w' \rangle$ is a second order small quantity. Also, the torque is

$$\tau = \frac{\eta_p P}{\omega_p} \quad , \qquad \text{(5A-6)}$$

where P is the power delivered to the propeller, η_p is the propeller efficiency (nominally, in the 0.6 - 0.8 range) and ω_p is the angular velocity of the propeller.

Thus, in the far wake we have

$$2\pi\rho W_o \int_0^\infty V\gamma \, {}^2 a\gamma = \tau \quad , \qquad \text{(5A-7)}$$

a rather bvious relation, since

$$2\pi\rho \int_0^\infty (\gamma V)\, \gamma\, d\gamma = \text{angular momentum/unit length}$$

and τ is the rate of generation of angular momentum in the wake. The swirl in the wake is then constrained by the power delivered to the propeller.

To describe momentum conservation, we re-write (5A-2) as

$$\frac{\partial}{\partial z}(W^2) + \frac{1}{\gamma}\frac{\partial}{\partial \gamma}(\gamma UW) + \frac{1}{\rho}\frac{\partial \overline{P}}{\partial z} = -\frac{\partial}{\partial z}\langle w'^2\rangle - \frac{1}{\gamma}\frac{\partial}{\partial \gamma}(\gamma \langle u'w'\rangle) + f_z \quad . \tag{5A-8}$$

We now perform the integral

$$2\pi\rho \int_{z_o}^{z} dt \int_0^\infty \gamma\, d\gamma \ldots ,$$

where z_o is a point ahead of the body. This gives the relation

$$2\pi\rho \int_0^\infty (W^2 - W_o^2)\, \gamma\, d\gamma + 2\pi \int_0^\infty (\overline{P} - P_o)\gamma\, d\gamma$$

$$+ 2\pi \rho \int_0^{\infty} \langle w'^2 \rangle \gamma \, d\gamma$$

$$= 2\pi\rho \int f_z \, dz \, \gamma \, d\gamma = \text{total force acting on wake.}$$

Here P_o is the ambient pressure ahead of the body. We also have

$$2\pi\rho \int f_z \, dz \, \gamma \, d\gamma = F_T - \frac{1}{2} \rho \, C_D \, A_B \, W_o^2 \quad . \qquad (5A\text{-}9)$$

Here C_D is the drag coefficient of the body and A_B is its area $(= \pi \, (D/2)^2$, D = diameter). The thrust force of the propeller is written F_T here.

In the far wake we take $\overline{P} = P_o$, $W^2 - W_o^2 = 2W_o \, (W - W_o)$ and have

$$4\pi\rho \, W_o \int_0^{\infty} (W - W_o) \, \gamma \, d\gamma = F_T - \frac{1}{2} \rho \, C_D \, A_B \, W_o^2 \quad . \qquad (5A\text{-}10)$$

For a self-propelled submerged body the right-hand side of (5A-10) vanishes. For a towed body $F_T = 0$, while for a surface ship we expect $F_T > \frac{1}{2} \rho \, C_D \, A_B \, W_o^2$. The value of the right side of (5A-10) has a very important implication for the development and persistence of the wake.

A further integral constraint on the wake is given by Birkhoff and Zarantonello[10]:

$$2\pi W_o \int_o^\infty (W - W_o)\, r^3\, dr = \text{constant} \quad .$$

The evaluation of the turbulent energy

$$q = \frac{1}{2} \langle \underset{\sim}{v}'^2 \rangle \qquad (5A\text{-}11)$$

is described by [see Hinze, Eqs. (1-111)].

$$\left\{W \frac{\partial}{\partial z} q + U \frac{\partial}{\partial r} q\right\}$$

$$+ \left\{\langle w'^2 \rangle \frac{\partial W}{\partial z} + \langle u'^2 \rangle \frac{\partial U}{\partial r} + \langle v'^2 \rangle \frac{U}{r}\right.$$

$$\left. + \langle u'w' \rangle \left(\frac{\partial U}{\partial z} + \frac{\partial W}{\partial r}\right) + \langle u'v' \rangle\, r \frac{\partial}{\partial r} \left(\frac{V}{r}\right)\right\}$$

$$+ \left\{\frac{1}{r} \frac{\partial}{\partial r} \left[r \langle u' \left(\frac{1}{2} \underset{\sim}{v}'^2 + \frac{p'}{\rho}\right)\rangle\right] + \frac{\partial}{\partial z} \left[\langle w' \left(\frac{1}{2} \underset{\sim}{v}'^2 + \frac{p'}{\rho}\right)\rangle\right]\right.$$

$$= -\nu \left\langle \frac{\partial u'_i}{\partial x_1} \left(\frac{\partial u'_i}{\partial x_j} + \frac{\partial u'_j}{\partial x_1}\right)\right\rangle \equiv -\varepsilon \quad , \qquad (5A\text{-}12)$$

where we have used rectangular coordinates to express the turbulent dissipation rate ε .

The three bracketed terms on the right describe respectively, advection, production, and diffusion of turbulent energy.

The LP model[4] uses the simplest closure prescription. They write

$$\langle u'^2 \rangle = \langle v'^2 \rangle = \langle w'^2 \rangle \quad ,$$

$$\langle u'w' \rangle = - \nu_\tau \frac{\partial}{\partial \gamma} (W - W_o) \quad ,$$

$$\langle u'v' \rangle = - \nu_s \gamma \frac{\partial}{\partial \gamma} \left(\frac{V}{\gamma}\right) \quad ,$$

$$\langle w' \left(\frac{1}{2} v'^2 + \frac{p'}{\rho}\right) \rangle = - \nu_e \frac{3}{2} \frac{\partial}{\partial \gamma} \langle w'^2 \rangle$$

$$= \langle u' \left(\frac{1}{2} v'^2 + \frac{p'}{\rho}\right) \rangle \quad . \qquad \text{(5A-13)}$$

The three quantities ν_τ , ν_s, and ν_e were determined by a fit to observed data. Generally, the final fit seemed good.

A much more elaborate model is used by LTD[5],[6]. They write

$$\frac{\partial}{\partial x_k} \langle u_k' \, u_i' \, u_j' \rangle + \frac{\partial}{\partial x_j} \langle u_i' \, p' \rangle + \frac{\partial}{\partial x_i} \langle u_j' \, p' \rangle \qquad \text{(5A-14)}$$

$$= \nu_c \frac{\partial}{\partial x_k} \left(\sqrt{2q}\, \Lambda \frac{\partial}{\partial x_k} \langle u_i' u_j' \rangle \right) \quad .$$

[In FW[7] it is assumed that $\langle u_j' p' \rangle = 0$, but a more symmetric expression is used for the r[illegible]-hand side.]

$$2\nu \left\langle \frac{\partial u_i'}{\partial x_k} \frac{\partial u_j'}{\partial x_k} \right\rangle = \frac{2bq}{3\Lambda} \delta_{ij} + \frac{a\nu}{\Lambda^2} \langle u_i' u_j' \rangle \qquad (5A\text{-}15)$$

$$\left\langle \frac{p'}{\rho} \left(\frac{\partial u_i'}{\partial x_j} + \frac{\partial u_j'}{\partial x_i} \right) \right\rangle = - \frac{\sqrt{2q}}{\Lambda} \left(\langle u_i' u_j' \rangle - \frac{2}{3} q\, \delta_{ij} \right) \quad . \qquad (5A\text{-}16)$$

[FW[7] adds a term $C_1 q \left(\frac{\partial U_i}{\partial x_j} + \frac{\partial U_j}{\partial x_i} \right)$ to the right of (5A-16)].

The parameters are determined[6] from data on boundary layers and jets:

$$\begin{aligned} a &= 2.5 \ , \\ b &= \frac{1}{8} \ , \\ \nu_c &= 0.3 \ , \\ \Lambda &= 0.2\, \eta_{1/2} \ . \end{aligned} \qquad (5A\text{-}17)$$

LTD insert the relations (5A-14), (5A-15), and (5A-16) into the differential equations for $\langle u_i' u_j' \rangle$, which then provides a closed set of equations. LTD argue that it is consistent with the

data to set $C_1 = 0$ and that the more symmetric form of (5A-14) is unnecessarily complicated.

A significant simplification is introduced in FW[7]. It is assumed that deviations from isotropy are "small" and a set of coupled algebraic equations is obtained for the $\langle u_i' u_j' \rangle$.

The similarity in the results obtained from these three models suggests that conservation of momentum, angular momentum, and energy, coupled with a "reasonable" model for radial transport, determines the gross features of wake development.

REFERENCES FOR SECTION 5.0

1. Chevray, R., "The turbulent wake of a body of revolution," J. of Basic Engin., 90, 925 (1968).

2. Naudascher, E., "Flow in the wake of self-propelled bodies and related sources of turbulence," J. Fluid Mech., 22, 625 (1965).

3. Gran, R. L., "An experiment on the wake of a slender propeller-driven body," TRW Report 200 86-6006-RU-00, (June, 1973).

4. Lin, J. T., and Y. H. Pao, "The turbulent wake of a propeller-driven slender body in a nonstratified fluid," Flow Research Report No. 14, (Feb., 1974).

5. Lewellen, W. S., M. Teske, and C. Donaldson, "Application of turbulence model equations to axisymmetric wakes," AIAA Jour., 12, 620 (1974).

6. Lewellen, W. S., "Use of invariant modeling' Handbook of Turbulence, Vol I;" W. Frost and T. Moulder, Eds., Plenum Publ. Co., (1977).

7. Rottman, J. W., L. Y. Oey, J.C.S. Meng, and J. R. Grant, "A computational model for turbulent wake flows in a stratified fluid, Part I: Fundamental formulation," Science Applications Report 200-79-986-LJ, (Aug., 1980).

8. Grant, J. R., G. E. Innis, and W. Y. Shaw, "A computational model for turbulent wake flows in a stratified fluid, Part II: Numerical simulation of wake behind towed and self-propelled axisymmetric bodies," Science Applications Report 200-80-483-LJ, (Aug., 1981).

9. Hinze, J. O., "Turbulence," McGraw-Hill, Inc., (1975).

10. Birkhoff, G., and E. H. Zarantonello, "Jets, Wakes, and Cavities," Academic Press, New York, (1957).

11. Innis, G. E., to be published as an SAI report.

6.0 A FUTURE EXPERIMENT

After three years of theoretical effort without firm conclusions, it is time for an experimental effort.

1. The first step was a JSS 83 experiment.[1] We photographed a number of ship wakes off Southern California from the SIO aircraft, at elevations between 500 and 1500 feet. The principal result is that different ships have different wakes. Sometimes the $\pm$ 19.5° cusp stands out very clearly; it may be the outer edge of a broad Kelvin pattern, or simply two narrow cusp bands without much wave structure.[2] At times the $\pm$ 19.5° cusp was not visible, and the interior wake was. The turbulent wake can be single or double (depending on the number of propellers?), and can be visible as a slick (calm) region in a rough ambient sea, or as a roughened band in a calm background. Winds clearly make a difference.

Sun glitter can be used to advantage by photographing the wake at the edge of the glitter, where a slight favorable slope

---

[1] R. Davis, pilot; F. Zachariasen, navigator; W. Munk, photographer.

[2] This could be because the cusp attenuates downstream as $x^{-1/3}$ compared to $x^{-1/2}$ for the interior wake.

enhancement from the Kelvin waves can produce an enormous increase in specular return. In this way we could see many wave lengths of short divergent waves at very long distances behind the vessel.

2. We participated as observers in a joint U.S.-Canadian experiment led by Blyth Hughes of the Canadian Defense Establishment on Vancouver Island. The wake produced by the NOSC Vessel QUAPAW was measured by equipment forward of the bow of the ENDEAVOUR during wake crossings. The key device, designed by Hughes, is an upward-looking beam from a submerged laser mounted on the bow of the ENDEAVOUR. The beam is deflected by the tilted surface facets, and the deflection is recorded in two dimensions against time. The illuminated spot is a few mm, and the response time is a few ms, so that wavelengths down to a cm can be measured. Open sea measurements using Hughes' tilt device were published some years ago. The slope statistics so obtained were in very good accord with slope statistics derived from sun glitter.

A very crude ship-board analysis* indicates an amplitude pattern roughly consistent with thin ship theory for a traveling

*This was summarized in a letter of 5 August 1983, from Munk to Zachariasen, Dashen, and Davis.

source. However, the transverse slope $\partial\zeta/\partial y$ fails to grow with decreasing y, in contrast to the theoretical expectation $\partial\zeta/\partial y \sim y^{-1/2}$; in fact, significant slopes occur only just inside the 19.5° cusp.

It was also learned that the wake slopes were swamped by ambient slopes in the presence of even light winds. For future experiments we shall need to suppress the larger contribution to slopes from the ambient waves that are shorter than the ship wake waves.

3. It is now fairly clear that the interior (to the $\pm$ 19.5° cusps) behavior of transverse slopes is sensitive to the type of vessel, including hull shape and configuration of screws. We suspect that the narrow V's seen on the SAR images were associated with particular vessels that produce high interior transverse slopes. Our first recommendation is to perform wake calculations for various ships and to select some that seem suitable from the foregoing considerations. It would probably be advantageous if some suitable Naval vessels could be identified.

4. With regard to a future experiment, we propose

(a) To make simultaneous coordinated measurements of a Kelvin wake

(i) with a SEASAT-like SAR from a spacecraft.

(ii) optically from an aircraft.

(iii) with a Hughes device from a vessel (suitably low-passed).

It might be worthwhile to include coordinated photography from the spacecraft; it might also be possible to fly a second SAR on the aircraft.

(b) To cover a variety of parameters:

(i) Ship speed and direction.

(ii) At least two types of vessels, which produce significant interior transverse slopes.

(iii) Wind speed and direction (relative to vessel).

(iv) SAR viewing angles of 15°, 20°, 25°, with the vessel (centered on SEASAT's 20°).

(c) The experiments should be closely tied with numerical simulation.

It ought to be possible in such an experiment to identify the V signature on SAR images with other observables. Once this has been done, the theoretical effort can be focused and will no doubt produce early affirmative results.

5. An opportunity for such an experiment exists in connection with the proposed shuttle flight in August 1984.* The very purpose of the experiment is to gain an understanding of radar imagery of land and sea (including wind waves, internal waves, . . .), so that a study of Kelvin waves should be a natural part of the experiment (they are not included as of now).

There would be a total of about 10 passes over a given spot; this is a serious limitation. The desirability of placing the ship wake at the edge of sun glitter will call for careful orbit planning. Because of the possibility that shuttle flights are postponed or canceled, it is proposed that the experiment be planned to provide critical information even without the spacecraft.

We recommend two dedicated wake-making ships, operating as close as possible without wake interference. They should be on a

---

*The SIR-B Plan. JPL 82-78, December 1982.

straight course for at least half an hour prior to satellite passage. A third vessel is required for wake crossings. Aircraft glitter (and SAR) measurements and surface tilt measurements should be made not only during satellite passage but at other times as well.

Here is a possible expedition profile:

Satellite viewing angle	Two ships' speed	Cover relative to satellite	Wind speed
20°	fast	parallel	low
20°	slow	parallel	low
20°	fast	parallel	high
20°	slow	parallel	high
20°	fast	perpendicular	low
20°	fast	perpendicular	high
15°	fast	parallel	low
25°	fast	parallel	low

This just about exhausts the satellite measurement program. But many other configurations should be tested by aircraft and surface measurements.

We recommend a site near Maui, to provide a high probability of clear sky, and a variety of sites with (normally) different wind speeds.

There is some urgency if this program is to be carried out one year from now. A responsible group needs to be identified. One possibility is APL Johns Hopkins, who have experience in this field.

DISTRIBUTION LIST

Dr. Marv Atkins
Deputy Director, Science & Tech.
Defense Nuclear Agency
Washington, D.C. 20305

National Security Agency
Attn RS: Dr. N. Addison Ball
Ft. George G. Meade, MD 20755

Dr. Charles Buffalano
DARPA
Deputy Director for Research
1400 Wilson Boulevard
Arlington, VA 22209

Dr. Kenneth A. Case
The Rockefeller University
New York, NY 10021

Dr. Robert Cooper [2]
Director, DARPA
1400 Wilson Boulevard
Arlington, VA 22209

Dr. Roger F. Dashen
Institute for Advanced Study
Princeton, NJ 08540

Defense Technical Information [2]
Center
Cameron Station
Alexandria, VA 22314

The Honorable Richard DeLauer
Under Secretary of Defense (R&E)
Office of the Secretary of
Defense
The Pentagon, Room 3E1006
Washington, D.C. 20301

Director [2]
National Security Agency
Fort Meade, MD 20755
ATTN: Mr. Richard Foss, A05

CAPT Craig E. Dorman
Department of the Navy, OP-095T
The Pentagon, Room 5D576
Washington, D.C. 20350

CDR Timothy Dugan
NFOIO Detachment, Suitland
4301 Suitland Road
Washington, D.C. 20390

Dr. Larry Gershwin
NIO for Strategic Programs
P.O. Box 1925
Washington, D.C. 20505

Dr. S. William Gouse, W300
Vice President and General
Manager
The MITRE Corporation
1820 Dolley Madison Blvd.
McLean, VA 22102

Dr. Edward Harper
SSBN, Security Director
OP-021T
The Pentagon, Room 4D534
Washington, D.C. 20350

Mr. R. Evan Hineman
Deputy Director for Science
& Technology
P.O. Box 1925
Washington, D.C 20505

Mr. Ben Hunter [2]
1917 Westmoreland Street
McLean, VA 22101

The MITRE Corporation [25]
1820 Dolley Madison Blvd.
McLean, VA 22102
ATTN: JASON Library, W002

Mr. Jack Kalish
Deputy Program Manager
The Pentagon
Washington, D.C. 20301

Dr. Sherman Karp [3]
DARPA/STO
1400 Wilson Boulevard
Arlington, VA 22209

Mr. John F. Kaufmann
Dep. Dir. for Program Analysis
Office of Energy Research, ER-31
Room F326
U.S. Department of Energy
Washington, D.C. 20545

Dr. George A. Keyworth
Director
Office of Science & Tech. Policy
Old Executive Office Building
17th & Pennsylvania, N.W.
Washington, D.C. 20500

MAJ GEN Donald L. Lamberson
Assistant Deputy Chief of Staff
(RD&A) HQ USAF/RD
Washington, D.C. 20330

Dr. Donald M. LeVine, W385 [3]
The MITRE Corporation
1820 Dolley Madison Blvd.
McLean, VA 22102

Mr. V. Larry Lynn
Deputy Director, DARPA
1400 Wilson Boulevard
Arlington, VA 22209

Mr. John McMahon
Dep. Dir. Cen. Intelligence
P.O. Box 1925
Washington, D.C. 20505

Director
National Security Agency
Fort Meade, MD 20755
ATTN: William Mehuron, DDR

Dr. Marvin Moss
Technical Director
Office of Naval Research
800 N. Quincy Street
Arlington, VA 22217

Dr. Walter H. Munk
9530 La Jolla Shores Drive
La Jolla, CA 92037

Dr. Julian Nall [2]
P.O. Box 1925
Washington, D.C. 20505

Director
National Security Agency
Fort Meade, MD 20755
ATTN: Mr. Edward P. Neuburg
DDR-FANX 3

Prof. William A. Nierenberg
Scripps Institution of
Oceanography
University of California, S.D.
La Jolla, CA 92093

Mr. C. Wayne Peale
Office of Research and
Development
P.O. Box 1925
Washington, DC 20505

The MITRE Corporation
Records Resources
Mail Stop W971
McLean, VA 22102

Mr. Alan J. Roberts
Vice President & General Manager
Washington C^{3}I Operations
The MITRE Corporation
1820 Dolley Madison Boulevard
McLean, VA 22102

Los Alamos Scientific Laboratory
ATTN: C. Paul Robinson
P.O. Box 1000
Los Alamos, NM 87545

Mr. Richard Ross [2]
P.O. Box 1925
Washington, D.C. 20505

Dr. Phil Selwyn
Technical Director
Office of Naval Technology
800 N. Quincy Street
Arlington, VA 22217

Dr. Eugene Sevin [2]
Defense Nuclear Agency
Washington, D.C. 20305

Mr. Robert Shuckman
P.O. Box 8618
Ann Arbor, MI 48107

Dr. Joel A. Snow [2]
Senior Technical Advisor
Office of Energy Research
U.S. DOE, M.S. E084
Washington, D.C. 20585

COMD William O. Studeman
Director, Long Range Planning Group
Office of C&O (OP-09X)
Navy Department
Washington, DC 20350

Mr. Alexander J. Tachmindji
Senior Vice President & General Manager
The MITRE Corporation
P.C. Box 208
Bedford, MA 01730

Dr. Vigdor Teplitz
ACDA
320 21st Street, N.W.
Room 4484
Washington, D.C. 20451

Dr. Al Trivelpiece
Director, Office of Energy Research, U.S. DOE
M.S. 6E084
Washington, D.C. 20585

Dr. John F. Vesecky
Center for Radar Astronomy
233 Durand Building
Stanford University
Stanford, CA 94305

Mr. James P. Wade, Jr.
Prin. Dep. Under Secretary of Defense for R&E
The Pentagon, Room 3E1014
Washington, D.C. 20301

Dr. Kenneth M. Watson
2191 Caminito Circulo Norte
La Jolla, CA 92037

Mr. Leo Young
OUSDRE (R&AT)
The Pentagon, Room 3D1067
Washington, D.C. 20301

Dr. Fredrik Zachariasen
California Institute of Technology
1201 East California Street
Pasadena, CA 91125